Design of a Novel X-Section Architecture for FX-Correlator in large Interferometers

A THESIS PRESENTED IN PARTIAL FULFILMENT

OF THE REQUIREMENT FOR THE DEGREE

OF

DOCTOR OF PHILOSOPHY

IN

ENGINEERING

AT

MASSEY UNIVERSITY

AUCKLAND

NEW ZEALAND

BY

VIGNESH RAJA BALU

2020

ABSTRACT

Design of a Novel X-Section Architecture for FX-Correlator in large Interferometers

Vignesh Raja Balu

Doctor of Philosophy in Engineering -School of Engineering and Technology

Massey University, Auckland, New Zealand

In large radio-interferometers it is considerably challenging to perform signal correlations at input data-rates of over 11 Tbps, which involves vast amount of storage, memory bandwidth and computational hardware. The primary objective of this research work is to focus on reducing the memory-access and design complexity in matrix architectural Big Data processing of the complex X-section of an FX-correlator employed in large array radio-telescopes.

This thesis presents a dedicated correlator-system-multiplier-and -accumulator (CoSMAC) cell architecture based on the real input samples from antenna arrays which produces two 16-bit complex multiplications in the same clock cycle. The novel correlator cell optimization is achieved by utilizing the flipped mirror relationship between Discrete Fourier transform (DFT) samples owing to the symmetry and periodicity of the DFT coefficient vectors. The proposed CoSMAC structure is extended to build a new processing element (PE) which calculates both cross- correlation visibilities and auto-correlation functions simultaneously. Further, a novel mathematical model and a hardware design is derived to calculate two visibilities per baseline for the Quadrature signals (IQ sampled signals, where I is In-phase signal and Q is the 90 degrees phase shifted signal) named as Processing Element for IQ sampled signals (PE_IQ). These three proposed dedicated correlator cells minimise the number of visibility calculations in a baseline.

The design methodology also targets the optimisation of the multiplier size in order to reduce the power and area further in the CoSMAC, PE and PE_IQ. Various fast and efficient multiplier algorithms are compared and combined to

achieve a novel multiplier named Modified-Booth-Wallace-Multiplier and implemented in the CoSMAC and PE cells. The dedicated multiplier is designed to mostly target the area and power optimisations without degrading the performance.

The conventional complex-multiplier-and-accumulators (CMACs) employed to perform the complex multiplications are replaced with these dedicated ASIC correlator cells along with the optimized multipliers to reduce the overall power and area requirements in a matrix correlator architecture. The proposed architecture lowers the number of ASIC processor cells required to calculate the overall baselines in an interferometer by eliminating the redundant cells. Hence the new matrix architectural minimization is very effective in reducing the hardware complexity by nearly 50% without affecting the overall speed and performance of very large interferometers like the Square Kilometre Array (SKA).

ACKNOWLEDGEMENT

First and foremost, I would like to express my sincere gratitude to my supervisor **Associate Professor Rezaul Hasan** for his continuous encouragement and valuable guidance throughout this research project. I also acknowledge the financial support I received as Junior Research Officer for my supervisor's MBIE funded Square Kilometre Array **(SKA)** project.

I greatly appreciate the support of my co-supervisor **Dr. Khalid Arif** for his thoughtful comments and recommendations on this dissertation.

I am also thankful to the **School of Engineering** and all its member staff for all the help and support rendered throughout the course of this research.

I extend my gratefulness to **CSIRO**, **JPL** and **NRC** for the collaborative support and resources provided to me, which facilitated to enhance my technical expertise.

My deep and sincere gratitude to my beloved **parents** for their continuous and unparalleled love, help and support. I am forever indebted to my parents for giving me the opportunities and experiences that have made me who I am.

Nevertheless, I also would like to thank my father-in-law **Mr. Djegadissane** for his diligent proof reading of this thesis.

I am grateful to my wife **Mrs. Jayaselvi Djegadissane** for her continued and unfailing love, consistent support and encouragement which has been invaluable throughout this study.

Finally, I owe a special thanks to my daughter **Miss Jayanethra** for being patient and understanding during this study and greatly value her unconditional love and support.

Dedicated to my parents
(Mr. Balu.M & Mrs. Shanmuga Vadivu S.P.)

DECLARATION

The author hereby declares that this is his own work except where due acknowledgement has been given. It is being submitted for the PhD in Engineering to Massey University, New Zealand.

This thesis describes the research carried out by the author at the School of Engineering, Massey University, New Zealand from January 2016 to March 2020, supervised by Associate Professor Rezaul Hasan.

TABLE OF CONTENTS

LIST OF FIGURES

LIST OF TABLES

DEFINITIONS AND ABBREVIATIONS

ADC	Analog to Digital Convertors
ADSP	Astronomical Digital Signal Processing
ALMA	Atacama Large Millimetre/submillimetre Array
ASIC	Application Specific Integrated Circuits
BEOL	Back-end-of-line
CMAC	Complex Multiplier and Accumulator
CMOS	Complementary Metal–Oxide–Semiconductor
CoSMAC	Correlator system Multiplier and Accumulator
CSP	Central Signal Processing
DFT	Discrete Fourier transform
FFT	Fast Fourier Transform
FPGA	Field Programable Gate Array
GMRT	Giant Metre wave Radio Telescope
GPU	Graphics Processing Unit
HDL	Hardware Description Language
HPP	High Performance Process
IQ	In-Phase and Quadrature Signal
JPL	Jet Propulsion Laboratory
JVLA	Jansky Very Large Array
LEDA	Large-Aperture Experiment to Detect Dark Ages
LFAA	Low-Frequency Aperture Array Structures
LSB	Least Significant Bit
MERLIN	multielement radio-linked interferometer
MSB	Most Significant Bit

MWA	Murchison Widefield Array
NRAO	National Radio Astronomy Observatory
PE	Processing Element
PE_IQ	Processing element for IQ sampled signals
PVT	process-voltage-temperature
RAM	Random Acces Memory
RTL	Register Transfer Level
SDP	Science Data Processing
SKA	Square Kilometer Array
SNR	Signal to Noise Ratio
VHF	Very High Frequency
VLA	Very Large Array
VLBI	Very Long Baseline Interferometer
VLSI	Very Large-Scale Integrated Circuits

CHAPTER 1: INTRODUCTION

Radio interferometers are array of telescopes, which monitor the cosmic and astrophysical changes that happen in space. Many on-going and future interferometer projects like Square Kilometre Array (SKA) have very high data rate in terms of Tb/s, which create a problem of “BIG DATA” handling for the astronomers and design engineers. These tera bits of data per second will immensely increase the complexity in signal processing electronics for storage, processing and transmitting in an efficient manner. There is thus an enormous necessity for providing faster and cheaper miniaturized low power electronics to overcome this Big-data challenge in astronomical digital signal processing (ADSP).

Beamforming, Correlation, Pulsar search and Imaging are the important operations performed in interferometers, in which the correlator plays a major role in image formation in ADSP architectures of all interferometer types. The correlation is a simple process but in interferometers it’s been complicated because of very high data flow. In interferometers, the correlator performs cross-correlation among signal pairs and auto-correlation of each signal with itself to form cross products and auto-correlation functions respectively. There are two types of correlators, Lag or XF correlator and FX correlator. Unlike the lag correlator, the FX correlator, converts each time domain signal to frequency domain in F-section using FFT followed by the X-section, which performs the multiplication and accumulation over each frequency sample for all the signals and directly measures the cross-power spectrum. The correlator size increases with the rate of the square of the number of antennas in the interferometer multiplied with their total band width and hence justifies the fact that the correlator is the most power consuming unit for very large array telescope structures.

The correlator in existing telescopes like Karl G. Jansky Very Large Array (JVLA) with 32 antennas and Atacama Large Millimetre/submillimetre Array (ALMA) with 64 antennas consume 70kW and 65kW power respectively. Both these have the same bandwidth of 8000 MHz and the correlator design of JVLA uses 130nm ASIC technology whereas ALMA correlator uses 250nm. The

correlator of the largest existing Large-Aperture Experiment to Detect Dark Ages (LEDA) telescope has 256 antennas, a total bandwidth of 57.55MHz and uses 28nm GPU technology which consumes 7.37kW of power. The correlator of an ongoing project SKA1-Low (512 antennas, 300Mhz bandwidth) and SKA1-Mid (197 antennas, 5000MHz bandwidth) are planned to be designed using the 16nm FPGA technologies and the power utilization has been calculated as 11.6kW and 40kW respectively.

This clearly shows that the power consumption is a major issue in implementing the correlation process for large antenna array structures. The state-of-art approach in this work targets the design of low power Array Processing Unit in X-section of FX correlator for performing correlation in large telescopes using 28 nm ASIC technology. This work mainly targets to achieve low power and area which is not based on the technology but totally based on the architectural design. The proposed design in this work can be implemented in any technology which will consume low power and occupy less area when compared to the existing method in the same technology. For this reason, the existing CMAC is designed with the same 28 nm technology and compared with the proposed architecture.

1.1 Research Challenges

In all type of interferometers, a Complex Multiplier and Accumulator (CMAC) is used to implement the correlation operation performed in the X-section. However, it consumes more power and area in interferometry correlator design using large number of antenna array structures. Even though the CMAC sharing is performed among different baseline calculations, it reduces only the area but not the power. The design of low power ASIC for calculating the Cross Correlation among the large array of antennas is still quite challenging. The main challenges for designing a correlator in interferometers are:

1) The very high data rate from these interferometer antennas leads to the problem of “Big DATA” handling.
2) Increase in the complexity of signal processing electronics to transmit these data in an efficient manner.

3) Requirement of memory to store the input and output will increase significantly.
4) The data processing needs a large number of temporary registers and hardware to process the data internally.
5) The correlator size increases in the rate of the square of the number of antennas in the interferometer multiplied with the total band width obtained.
6) The power consumption will rise tremendously if the antenna size increases.

1.2 Research Objective

The main objective of this research work is to design an area and power optimised array processing architecture to perform the complex multiplication and accumulation in X-section of FX correlator used in the large interferometers like SKA-LOW. In this state-of-art, the design phase embraces the basic multiplier design followed by the design of a dedicated correlator multiplier architecture and a processing element and finally ends with the design of the Matrix array structure for the X-Section. All the relevant publications and documents are clearly reviewed to obtain a power efficient solution for designing this state-of-the-art.

1.3 Research contributions to Knowledge

The research work explained in this thesis will give an insight knowledge about the design of a correlator for large interferometers. The subsequent chapters contribute to have a better understanding on Interferometers, different types of correlators and detailed investigations on conventional architectures. A new modified multiplier architecture is proposed and used to design a power efficient dedicated correlator multiplier and accumulator. Different techniques have been combined to design the X-section of the FX correlator, thereby reducing the overall memory requirement, area and power dissipation for correlation of large interferometers.

1.4 Thesis organization

In this thesis, Chapter 2 outlines the history and basics of interferometers, big data challenges in large interferometers and an introduction to the ongoing interferometer project Square Kilometre Array (SKA). It also discusses on the useful Fourier transforms that are helpful in interferometer calculations and understanding of the process involved in it. The different correlator architectures and advantages of FX Architecture in designing a correlator for large array interferometers and Low power Architecture for SKA are discussed in Chapter 3. It also analyses all the conventional multiplier and correlator designs for better understanding to design an efficient architecture. In Chapter 4, a mathematical model for a dedicated correlator multiplier and accumulator is derived and the hardware is designed. A processing element which calculates both auto and cross-correlation using the dedicated correlator multiplier is designed and explained. Furthermore, a power and area efficient multiplier is designed and implemented in both the dedicated correlator multiplier and accumulator and the processing element and the results are discussed. In Chapter 5, the final X-section design algorithm of the FX correlator is based on the multiplier, dedicated correlator multiplier and accumulator, and the processing element implemented in chapter 4. Chapter 6 summarizes the research outcomes of the design and deliberates the scope of future work.

CHAPTER 2: LITERATURE REVIEW

Astronomy is the study of celestial objects and phenomena of space and about their physical and chemical properties. In ancient times, before the invention of tools like telescopes, the astronomy was based on the observations and estimations of visible objects like the sun, moon and stars through naked eye. In later civilisations, specifically in Egypt, China, India, Greece and Central America, the astronomical observatories were created and the positions of planets, stars and their natural satellites were mapped. The evolution of astronomy flourished ubiquitously in the middle age. The work done by Kepler [1] was the first system which explains clearly about the motion of planets revolving around the sun. Celestial Mechanics, Gravitational law and reflecting telescope [2] were invented by Sir Isaac Newton which finally enlightens the planets' motion with evidence.

The reflecting telescope overcame the disadvantages of refracting telescopes then and in the later years, various enhancements were made to improve the quality and size of it. The introduction of Spectroscope and Astrophotography made significant improvements in astronomy which helped to prove the existence of various galaxies including the earth's galaxy milky way, black holes and neutron stars [3]. In the 20th century, the advancement in Physical Cosmology stepped up Astronomy to the next level. The Big Bang theory [4] formulated in early 1900s' explained about the expansion of universe from very high temperature state and density [5]. This model was profoundly confirmed by the electromagnetic radiation and by the cosmological abundance of elements. The information about the universe obtained by visible light are mostly by the electromagnetic radiation. The observational astronomy record data according to the specific range of frequencies, wavelength and photon energy. Some spectrum ranges can be observed from the earth's surface or in some high altitudes but some need to be observed from space (outside the earth's atmosphere). Based on the observation wavelength of electromagnetic spectrum, the observation astronomy can be classified into Radio astronomy, Infrared astronomy, Optical astronomy, Ultraviolet astronomy, X-ray astronomy and Gamma-ray astronomy.

2.1 Radio Astronomy

The study of radio waves invading from space is termed as Radio Astronomy [6]. The radiation from Milky Way was the first radio wave from a space object discovered in the year 1932 by Karl Jansky in Bell Telephone Laboratories. He also made a sequence of observations on different radio emissions and identified various stars, quasars, radio galaxies, masers and pulsars. The invention of cosmic microwave background radiation through radio astronomy proves the Big Bang Theory with strong evidences. A single or multiple-linked radio telescopes also called radio antennas are used to receive the radio waves from the space using the Radio Interferometry and aperture synthesis techniques [6]. The interferometer power is based on the distance between the antennas it has and not based on the size of it. Thus, the interferometry helps to achieve high angular resolution in radio astronomy [7].

$$Frequency = \frac{Speed\ of\ light}{Wavelength} \tag{2-1}$$

where, speed of light = 299792.5 km/s.

The Frequency range of the radio waves ranges from 20 kHz to about 600 GHz frequencies and the corresponding wavelength ranges from several kilometres to 500 microns. The relation between the Frequency and wavelength of any wave can be calculated using the equation (2-1).

2.1.1 History of Radio Astronomy

Before the discovery of radio waves from Milky Way by Jansky, many researches were speculated to observe the radio waves emitted from the astronomical objects. A Physicist James Clerk Maxwell formulated the relation of electromagnetic radiation with electricity and magnetism, and proved that it could exist at any wavelength in 1860's. From 1896 to 1900, several experiments were made to detect the radio emissions from the Sun by Johannes Wilsing and centimetre wave radiation by Oliver Lodge. The technical limitations of the instruments used in their experiments ended with failure on detecting emissions.

Later, they found that, the astronomical radio transmission signals bounce back into the space from the layer which makes it to be undetectable [8].

Figure 2-1: Grote Reber's 9m diameter Parabolic antenna remains in National Radio Astronomy Observatory (NRAO) as a historical monument [9]. First Radio telescope used for astronomical research.

In 1901, Guglielmo Marconi improved the design of radio transmitter and receiver and successfully transmitted and received the radio waves over the ocean. Then in early 1931, Karl Jansky explored the radio static and discovered the radio waves from Milky Way. The work was further carried out by Grote Reber in 1937, who constructed a 9.5-m diameter parabolic radio telescope in his backyard and conducted the first sky survey with radio frequencies. He first designed the 3300 MHz receiver to detect the space signals, failing which, he designed the 900 MHz receiver and finally succeeded in receiving the radio emission of Milky Way with 160 MHz receiver and conformed the Jansky Invention. Between 1938 and 1943, he conducted surveys on radio waves from space and published the results. He published the first radio frequency sky map in the year of 1944. The Figure 2-1 shows that the Grote Reber's Parabolic antenna remains in National Radio Astronomy Observatory (NRAO) as a historical monument. After the World War II, many countries involved in radio astronomical research and began constructing larger antennas and bigger receivers based on Grote Reber Inventions [9].

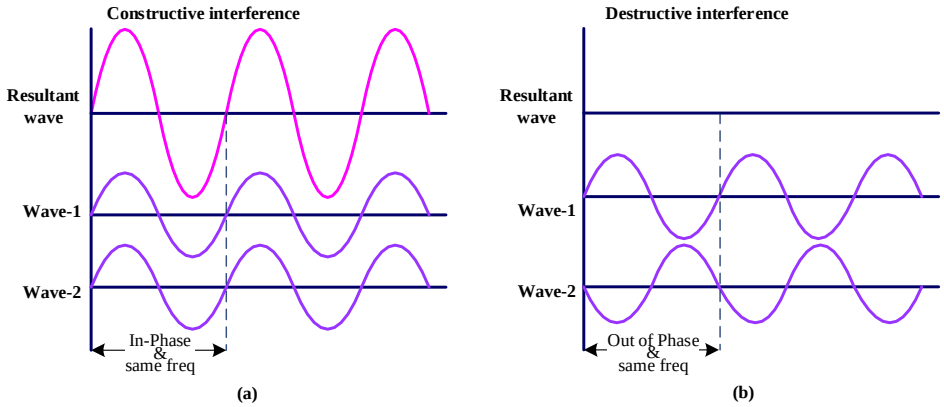

Figure 2-2: (a) two waves with same frequency and in-phase result in Constructive interference (b) two waves with same frequency and out-of-phase (antiphase) result in Destructive interference[10].

In 1942, J.S.Hey first observed the radiation from the sun and he concluded that the sun emits strong radiation. During World War II, J.A Ratcliffe and other members of Telecommunication Research Establishment in Cambridge University had a wartime research on radars, and they found the radio wave emissions from the sun. Later, they did observations on other space objects and initiated the interferometry techniques to differentiate the angular source of detected radio waves. The Earth's rotation aperture synthesis technique was developed by the Cavendish Astronomers Martin Ryle and Antony Hewish. In 1950's, the Astronomical department of Cambridge University constructed the Mullard Radio Astronomy Observatory near Cambridge. The optical telescope cannot identify most of the gases, neutral atoms and fast-moving electrons in galaxies, but these are detected by the radio telescopes because they emit in the range of radio wavelength. H.I.Ewen and E.M.Purcell discovered the neutral Hydrogens spectral line emission in the year 1951 which helped the astronomers to determine the shape of our own galaxy.

After 1960's, the evolution of computers made it possible to handle the computationally intensive Fourier transform inversions. The aperture synthesis was first used to create 'One-Mile' aperture and later used One-mile and Ryle telescopes to create five Km aperture arrays [11]. In 1967, a young graduate student Jocelyn Bell-Burnell and Anthony Hewish observed that a radio pulse occurred 30

times a second in a regular interval from the radio telescope. The flashes of radio emission from the natural phenomenon found was named as Pulsers, the leftover after the explosion of Supernova. Pulsers are also known as spinning Neutron stars which are strongly magnetized. The important discovery of cosmic background radiation by Wilson and Penzias got a Nobel prize in 1978 which is the strongest proof of Big Bang Theory.

2.1.2 Interferometry basics and its importance on Radio Astronomy

Interferometry is an exploration technique which mostly uses light or electromagnetic waves. These waves are superimposed to produce the required information [10]. The main application of this interferometry is in many fields like optometry, astronomy, oceanography, bio-molecular interactions, spectrometry, etc.

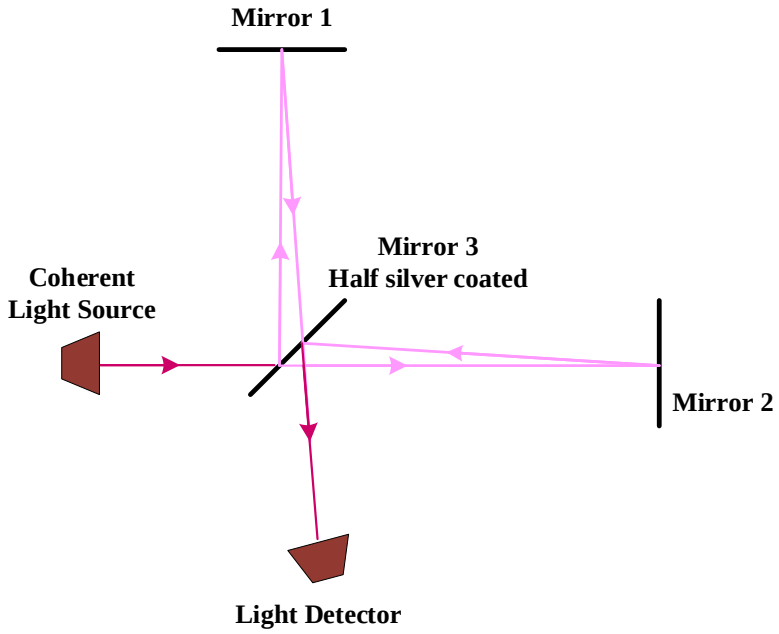

Figure 2-3: The incoming light beam is split into two and again recombined before detector using a half-silvered mirror. Either constructive interference or destructive interference may happen depending on the phase difference between the two beams [12].

The interferometry combines the waves to analyse their actual state by utilising the property of superposition. The superpose of two waves with the same frequency give the phase difference between them. When two waves are in-phase,

it results in constructive interface and when in out-of-phase, it results in destructive interface as shown in Figure 2-2. For other conditions where the signals are not in-phase and out-of-phase, the result will be an intermediate intensity pattern from which the relative phase difference can be determined [13].

In interferometry, the incoming light beam is divided into two beams with a partly reflecting mirror. The two beams obtained after beam splitting are identical in nature. These two beams travel in different paths and are then recombined before reaching the detector. This provides the path difference among the two beams and from which the phase difference can be obtained [13]. This is clearly described in the Figure 2-3. Based on different measures, the interferometry techniques are categorized as homodyne and heterodyne detection, double path and common path, wave splitting and amplitude splitting.

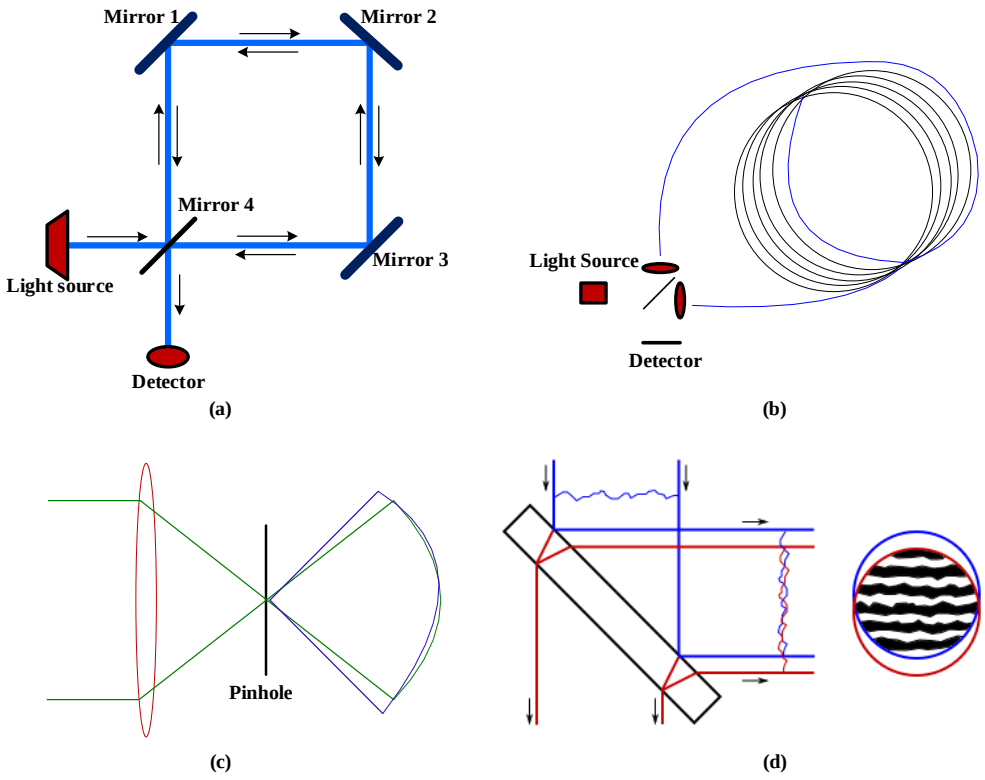

Figure 2-4: Interferometers using common path technique. (a) Sagnac interferometer (b) Fibre-optic Gyroscope (c)Lateral Shearing (d) Point Diffraction [12]

In the double path method, the reference and the input beams travel laterally in different paths. The best example of double path method interferometry is Michelson interferometer as shown in Figure 2-3. In the Common path method, the reference and the input signals travel in the same path. Sagnac, Fiber-optic Gyroscope, point diffraction and lateral shearing interferometers shown in Figure 2-4 are good examples for this common path method.

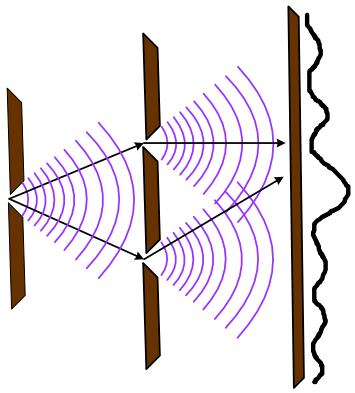

Figure 2-5: The source light wavefront is divided into two wavefronts in Young's interference experiment [12]

Wavefront splitting is a method in which the light wavefront emerging from a source is divided into two wavefronts, passes in different paths and later are recombined near the detector. Figure 2-5 illustrates this operation which is called as Young's interference experiment. In Amplitude splitting type, it splits the amplitude of the given input from the source into separate beams and later they are recombined. Fizeau interferometer shown in Figure 2-6 is the best example for amplitude splitting interferometers.

Interferometry plays a major role in the radio astronomy to read the astronomical objects in the form of radio frequencies. In radio astronomy, large radio antennas or radio telescopes are employed independently or in an array structure to observe radiation coming from the space using interferometry and aperture synthesis techniques. The single radio telescopes are not good enough in resolution which lay the path for the radio interferometry. The interferometry technique improves the angular resolution because the interferometers work based on the distance between the antennas but not on the size.

Combining two or more number of antennas focusing on the same source exactly at the same time are called Interferometers. The signals from all the antennas in an interferometer are combined to get a useful information and this signal is equal to the signal obtained from a single antenna having the diameter of spacing between the interferometer antennas. To obtain a very high-resolution image, different separations have been introduced between the antennas and this separation between any pair of antennas is termed as baseline [14-16].

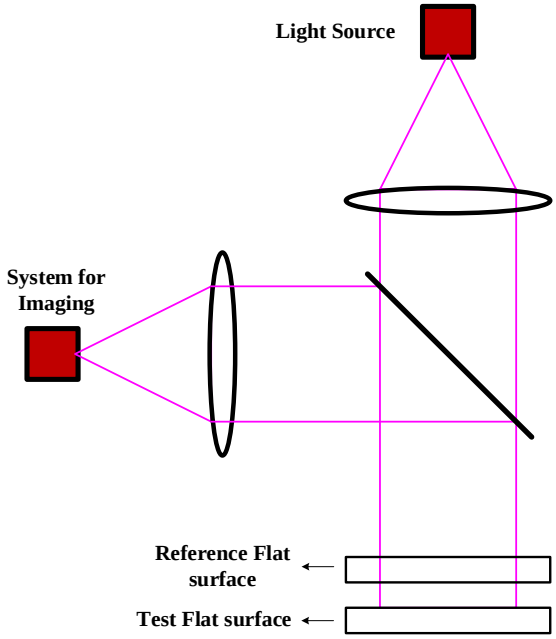

Figure 2-6: Fizeau interferometer (Amplitude-splitting interferometer type [12])

In the earlier stages, the data collected from the antennas were first stored in magnetic tapes or hard disks and then later correlated with all the antenna pairs to form baselines. But at present, the technological advancements made it possible to perform the same operation in real time [14].

2.1.3 Evolution of Radio Interferometers

The First interferometry technique was introduced by Michelson Stellar by using two optical receiving apertures to determine the angular width of stars like Arcturus and Betelgeuse [17, 18]. The Figure 2-7(a) shows the Michelson-Pease stellar interferometer in which the mirrors guide the incoming rays to the telescope aperture. The star width is comparable with the spacing among the maxima's and

the points across the star are superpositioned to form an image. The fringes maxima minima from various points are individual, and the amplitude of the fringe is attenuated as shown in Figure 2-7(b). Michelson measured the relative amplitude fringes and defined the fringe visibility, as

$$Fringe\ Visibility = \frac{Maxima\ Intensity - Minima\ Intensity}{Maxima\ Intensity + Minima\ Intensity} \quad (2\text{-}2)$$

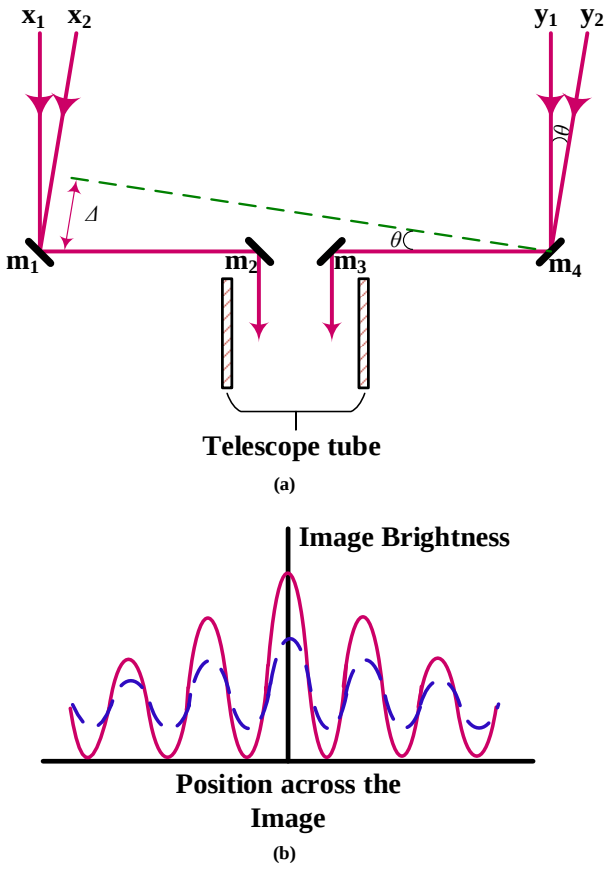

Figure 2-7: Michelson-Pease stellar interferometer (a) Schematic diagram showing how the two mirrors m1 and m2 guide the incoming rays into the telescope aperture. (b) Intensity of the image. The broken line is the fringe profiles of partially identified star and the solid line shows fringe profiles for the unresolved star.

The Ryle and Vonberg used dipole antenna arrays to construct a radio interferometer which investigates the cosmic radio emission in 1946, shown in Figure 2-8. This simple interferometer added the signal received from the dipole antenna arrays and fed to the receiver to find the power [19]. This is the first astronomical Radio Interferometer developed to observe the space with two antennas. Then during the World War II, a different type of interferometer called

the Sea or Lloyd mirror interferometer [20] was installed, which had number of horizontal pointing antennas in several coastal areas near Sydney in Australia for radar communication. Bolton and Stanley used this interferometer to observe the Cygnus A and proved the presence of a discrete non-solar radio sources [21]. This interferometer was not further improved because of the difficulties like the long atmospheric paths, variation in the physical length of the baseline based on the cliff height, and the sea surface irregularity.

The Dipole antenna [19] and Sea radio interferometer [20] had other noises such as thermal noise on the sidelobes of the antenna, background galactic radiation and the amplifier noise in the receiver. Ryle introduced a phase switching technique as shown in Figure 2-9 which filtered the unwanted components of the receiver output other than the fringe oscillations. This phase switching interferometer is the first interferometer to use the voltage multiplying of correlator to combine the signals from two different antennas. Now a days with the technological advancements, the phase switching for voltage multiplying action is not used but still helps to remove different instrumental imperfections.

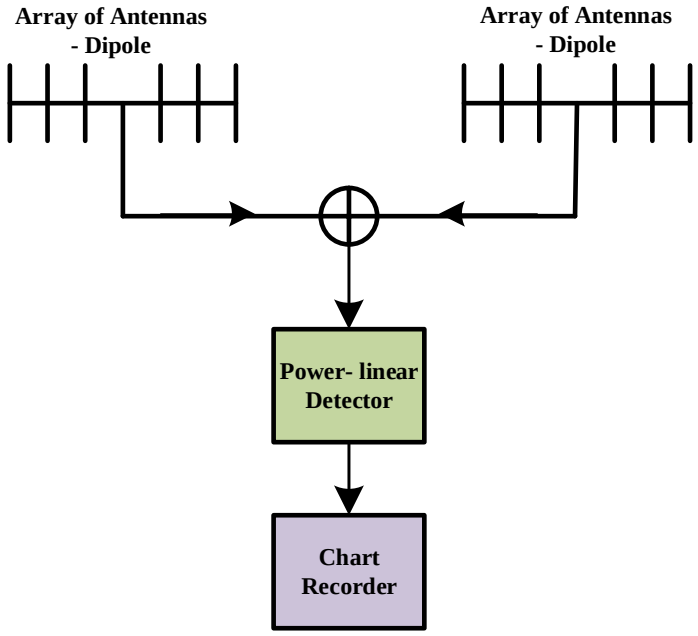

Figure 2-8: Adding Interferometer. The signals are combined additively, and the receiver is sensitive to a narrow band frequency.

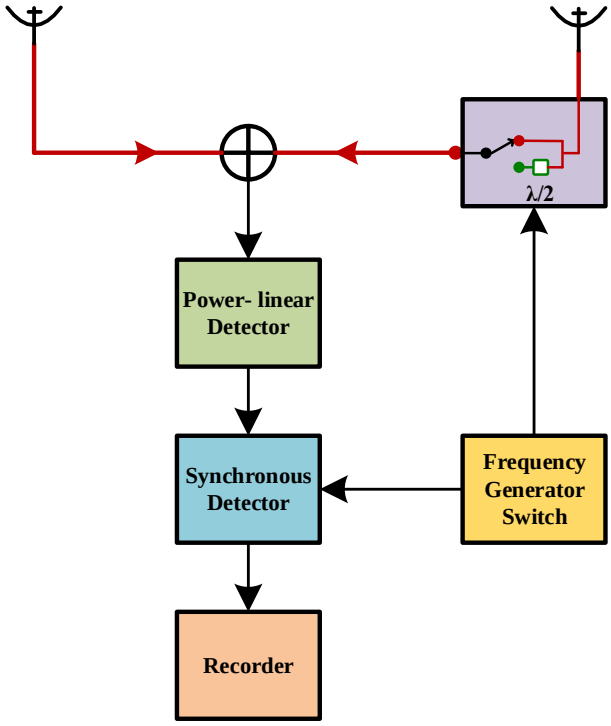

Figure 2-9: Phase Switching Interferometer. Among two antenna signals, one is periodically phase reversed, and switching extra half wavelength into the transmission line.

Various astronomical calibrations were made to accurately position the small diameter radio sources during 1950s and 1960s. Hanbury Brown and Twiss experimented and publicized that if the two spaced antennas received signals were sent through the square-law detectors, the intensity fluctuations in the received field strength were correlated [22]. The signals were combined before detection in the conventional interferometer in which the correlation degree changes in proportion based on the visibility. In intensity interferometer it's not required to preserve the signals' radio frequency phase while transmitting to the combining location. For correlation in remote location, VHF radio links were used to transport the signal from the antennas. Jennison and Latham used three antennas and recorded three set of fringes simultaneously [23]. At Jodrell Bank Experimental station, Hanbury Brown constructed an interferometer with high angular resolution and sensitivity [24]. The equipment was updated up to 130 km baselines to obtain one inch less resolution and higher sensitivity in 1960s [25] and then was developed into multielement radio-linked interferometer called MERLIN array.

Many research works were conducted, and various instruments were made to image the Sun. As the radio source is very strong from the sun, it does not require very large apertures. A grating array technique was implemented to perform the solar observation. Eight equally spaced linear array of antennas were connected to a branching network with equal electrical path length from the receiver and in order to enhance the angular resolution, it is combined with the two-gating array structures as shown in Figure 2-10. Christiansen and Warburton used 32 east-to-west and 16 north-to-south uniformly spaced parabolic antennas in grating technique and imaged the quiet sun in 2-D form at 21-cm wavelength [26]. It was also possible to reduce the grating responses on the sky by combining one grating array antennas into a single larger antenna [27]. Later the received antenna signals were converted to Intermediate Frequency (IF) and separate voltage multiplying correlators were used for every spacing which relaxed the arrangement of antennas to maximize the number of different antennas spacings.

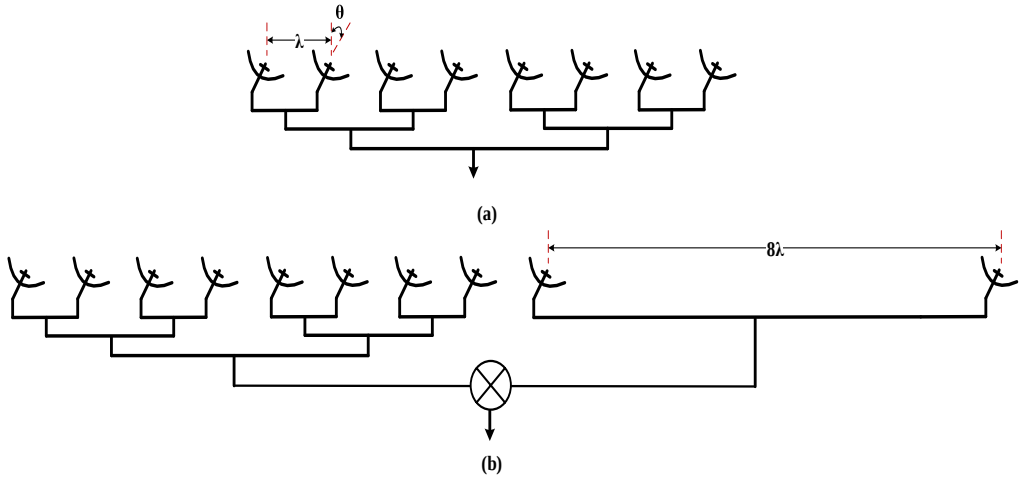

Figure 2-10: Gating Array Interferometer. (a) Eight equally spaced linear array of antennas were connected to a branching network with equal electrical path length from the receiver. (b) Two element array structure combined with eight gating arrays to improve the angular resolution.

It was later found that the measured intensity profiles were not symmetrical in nature, meaning that the fringe pattern phase and the amplitude varied based on the antenna spacing. In 1970's the availability of computers to process and record data, perfection in electronic phase stability, improvement on calibration of fringes, advancement in antennas and receivers made possible to perform measurements on

wavelengths in the range of centimetres(~1GHz). The earliest interferometer in Owens Valley Radio Observatory which was widely used for shaping the radio structure delivers a good example [28] on detecting 960 MHz to few GHz. Using Nancay Observatory in France, Lequeux observed nearly 40 extragalactic sources in the range of 1400 MHz with baselines upto 1.46 km East-to-west and 380 m north-to-south [29]. In 1960s, the interferometers were upgraded with the spectral line receiving system in which each receiver passband was subdivided into multiple channels using filter bank in IF stages. The signal from the different antennas were correlated in separate correlators. An interferometer in Canada was built specifically to observe neutral hydrogen in the range of 21-cm wavelength [30].

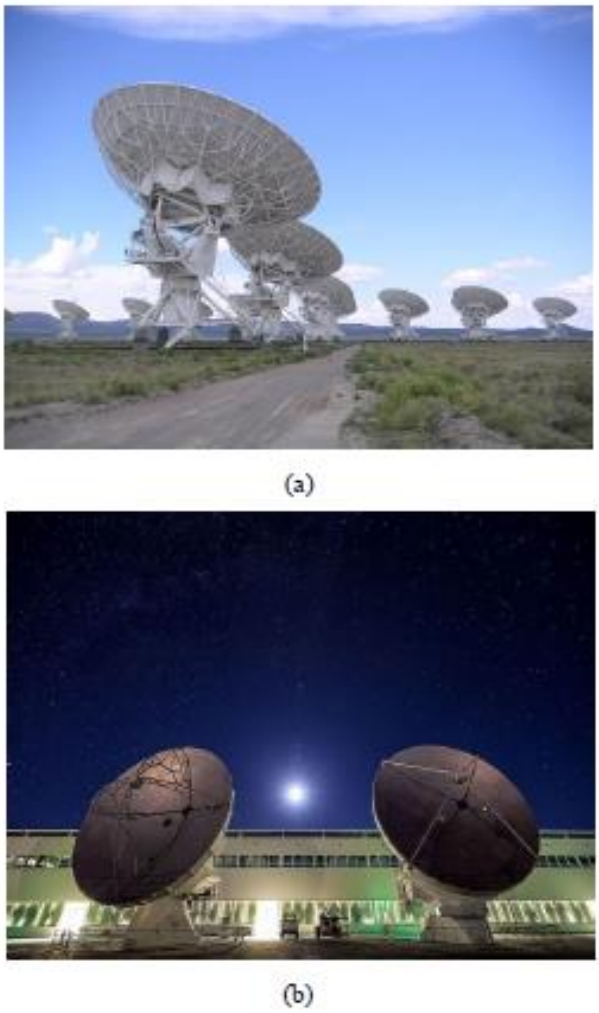

Figure 2-11: Radio interferometers: (a) Very Long Baseline Interferometer (VLBI) radio telescopes collecting astronomical data (b) Atacama large Millimetre Array (ALMA) radio telescopes used to read sub millimetre and millimetre wavelengths [14]

The next advancement in synthesis imaging was utilising the variation obtained by earth's rotation in the antenna baseline [31]. The One-Mile Radio Telescope of Cambridge was the first interferometer which utilised the Earth's-rotation technique to various radio sources. After this achievement by One-Mile telescope, the synthesis imaging became popular and was adopted by other interferometers. The Netherland's Westerbork Synthesis Radio Telescope [32], England's Five-Kilometre Radio Telescope [33] and New Mexico's Very Large Array (VLA) [34] used centimetre wavelength with less than 1-inch resolution to image the radio sources. Very Long Baseline Interferometer (VLBI) shown in Figure 2-11 (a) was the first interferometer which achieved the resolution of central sources [35]. The Giant Metrewave Radio Telescope (GMRT) was constructed in India with huge collecting area and operated in the range of 38 to 1420 MHz frequency [36]. The technological advancement in Very Large-Scale Integrated circuits (VLSI) and broadband antenna technology added a great performance increase in Interferometers. Later, with these new technological improvements, VLA interferometer was upgraded and now it's called as Karl G. Jansky Very Large Array (JVLA) [37].

In 1990s, short millimetre wavelengths of frequency range of 100 GHz and more, were established in the synthesis arrays. Unlike centimetre wavelengths, millimetre wave lengths needed some more considerations due to shorter wavelength, which led to worse effect on the signal phase if any irregularities were present in the atmospheric path length. To overcome this effect and to obtain the required sensitivity in millimetre wavelength, a greater number of antennas were required in the arrays than the centimetre wavelength. The Nobeyama Millimetre Array in Japan [38], Hat Creek, California [38]; Atacama, Chile; and Mauna Kea, Hawaii [39] are the best examples of Millimetre array. The Atacama Large Millimetre/submillimetre Array (ALMA) [40] in Atacama Desert of Chile, shown in Figure 2-11 (b) was the biggest among these and started its function in 2013. It has two arrays in which one has twelve 7m-diameter antennas and the other has fifty 12m-diameter antennas and the overall operating frequency range is from 31GHz to 950 GHz. The antennas are spaced in the range of 14 km and the field of view is about 8 inches at 345 GHz with the primary array.

The ongoing interferometer project Square Kilometre Array (SKA) will be the world's largest telescope after its construction. It was conceived in the year 1991 and a group of international working team was formed in 1993. The total area of construction is expected to be approximately one square kilometre that is equal to 11,000,000 sq. ft [41]. This interferometer is planned to operate in a wide range of frequencies and the sensitivity is expected to be 50 times more than the other radio interferometers. The SKA has two arrays called SKA-Low (Low frequency range) and SKA-Mid (mid frequency range). The construction targets to start in mid 2020s with the SKA-Low consisting of 512 antenna stations and a total bandwidth of 300MHz, and SKA-Mid with 197 antenna stations and 5000 MHz bandwidth [42].

2.2 Useful Fourier transforms in Interferometry

The Fourier transform is a means to break a waveform or function and represents it in an alternate way as the sum of sinusoidal function. The Fourier transform theory explained here is more focused towards the radio interferometry [43] and for more complete explanations refer to [44-46]. Let's consider a function $f(l)$, after applying Fourier transform to this function it can be written as,

$$F(Z) = \int_{-\infty}^{\infty} f(l) e^{-j2\pi Zl} dl \tag{2-3}$$

The inverse Fourier transform helps to obtain the original function $f(l)$ from the Fourier transformed function $F(Z)$ as shown below,

$$f(l) = \int_{-\infty}^{\infty} F(Z) e^{j2\pi Zl} dZ \tag{2-4}$$

So, the transform pair can be written as $f(l) \leftrightarrow F(Z)$. In function $f(l)$, if the unit of l is in time, then in the transfer function, the unit of Z will be in frequency (Hz or cycles/second). The transform pair can also be written in time – frequency domain as,

$$F(\omega) = \int_{-\infty}^{\infty} f(t)e^{-j\omega t}dt \tag{2-5}$$

$$f(t) = \frac{1}{2\pi}\int_{-\infty}^{\infty} F(\omega)e^{j\omega t}d\omega \tag{2-6}$$

The Fourier transform has many interesting properties which are very useful in interferometry. The Linearity property of Fourier transform in equation (2-7) represents that the visibility function is the sum of all the components visibility function present in an image.

$$f(l) + g(l) \leftrightarrow F(Z) + G(Z) \tag{2-7}$$

$$f(al) = \frac{1}{|a|}F(Z)\left(\frac{Z}{a}\right) \tag{2-8}$$

According to the Similarity property as shown in equation (2-8), when the function $f(l)$ narrows, then its transfer function $F(Z)$ widens equivalently and the same happens vice versa. This makes the product of function width Δl in l domain and ΔZ in Z domain to satisfy the relation,

$$\Delta l \Delta Z \sim 1 \tag{2-9}$$

This equation (2-9) is called as the product of time-bandwidth function in radar astronomy signal-processing [47]. All functions can be divided into odd and even components as shown in equation (2-10 & 2-11). The symmetric property of Fourier transform says that if the function $f(l)$ is even and real, then the transfer function $F(Z)$ is also the same, and if $f(l)$ is real and odd, then the transfer function $F(Z)$ is imaginary and odd.

$$f_{even}(l) = \tfrac{1}{2}[f(l) + f(-l)] \tag{2-10}$$

$$f_{odd}(l) = \tfrac{1}{2}[f(l) - f(-l)] \tag{2-11}$$

The two most important properties of Fourier transform in radio interferometry is the convolution and correlation properties. Correlation is the measurement of the similarity between two signals and convolution is the measurement of effect of one signal on the other signal. The convolution theorem states that the multiplication of two transfer functions is similar to the convolution of two functions, i.e. in terms of time domain and frequency domain, we can say that the multiplication of two frequency domain signals is always equal to the convolution of two-time domain signals as shown below,

$$f(t) * g(t) \leftrightarrow F(\omega)G(\omega) \tag{2-12}$$

The correlation or cross correlation of two functions is helpful to measure the similarity between each other, which is the most important process in radio interferometry image formation. The equation (2-13) shows the property of correlation.

$$f(t) \star g(t) \leftrightarrow F(\omega)G^*(\omega) \tag{2-13}$$

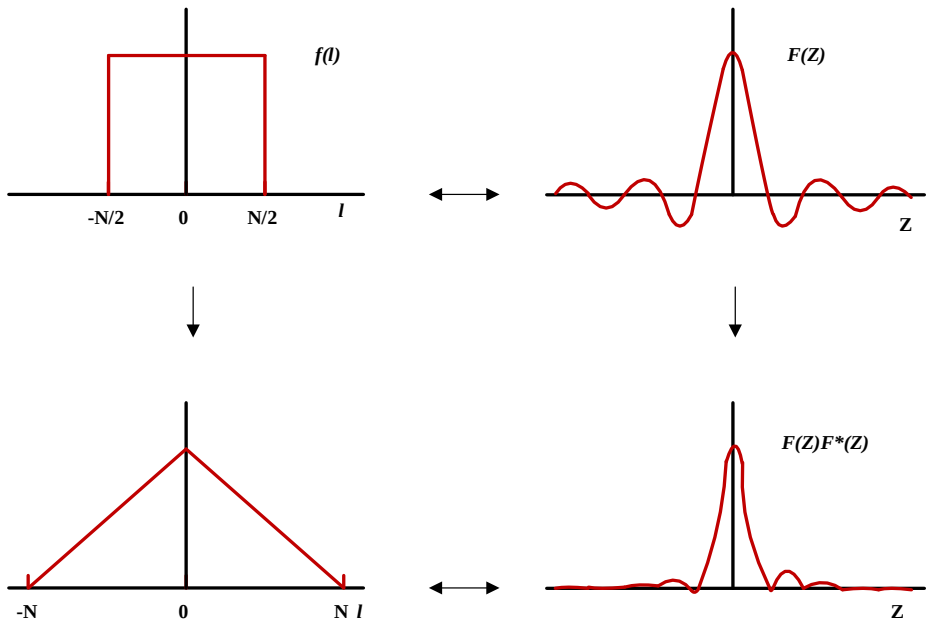

Figure 2-12: The function $f(l)$ is an even function. The convolution $f * f$ and the correlation $f \star f$ are indicated by the left vertical arrow. The convolution $F(Z)F(Z)$ and correlation $F(Z)F^*(Z)$ are indicated by the right vertical arrow [47].

The example shown in Figure 2-12 shows the relation between convolution and correlation, for the even function $f(l)$. This depicts that both convolution and correlation are identical and produce an even function when F(Z) is real and even.

Apart from these properties, there are five other Fourier transform pairs which are more useful in radio interferometry. The first Fourier transform pair is the unit rectangular function or boxcar function which is represented as $\prod(l)$,

$$f(l) = 1 \; for \; |l| \leq \frac{l_0}{2}$$
$$f(l) = 0 \; for \; other \; conditions \tag{2-14}$$

$$F(Z) = l_0 \frac{sin\pi Z l_0}{\pi Z l_0} = l_0 sinc(Z l_0). \tag{2-15}$$

The second one is a Gaussian function whose transfer function $F(Z)$ is calculated using "completing the square" procedure [47],

$$f(l) = e^{-\frac{l^2}{2a^2}} \leftrightarrow F(Z) = \sqrt{2\pi} a e^{-2\pi^2 a^2 Z^2} \; . \tag{2-16}$$

In the third Fourier transform pair, the transfer function $F(Z)$ is estimated by using the limiting process and considering the function $f(l)$ in exponentials [47],

$$f(l) = cos2\pi z_0 l \leftrightarrow F(Z) = \frac{1}{2}[\delta(Z - z_0) + \delta(Z + z_0)] \; . \tag{2-17}$$

The infinite train delta function pair is the fourth useful Fourier transform pair. Starting with a finite series of impulses and by using the shift property of Fourier transform, the relation can be proved [47],

$$\sum_{n=-\infty}^{\infty} \delta(l - n l_0) \leftrightarrow \sum_{m=-\infty}^{\infty} \delta\left(Z - \frac{m}{l_0}\right) \tag{2-18}$$

The Fifth one is the Heaviside step function,

$$f(l) = 1 \quad for \quad l \geq 0$$
$$f(l) = 0 \quad for \quad l < 0 \tag{2-19}$$

$$F(Z) = \frac{1}{2}\delta(Z) + \frac{1}{j2\pi Z} \tag{2-20}$$

Here, the transfer function is calculated by dividing the $f(l)$ function into odd and even components, applying the Fourier transform separately and finally combining them together.

If the function $f(l)$ has the periodicity property over the time interval - $\frac{l_0}{2}\ to \frac{l_0}{2}$, it can be represented by a special case of Fourier transform called Fourier series as given below,

$$f(l) = \sum_{n=-\infty}^{\infty} \propto_n e^{\frac{j2\pi nl}{l_0}} \tag{2-21}$$

where

$$\propto_n = \int_{\frac{-l_0}{2}}^{\frac{l_0}{2}} f(l)\, e^{\frac{-j2\pi nl}{l_0}} dl \tag{2-22}$$

This is applicable only for the functions which are random processes, for, the ergodic random process functions extending to infinity have some difficulties and can be overcome by selecting the truncated version of the function, $f_T(l)$.

$$f_T(l) = f(l) \prod \left(\frac{l}{l_0}\right) \tag{2-23}$$

where, $\prod(\frac{l}{l_0})$ is the unit rectangular function. According to the convolution property, the transfer function of the truncated version is,

$$F_T(Z) = F(Z) * l_0 sinc(Z l_0). \quad (2\text{-}24)$$

The truncation version power spectrum is not based on T and has the units of power and is defined by the equation (2-25), for detailed derivation please refer the reference [6].

$$P_T(Z) = \frac{1}{T} F(Z) F^*(Z). \quad (2\text{-}25)$$

The Fourier transform of random process autocorrelation function and its power spectrum is also called as Wiener-Khinchin relation[48, 49].

2.3 Cross-Correlation and Wiener-Khinchin theory

The Wiener-Khinchin relation helps to analyse the cross correlation between two different signals. The correlator response of a radio interferometer is given by the following equation (2-26),

$$C(\tau) = \lim_{T\to\infty} \frac{1}{2T} \int_{-T}^{T} f_1(t) f_2^*(t-\tau) dt \quad (2\text{-}26)$$

In equation (2-26), the symbol * represents that the complex conjugate is applied to the second signal. In practice, the correlation is measured for a finite time period 2T, which is usually a few seconds or minutes but is long when compared to both the period and the reciprocal bandwidth of the waveforms. The factor 1/2T is sometimes omitted, but for the waveforms considered here, it is required to obtain convergence. The $C(\tau)$ is the cross-correlation function between $f_1(t)$ and $f_2(t)$ and can be represented as

$$C(\tau) = f_1(t) \star f_2(t) \quad (2\text{-}27)$$

Substituting equation (2-27) in equation (2-26) results in,

$$f_1(t) \star f_2(t) = \lim_{T\to\infty} \frac{1}{2T} \int_{-T}^{T} f_1(t) f_2^*(t-\tau) dt \qquad (2\text{-}28)$$

The integral part can be represented as convolution as shown below,

$$f_1(t) \star f_2(t) = \lim_{T\to\infty} \frac{1}{2T} \int_{-T}^{T} f_1(t) f_{2-}^*(t-\tau) dt = f_1(t) * f_{2-}(t) \qquad (2\text{-}29)$$

In the above equation, $f_{2-}(t) = f_2(-t)$. The Fourier transform pairs for the two signals are represented as $f_1(t) \leftrightarrow F_1(\omega)$, $f_2(t) \leftrightarrow F_2(\omega)$, and $f_{2-}^*(t) \leftrightarrow F_2^*(\omega)$ and based on the convolution theorem, the equation (2-29) can be written as,

$$f_1(t) \star f_2(t) \leftrightarrow F_1(\omega) F_2^*(\omega) \qquad (2\text{-}30)$$

The equation (2-30) is the important relation for cross correlation spectrometry, in which the R.H.S value is the cross-power spectrum of the two signals ($f_1(t)$ and $f_2(t)$). The cross-power spectrum is always the cross- correlation Fourier transform and a function of frequency. If the two signals $f_1(t)$ and $f_2(t)$ are equal, then the transfer function of it is an autocorrelation and the equation (2-30) relates the Wiener-Khinchin function.

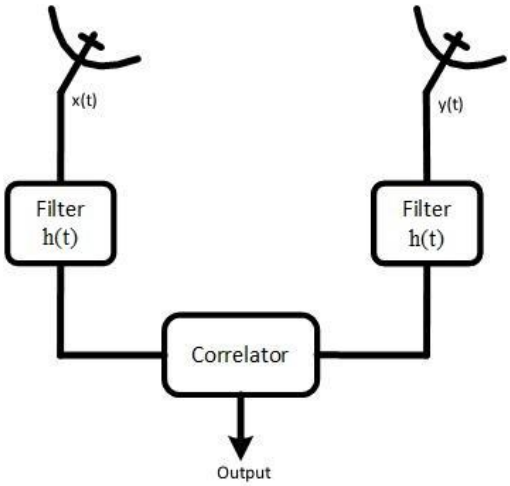

Figure 2-13: Basic interferometer receiving system.

2.4 Interferometer Receiving System Response

The antennas are the main components of the receiving section in interferometers which convert the incident signals to voltage levels. These outputs from the antennas are filtered to obtain the required frequency band and finally correlated as shown in Figure 2-13. In this analysis, the receiving signal strength and the antenna frequency response are constant over the passband filtering. The correlator response is always based on the signal voltage product and hence the antenna response is expressed in terms of voltage reception pattern [50], given by the equation (2-31). In this equation (2-31) the $A_v(l,m)$ is the antenna voltage reception pattern which is the transfer function of distribution field $\bar{\varepsilon}(X,Y)$ aperture where the coordinates X and Y determine the position, and λ represents the wave length.

$$A_v(l,m) \propto \iint_{-\infty}^{\infty} \bar{\varepsilon}(X,Y) e^{j2\pi\left[\frac{X}{\lambda}l+\frac{Y}{\lambda}m\right]} dXdY \tag{2-31}$$

The receiving area of antenna is a real number, and it's quite common to represent the response of an antenna in terms of $A(l,m)$. The $A_v(l,m)$ is replaced with its modulus proportional value $\sqrt{A(l,m)}$ [50]. The total interferometer response is regulated based on witnessing the uncertain source with its recognized flux density and location. The antenna output voltage based on the incident field $E(l,m)$ is given as

$$V = \iint_{-\infty}^{\infty} E(l,m)\sqrt{A(l,m)}dldm \tag{2-32}$$

The received input signal is passed to the filter. The frequency response of the filter $H(\omega)$ is the function of bandpass limit it has, which finalises the receiving channel response. The filter output $V_o(\omega)$ is the product of the filter response $H(\omega)$ and the input $V_i(v)$.

$$V_o(\omega) = H(\omega)\, V_i(\omega) \tag{2-33}$$

The impulse response $h(t)$ of the filter is the inverse Fourier transform of the frequency response $H(\omega)$. So, in time domain it can be represented in convolution as,

$$v_o(t) = \int_{-\infty}^{\infty} h(t) v_i(t - t_0) = h(t) * v_i(t) \tag{2-34}$$

Preferably, the frequency response is used, which is more related to deal in frequency domain calculations. In correlator, the voltage levels obtained from two filters are cross-correlated and the output is,

$$C_o(\tau) = \lim_{T \to \infty} \frac{1}{2T} \int_{-T}^{T} V_1(t) V_2^*(t - \tau) dt \tag{2-35}$$

In the above equation, the τ represents the delay of the second signal from first signal. In continuous operation, the delay τ is zero or some small value. The input signal for the correlator is mostly complex and hence the output is a complex visibility which has both the amplitude and phase value [50].

2.5 Overview of SKA

Square Kilometre Array [51] is a multi-radio telescope project built to answer several questions in fundamental physics and astrophysics [52, 53] and aimed to study the space with a total collecting area of approximately one square kilometre, featuring high sensitivity and angular resolution with a large field of view. SKA comprises of sub-arrays of different antenna types that make up the SKA1-low and SKA1-mid types with frequencies ranging from 50 MHz to 14 GHz. The SKA1-low observatories are built in Australia, the SKA1-mid observatory has been built in South Africa and the total control and global headquarters is established in U.K as illustrated in Figure 2-14. The SKA1-low system baseline design [54] initially

was targeted to have the frequency ranging from 50 MHz to 350 MHz with an overall bandwidth of 300 MHz.

The design also included 250,000 maximum number of channels with a channel resolution of 1 kHz. Similarly, the baseline design for SKA1-Mid included three bands of frequencies ranging from 350 MHz to 3050 MHz. The maximum available bandwidth for the three bands was allocated as 700 MHz, 808 MHz and 1403 MHz respectively. The SKA1-Mid design was based on SKA dishes only [54, 55] with each dish having a sensitivity at 6.9m2/Km.

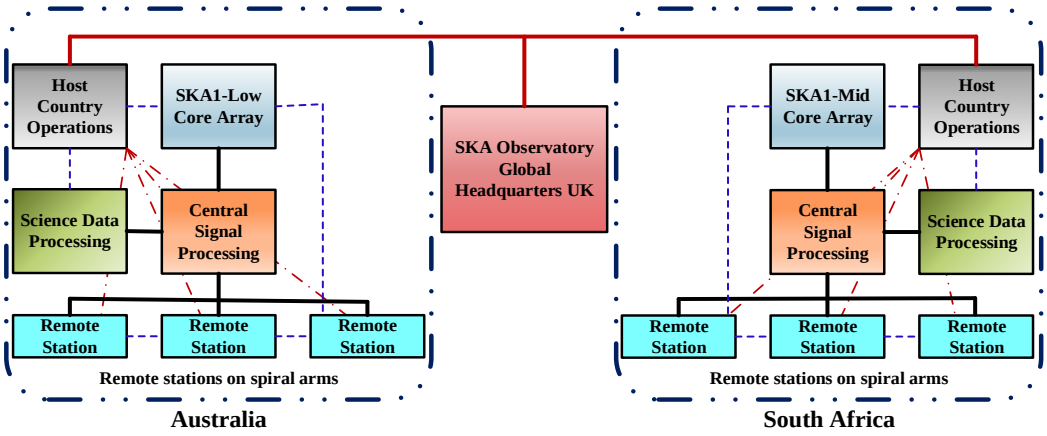

Figure 2-14 Block diagram illustrating the Geographical location of SKA1 observatory and its operational overview [54].

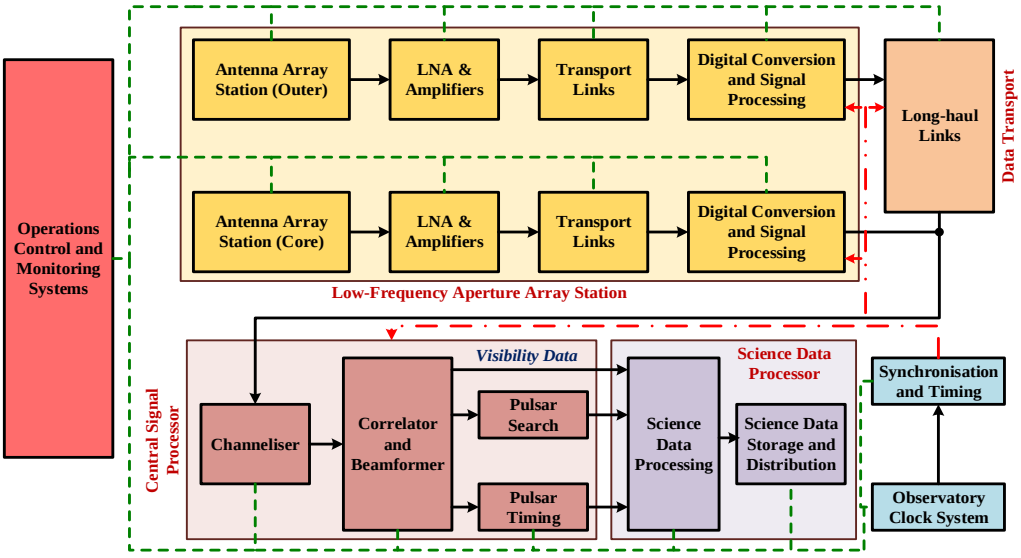

Figure 2-15: Functional block diagram of SKA1-Low [54].

2.5.1 SKA1 – Low

The SKA1-Low project is based in Australia where more than hundred thousand (100,000) antennas have been erected in phase1 [56, 57] to cover all the low frequency radio waves from 50 MHz to 350 MHz using 512 dual polarised antenna stations and may be expanded in the next phase [58] (phase 2) to millions of antennas. The SKA1-Low is an aperture array configuration similar to LOFAR in Netherlands [59-62] and was initially proposed to operate in the frequency range of 50-350 MHz [63, 64]. Later, many performance analyses were conducted by having a dual band implementation of antennas and also by increasing the operational frequency range of the SKA1-Low antennas which augmented the fact of increase in the performance of the SKA1-Low antennas [65]. This SKA1-Low antenna aperture array receives exa bytes of data per second and stores one peta byte of data per day [66].

The processing of signals in SKA1-Low is categorised in three stages [67]: signal processing in Low-Frequency Aperture Array Structures (LFAA) stations, Central Signal Processing (CSP) and Science Data Processing (SDP) as illustrated in the Figure 2-15.The signals from the antennas are digitized using the Analog to Digital Convertors (ADC) and fed to the filter banks for producing the frequency bands. These bands are fed as input to the beam former where the signals are delayed and added with other such bands from different antennas to form a beam. This beam forming technique is applicable for small frequency bandwidths only and hence, needs channelization [68] prior to it. The above two processes of digitization and beam forming occur in the first stage. In the central signal processing [66] as shown in Figure 2-16, the beams are again channelized and gain corrected to obtain finer frequency channels which are then correlated to improve the signal to noise ratio of the data [68, 69].

The correlation of the signals is integrated for some dump period based on the rotation of the Earth and the outputs are called as baselines [68, 70].These baselines are used to construct the sky images in the SDP. Initially, in SDP, the baselines are calibrated for direction dependent and direction independent effects and further given to the image pipeline to create a map which represents a complex

gain function of a beam [71]. The map is then scaled up [72], multiplied with the baseline and added to the Fourier grid happening in various time steps called as W-snapshots [73] and finally recombined to form a single grid. By using Fourier Transform and re-convolution algorithm [74, 75], the dirty image and bright sky sources are obtained respectively. The sky model is obtained from the sky sources and finally yields the sky image after several iterations.

2.5.2 SKA1 – Mid

The SKA1-Mid is planned in South Africa MeerKAT site [76] which has large dish-based array of nearly 200 dishes including 64 MeerKAT dishes with single-pixel feeds and covering a frequency ranging from 350 MHz to 14 GHz. On comparing SKA1-Mid with an existing JVLA telescope [77], it has four times better resolution and sensitivity, and the survey speed is 60 times faster than JVLA. The signals received from these dishes are divided into narrow band channels and the cross-power spectrum is calculated in the central signal processing unit. The dishes are placed in spiral arm structures extending from 2.5 km to 100km from the middle.

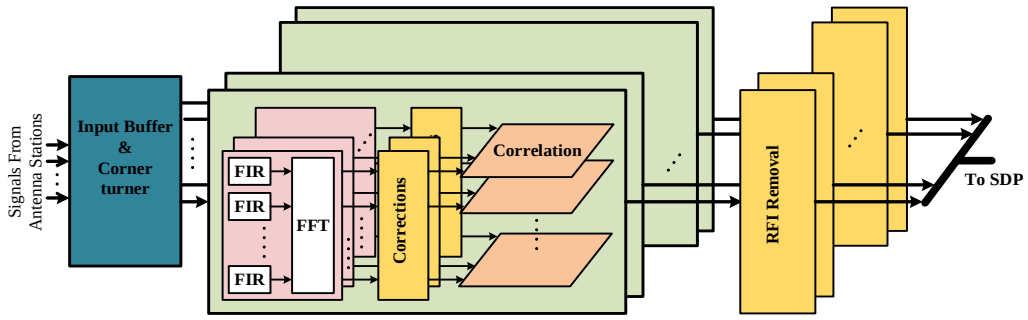

Figure 2-16: The detailed block diagram of central signal processing unit in SKA1-Low [66]

The Correlator architecture is same as that of the SKA1-Low, but the computing complexity on calculating cross correlation is reduced due to the smaller number of antennas in SKA1-Mid when compared to SKA1-Low.

2.6 Big Data challenges in large interferometers

The large astronomical radio interferometers like South Africa's KAT-7, Europe's LOFAR, EVLA in New Mexico, ALMA & LSST in Chile, and the ongoing projects like SKA planned in Australia and South Africa will produce very large volumes of data in the range of several terabytes per day to several hundred terabytes per second. This enormous amount of data is termed as big data based on its volume, velocity and the different forms it takes [78]. While handling this big data, the normal data management systems found this to be difficult on memory operations, processing speed of this data and the array of disparate data format collected. Specific design conditions must be thought of to handle this big data in terms of data processing, transport, storage and management aspects.

The Jet Propulsion Laboratory (JPL) addresses these big data issues emphasising on low power digital processing architectures, real time analysis of big data using adaptive algorithms and design of scalable data archive systems [79]. In due course, this big data also increases the area of hardware utilisation for the above-mentioned processes and hence increases the power consumption apparently. It has also been highlighted that the correlation process in the radio interferometer arrays consumes more power than the other sectors and an ASIC design of the correlator helps to minimise the power consumption in terms of data transfer and storage.

The need to address the big data challenges is hence evident and becomes more vital in the SKA project as the beam forming and correlation appear to be the major processing tasks in this telescope array, handling loads of data from the antennas. If the array consists of Na number of antennas, then Na (Na-1)/2 number of antenna pairs is seen and for each polarised input signal from one antenna, four correlations are performed per antenna pair. A survey carried out in [80] states that the SKA interferometers have three arrays: low, mid and survey with 1024, 254 and 96 dual polarised input signals with a maximum bandwidth of 0.3, 5 and 36x0.5 GHz respectively. Also, based on the bandwidth and the number of antennas and inputs, the data rate and loads have been estimated for the three telescopes of SKA as mentioned in Table 2-1.

	Input data rate (Tb/s)	Compute load Arithmetic (Pops/s)	Correlator dump size (Tb)	Correlator dump time (sec)	Output data rate (Tb/s)
LOW	11.8	5.0	32.7	0.6	57
MID	48.8	5.1	2.1	0.08	26
SURVEY	66.4	2.6	10.7	0.3	36

Table 2- 1: Input and Output data rates, dump size and dump time of correlators in SKA telescopes [80].

It is evident from the Table 2-1 that the input and output data rates depend on the number of antennas and the number of frequency channels and implies that big data handling and storage has a significant design factor in SKA telescopes, as the number of antennas and frequency channels are higher in order of magnitude here when compared to the current radio interferometers. The data rate of SKA radio interferometer is approximately estimated by the equation (2-36) [81] that is given below.

$$R \propto Na(Na-1).ns.\frac{B}{\Delta B}.\frac{1}{\Delta t}.s^{-1} \qquad (2\text{-}36)$$

Here Na is the array of antennas in the interferometer, ns is the polarization factor, B is the signal bandwidth, ΔB is the channel bandwidth and Δt is the sampling period. Thus, the data rate totally depends on the number of antennas, polarization factor and the bandwidth of the signal which proves that the data rate increases tremendously if there seems to be any increase in the above-mentioned factors. In VLA architecture, for 27 antennas with the polarization factor of 4, having a bandwidth of 1 MHz and a sampling period of 10, the data rate is approximately equal to 3x106/s and 20GB for an hour [81]. But, the Murchison Widefield Array (MWA) shown in Figure 2-17 is the first telescope for SKA and has 128 antennas with a polarization factor of 4 [81]. The bandwidth is 30 MHz with a sampling rate of 2 and produces a data rate of 100x106/s which is 30 times larger than that of the VLA architecture discussed above.

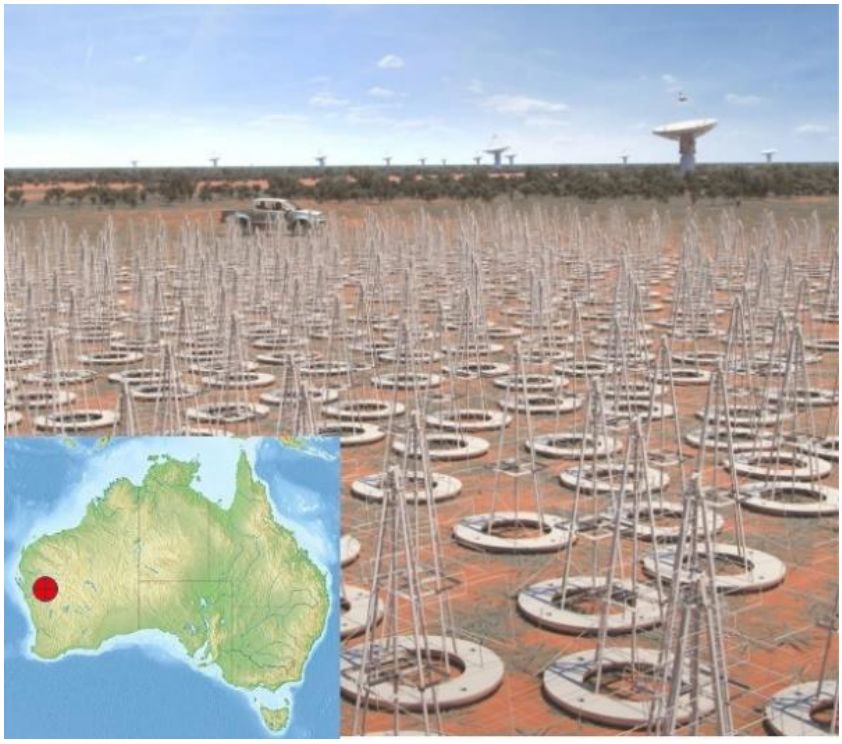

Figure 2-17: Murchison Widefield Array (MWA) Antennas in Murchison Shire of Western Australia, the first telescope for SKA [81]

In the recent SKA project, among the 4 stages, SKA1 low has 866 antennas, polarization factor of 4, 300 MHz bandwidth and a sampling rate of 1. The data rate estimated is about 100x109/s which is thousand times greater than MWA. For an hour, it produces 400 TB of data and for a day, it generates 10 PB of data [81]. It is to be noted that this data rate holds good for phase 1 only and when taking phase 2 into consideration, the data rate increases by 10 times this value which increases the SKA processing range on the whole to exa scale signal processing thereby leading to big data processing issues. So, though there are many ongoing researches in this regard, an optimal solution to handle these big data problems is the need of the hour, especially for correlating these Terabits of data in real time.

2.7 Summary

The Interferometry plays an important part in radio astronomy to identify the astronomical objects in the form of radio frequencies. Some neutral atoms and fast-moving electrons in galaxies and most of the gases are only identified by the radio telescopes. In radio astronomy, large radio antennas or radio telescopes are

employed independently or in an array structure to observe radiation coming from the space using interferometry and aperture synthesis techniques. The interferometry technique improves the angular resolution because the interferometers work based on the distance between the antennas but not on the size. The ongoing interferometer project called SKA is the largest interferometer so far and the design phase is targeted for two stages. The data rate of this SKA Interferometer is around 10PB per day and this is expected to be increased to 10 times higher value in Phase 2. Handling this big range of data involves exa byte digital signal processing which may require higher volume of hardware. Hence, it is important to address this big data issue to reduce the hardware for the astronomical digital signal processing.

CHAPTER 3: CORRELATOR DESIGN ANALYSIS

3.1 Interferometer Correlators

3.1.1 Correlators

Generally, correlation is defined as a measure of the similarity between two signals as a function of the time shift between them. In an interferometer, the antennas convert the electric field based on the distribution of brightness in the sky to its corresponding voltages [69, 82-85] and the spectral correlator performs cross multiplication between the input samples either before or after Fourier Transform and the integration of the output over a period of time called the Dump period [86] to calculate the mutual coherence function or visibility for each antenna pair. The group of visibilities is termed as a baseline. The cross-power spectrum of two signals can be obtained by taking Fourier transform for the cross-correlated functions [87-89]. The cross-correlation is carried out to find the similarity between the signals as a function of the displacement of one signal with respect to the other. Similarly, the auto-correlation is the cross-correlation of a signal with itself at different time period [90] .

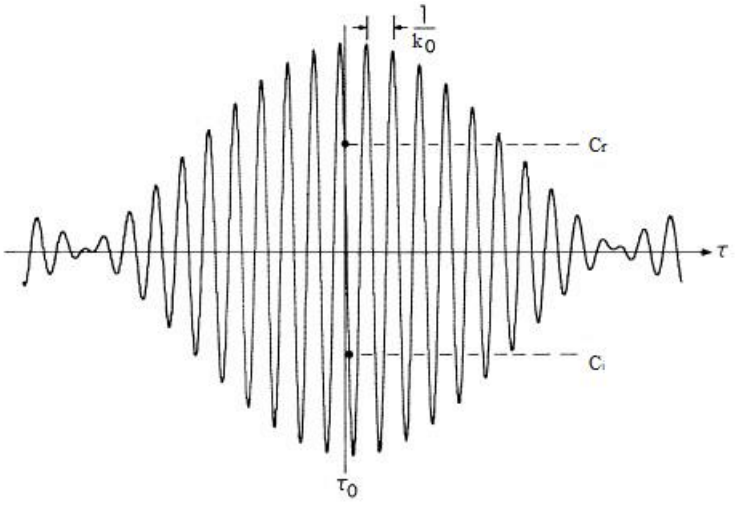

Figure 3-1: Cross correlation of quasi-monochromatic signal with rectangular passbands centred at k_o.

The cross-correlation $C_{xy}(\tau)$ of two real signals $x(t)$ & $y(t)$ and auto-correlation $A_{xx}(\tau)$ of signal $x(t)$ are given by the following equations,

$$C_{xy}(\tau) = \langle x(t)y(t+\tau)\rangle \quad (3\text{-}1)$$

$$A_{xx}(\tau) = \langle x(t)x(t+\tau)\rangle \quad (3\text{-}2)$$

where $\langle\cdot\rangle$ is the statistical average and τ represents the delay. In some cases, when $x(t)\,\&\,y(t)$ are narrow-band signals with a bandwidth of $\triangle k \ll k_0$ centered at k_0, and also the cross power spectrum $C_{xy}(\tau)$ is almost sinusoidal in τ , with period k_0^{-1} as shown in Figure 3-1 ,then $C_{xy}(\tau)$ can be represented as,

$$C_{xy}(\tau) = C_r cos2\pi k_0(\tau - \tau_o) + C_i sin2\pi k_0(\tau - \tau_o) \quad (3\text{-}3)$$

where τ_o represents the reference delay of τ. Also for a wide range of τ, the $C_{xy}(\tau)$ is specified with a single complex function as $RI_{xy}(\tau) = C_r + iC_i$,which defines the narrow band signal's complex cross power. Later, this complex cross power after astronomical calibrations is called as complex visibilities. There is no need to measure $C(\tau)$ for all τ but it is enough to calculate two nearby values of τ for τ_o and $\tau_o + \Delta\tau$, where $\Delta\tau = 1/(4k_0)$. This cross-power function is useful even for the non-sinusoidal signals that are not narrow band signals, by breaking the wideband signal into numerous narrow bands using a bank of filters and feeding the pair of outputs to a complex correlator as shown in Figure 3-2.

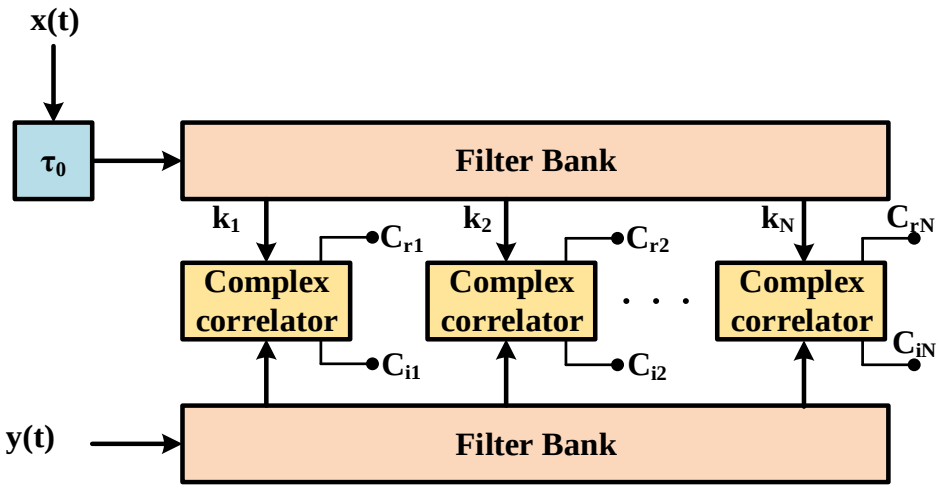

Figure 3-2: Block diagram of wide band complex correlator using narrow band complex correlator.

The output of all the correlators are then finally averaged over the full bandwidth and is given by the following equation,

$$RI_{xy}(\tau_o) = \lim_{N\to\infty} \sum_{n=1}^{N} C_{rn} + iC_{in} \tag{3-4}$$

The Filter bank correlators are more useful for spectroscopy in which the output of a specific complex correlator is stored individually rather than adding it. The Figure 3-3 shows the spectroscopic way of measurement, where the Discrete Fourier transform (DFT) is applied to the results of real cross correlation function of closely spaced delays at τ_o. The Fourier transform for correlation of two signals shown in equation (3-1) will give the cross-power spectrum $\tau_{xy}(k)$ which is given by,

$$ri_{xy}(k) = \int_{-\infty}^{\infty} C_{xy}(\tau) e^{-2\pi ik(\tau-\tau_o)} d\tau \tag{3-5}$$

Similarly, Fourier transform of the autocorrelation function shown in equation (3-2) will produce the signal power spectrum. The cross-power spectrum is mostly complex in nature, whereas the signal power spectrum is always real and positive. The complex cross correlation function is twice the Fourier transform of equation (3-5) in which the negative frequencies are truncated. The time shift of τ_o is inserted before transforming. This definition is convenient if C_{xy} peaks near τ_o, because ri_{xy} will then be nearly constant. The complex cross correlation is given by the equation (3-6) (for detailed derivation please refer the book Interferometry and synthesis in radio astronomy [6]),

$$RI_{xy}(\tau) = 2\int_{0}^{\infty} ri_{xy}(k) e^{2\pi ik(\tau-\tau_o)} dk \tag{3-6}$$

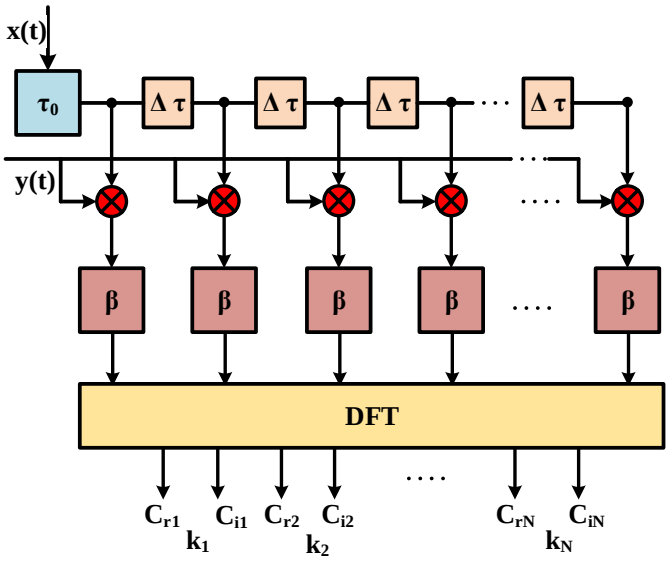

Figure 3-3: Block diagram of spectroscopic correlator with frequency analyser after the cross correlation, where the $\beta = \frac{1}{T}\int_0^T dt$.

It can be clearly seen that the correlator in Figure 3-3 approximates the equation (3-5) (right side) and by summing up the outputs, approximates the equation (3-6) (right side) for $\tau = \tau_o$. The overall operation of the spectroscopic correlator shown in Figure 3-2 is clearly defined by the following equation,

$$C_N = \sum_{i=0}^{2N-1} \left[\frac{1}{T} \int_0^T x(t - \tau_o - i\Delta\tau) y(t) dt \right] e^{-2\pi i k/2N} \qquad (3\text{-}7)$$

3.1.2 Digital Correlators

The digital technique is used to implement the spectral correlator since it's far better than the analog implementation when the stability and repeatability are the facts to be considered [90]. Also, the exact replication of digital circuits is possible, if large number of identical circuits are required at low cost. Moreover, for long baselines and wider bandwidths, only the digital delay lines have large ratio of length to resolution. To perform digital correlation, the analog input signal is converted into a digital input by using an Analog to Digital Converter [91-93]

which performs sampling, quantization and analog to digital conversion. The process of sampling and quantizing the signal is called as Digitization.

In the sampling process, the continuous time domain signal $x(t)$ is time sampled at equal intervals to convert it into a discrete time sampled signal $X(K)$, where K is the frequency sample number ranging from $0\ to\ N-1$. The sampling must be performed at the Nyquist rate [94] or faster to achieve lossless reconstruction of the signal. Then the sampled signal is quantised to one of the known finite set of values. The digitization can be performed in two ways, either the signal can be sampled first and quantized, or quantized and then sampled.

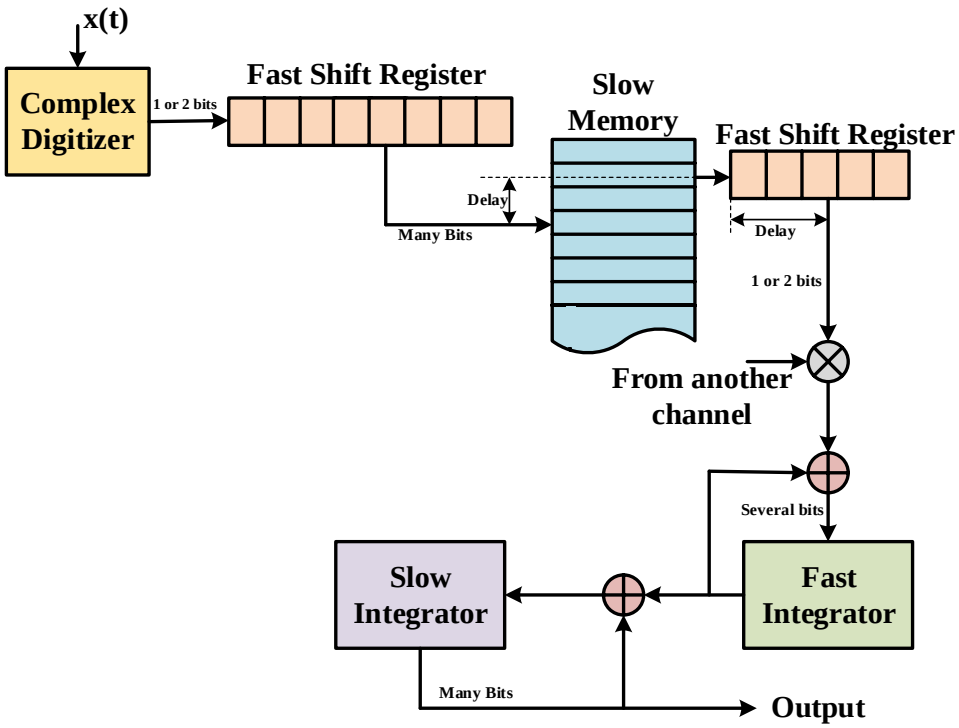

Figure 3-4: Block diagram of a simple digital correlator [95]

The digital implementation of a simple correlator [95] with multiplier delay line and integrator is shown in Figure 3-4. Normally, the memories and logics operating at high speed always occupy a lot of space and consume more power than the low speed ones. The delay lines used in Figure 3-4 use more slow speed memories and some fast shift registers to buffer the input and output. The integrator memory also uses the same logic to accumulate data or long time periods. The integrators and multipliers are the most area and power consuming parts in

correlators during correlating the signals from large array of antennas. For N number of signals, it requires nearly N^2 number of multipliers and integrators, $2N$ digitizers and delays to perform correlation. Moreover, in spectroscopic correlators, for K frequencies it requires $KN(N\text{-}1)$ multipliers and integrators to perform correlation. Therefore, the design of correlators for large interferometer should reduce the number of multipliers to crosscut the overall power and area. In VLA [34, 96] interferometer, for spectroscopic correlation of 256 frequencies, it used a buffer called re-circulator to store the samples temporarily and the same multiplier was timeshared among many correlators.

There are two approaches to build a spectroscopic correlator based on whether the frequency analysis must be done before or after the cross correlation. In the first approach, filter banks are implemented with analog circuits before the digitization and the later uses digital circuits after digitization. The cost of general correlator is estimated by the equation (3-8) [95].,where, Na is the number of antennas, Δk is the total bandwidth from these antennas, A_F is the total number of analog filter channels and CA_F is the cost for it, CD_F is the cost per unit bandwidth of K channel digital filter, number of post correlation DFT Pc_{DFT}, and C_c is the each cross correlator cost per unit bandwidth. It can be visible that if the number of antennas increases, the cost of digital implementation also increases. Thus, based on the equation 3-8 it's better to implement the more processing sections before correlation. Also, if the total bandwidth increases it is a good idea to use analog filters rather than using digital ones. Based on the above considerations, it's proved that the large spectroscopic correlators must be built with filter banks prior to the correlation to reduce the cost. This type of correlator design is called as FX-Correlator, and the filter banks implemented after correlation is termed as XF-Correlators.

$$Cost_{total} = Na\left[A_F CA_F + \frac{CD_F(K)\Delta k}{A_F Pc_{DFT}}\right] + \frac{\frac{1}{2}Na(Na-1)C_c\Delta k}{A_F K} \qquad (3\text{-}8)$$

3.1.3 XF-Correlator

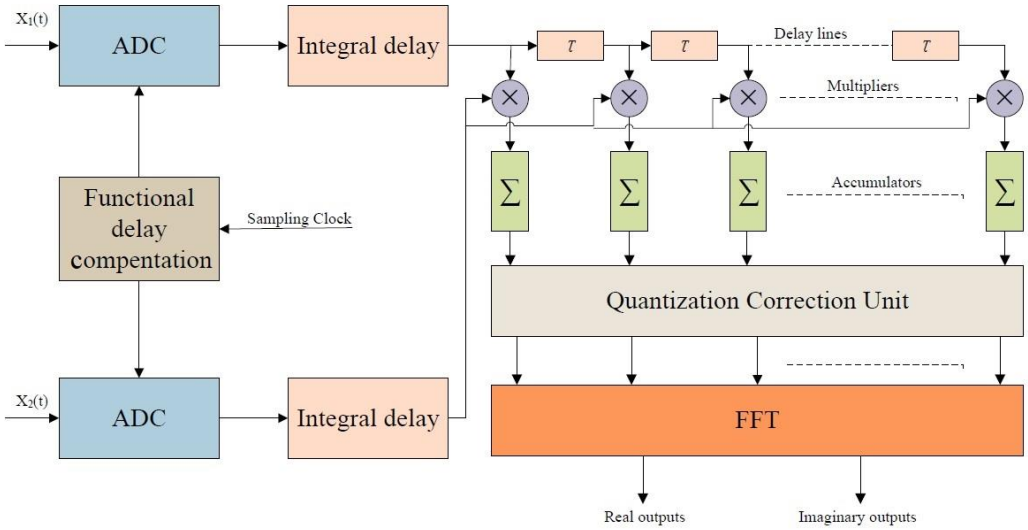

Figure 3-5: Simplified XF-Correlator

This type of Correlators [97, 98] initially cross correlate the signals obtained from the array of antennas in the X-section and later, the complex product obtained from this cross correlation is then converted into frequency domain in the F-section[99, 100] using Fast Fourier Transform (FFT). Normally, in lag correlators, the delay between the signals are introduced by varying the phase of the sampling clock and then the cross correlation is calculated for various delays by using the integral delay blocks and multipliers. After cross correlation, the value is integrated for some dump period. The normalized cross correlated values are passed to quantization correction and finally the cross spectrum is acquired by applying Fast Fourier transform for the quantized cross correlated function. The VLBI Correlator [101-103] and WIDAR Correlator [104, 105] are the best examples of XF interferometer Correlators used to correlate signals from large array of antennas. The advantage of this XF architecture is that, during data transmission between stations-based hardware and baseline-based hardware, it uses minimum bandwidth.

In Figure 3-5, the delay factor τ regulates the spacing for correlation function measurements and implemented with shift register to shift the multiples of sampling interval. The power of individual signals can be calculated by adding a self-multiplier for every signal after being digitized. Before computing the DFT, the quantisation correction on cross correlation is performed. The integrators

accumulate data for certain period before the start of a new measurement. For instance, 200MHz sampling rate with an accumulation time period of 1 sec integrates nearly 2×10^8 samples before computing the next measurement. The basic XF-Correlator structure in Figure 3-5 is a much simplified one than the practical structure which is more complicated.

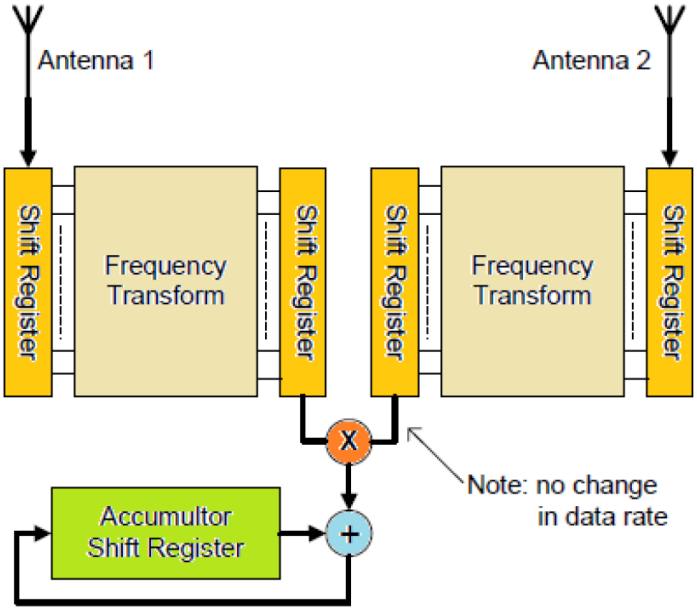

Figure 3-6: Basic FX correlator design proposed by Chikada [106]

3.1.4 FX-Correlator

The FX Correlator was developed by Chikada [106] in 1980s using FFT technique and its representation is shown in Figure 3-6. The FX Correlator [107-109] also produces the same output as the XF Correlator, but it reverses the operation by performing Fourier transform initially followed by the cross correlation [99, 110].

Initially, FFT is applied over the data from every antenna to transform them from time domain to frequency domain and later the cross power for all the channels are calculated to obtain the cross power spectrum [89, 107]. The use of FFT has the advantage that the number of output samples are equal to the input samples which reduces the number of CMACs to one for a baseline when the processing of input data is through non overlapping cells. But still, it requires a

register for storing the correlations per frequency channel. The Functional block diagram of FX correlator is shown in Figure 3-7. Earlier, for the frequency transform, the F-Engine uses only FFT which has a signal to noise degradation problem or an increase in the data rate. Later the poly phase filter bank [111] is introduced before FFT [107] which allows the impulse response of the channel to be greater than the length of FFT and makes a way to choose channel impulse response randomly. By using polyphase filter bank structure as shown in Figure 3-8, a minimum increase in data rate but will ease the way to achieve high quality channel response as that of XF Correlator. The interferometers like Nobeyama [112], VLBA[113] and GMRT [114] used FX architecture for their Correlator design.

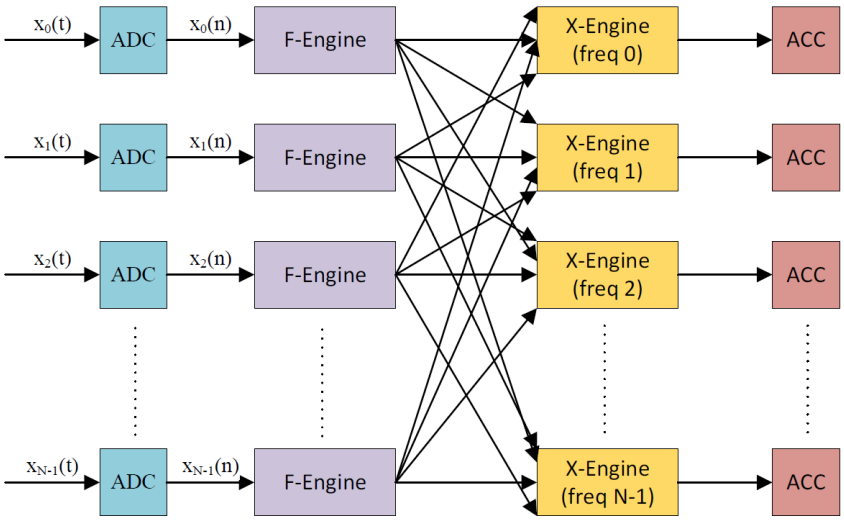

Figure 3-7: Functional block diagram of FX-Correlator

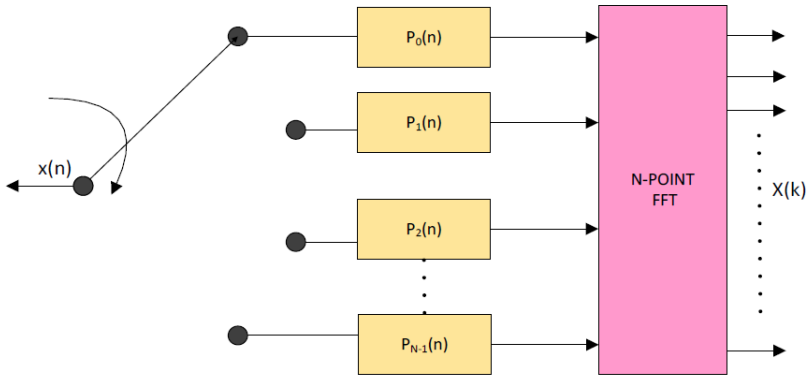

Figure 3-8: Simplified block diagram of a Polyphase Filter bank

3.2 Comparison of FX-Correlator and XF-Correlator

The F-engine in FX-Correlator works with a smaller block of data to control the spectral resolution. From this small block of data, there are N possible ways to construct the equivalent correlation function for the zero-lag component. To increase lags, there are only fewer possible multiplications available due to the data block boundaries. There is only one way to calculate the correlation function at $\pm(N-1)t_{int}$, where t_{int} is the time interval between the two samples and N is the number of samples. So, for the range of $\pm Nt_{int}$ the lag multiplications density has a triangular shape as a function of lag as shown in Figure 3-8(a). Therefore, the spectral response of this function is given by,

$$sinc^2(Nt_{int}ks) = sinc^2(n) \tag{3-9}$$

where $ks = \frac{n}{Nt_{int}}$ and n is the number of spectral channels.

The spectral resolution of XF-Correlators depends on the correlation function length. The lag multiplication density is basically uniform because the segment data correlation function is much greater than the block length and the spectral response become $sinc(Nt_{int}ks)$ or $sinc(n)$ which is shown in Figure 3-9. The integral over frequency of spectral response for both FX-Correlator and XF-Correlator is unity. The spectral feature's peak amplitude is based on the position it falls which is narrow than the resolution with respect to the frequency channels. The peak amplitude is decreased to $sinc^2\left(\frac{1}{2}\right) = 0.41$ for FX-Correlator and $sinc\left(\frac{1}{2}\right) = 0.64$ for XF-Correlator when a line falls in-between two channels and this effect is called as scalloping [115] which can be moderated by zero padding technique to get an interpolated spectrum. In full nonlinear quantization correction, it is necessary to estimate the correlation function from F-Section. Therefore it's important to pad N zeros to the spectrum to calculate the exact result [116].

Both the FX-Correlator and XF-Correlator have the same multiplier counts and the only basic difference between them is the density weighting in the lag domain. The FX is capable to accommodate two times of lags as XF, but this lowers

the density. The Signal to Noise Ratio (SNR) for both systems is the same for the continuum source. Also, the SNR is same for very narrow bandwidth source as both have the same multiplier count. But, there is a slight difference in the response for the signals with equal line width and resolution and the spectral amplitude is decreased by about 0.82 [117]. The distribution of lags in the FX-Correlator causes this small problem.

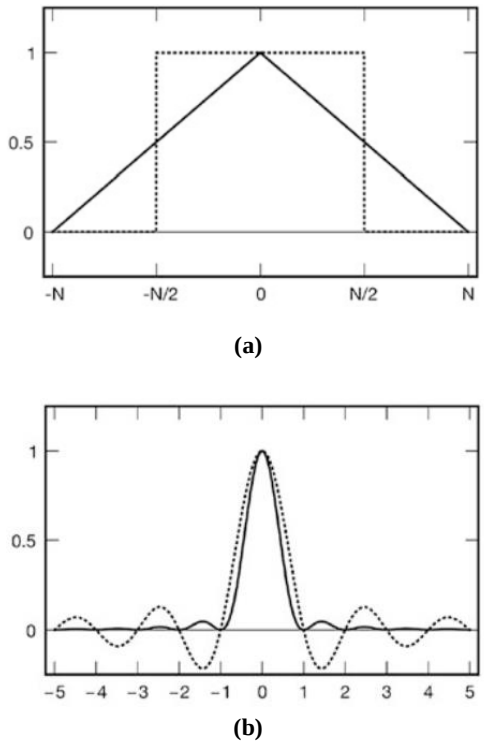

Figure 3-9: The dotted line represents the XF-Correlator and the solid line shows the FX-Correlator in both (a) & (b). (a): The intrinsic weighting function for FX-Correlator and XF- Correlator. Here N is the segment size which is assumed to be same for both FX and XF for compression purpose. (b): The spectral response for FX-Correlator and XF-correlator sinc function.

The FX-Correlator covers larger range with smaller multiplications at $lag(ks) \pm \frac{N}{2}$ as shown in Figure 3-9. To overcome this issue, the block processing segments in the F-section of FX-correlator can be overlapped to 50% which almost retrieves the lost SNR with double the processing time [118, 119], or average the spectrum channel which cost the F-section resolution capacity. But when using the polyphase filter shown in Figure 3-8 in the F-section, the FX-Correlator will have very small SNR loss and narrow spectral lines scalloping.

	Freq.band Available	Freq.band Data rate	Overall Data rate	Lags per Freq.band	Multiply and Accumulate ops/sec in one baseline
XF-Correlator	1	S	S	w.n	w.n.S
FX-Correlator	n	S/n	S	1	S

Table 3- 1: Input and Output data rates, dump size and dump time of correlators in SKA telescopes [108].

Also, in the FX-Correlator, the signal is split into number of channels with useful frequency resolutions and then is correlated separately. This helps us to calculate the cross-power spectrum directly which is the most advantageous factor. The FX Correlator is advantageous when using large antenna arrays because the multiply and accumulate unit is not dependent on the frequency channel count. For instance, consider a hypothetical XF correlator with complex input data at a sample rate S and a total useable bandwidth of S. If the final frequency resolution is to be S/n then for an XF correlator, a total of w.n lags of the correlation must be measured, where w = 1 for Rectangular window and 1.7 for Blackman window to prevent spectral leakage. But in FX correlator, it divides the useable bandwidth into n equal frequency bands. Each band is S/n wide with a sample rate of S/n. A single multiplier and accumulator (MAC) is needed for each of the n frequency bands. However, the rate at which each of the MAC units must operate is reduced by a factor of n. Table 3-1 shows the relationship between the operations of multiplier and accumulator in FX-Correlator and XF-Correlator [108]. Here, it is considered that the transition bandwidths as a fractional of total bandwidth are same for the XF and FX frequency channel.

In Table 3-1, n represents the number of frequency channels obtained from the input signal, S is the overall data rate and w refers to the windowing technique which helps to stop the spectral leakage. The data rate to both XF and FX correlators are the same in Table 3-1, but this is true only if the transition bandwidths as a fractional of total bandwidth are same for XF and FX frequency

channel. The aliasing and band edge effects are also eliminated as the data rate per frequency band is reduced by a factor of n. Even though these advantages are seen, the FX Correlator has higher data rate and the splitting of the signal into frequency channels requires additional hardware[120]. For example, after processing two input signals using FFT, convolution can be attained with point by point multiplication. The resultant circular convolution complications produced by this method are controlled by windowing and overlapping the data or by using a linear convolution. But the output data rate is increased by both the methods when compared to input data rate. The word length growth by means of FFT is the second source of increase in data bandwidth.

But these problems can be overcome by using a polyphase filter bank and FFT together as discussed in [108, 120]. Also, further improvements like the use of high precision Analog to Digital convertor and a Quantiser with a level control at the DFT filter bank output to perform fine quantization as that of XF Correlator help to prevent the escalation of the sample bit size.

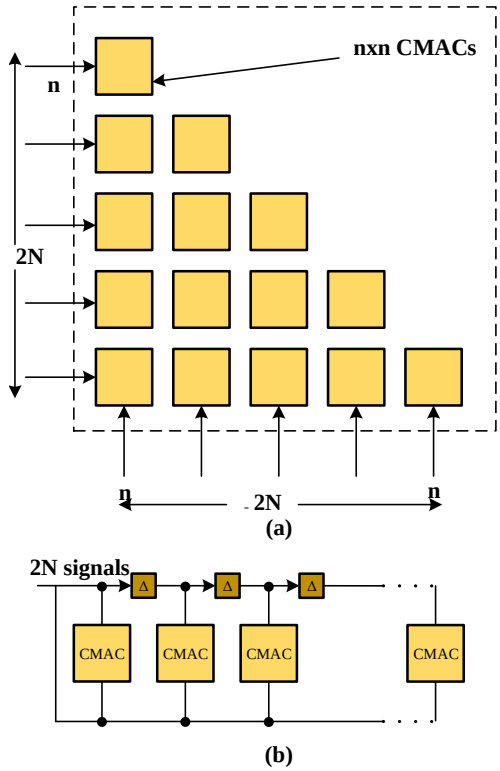

Figure 3-10: (a) Matrix Architecture with n ×n CMACs to process 2N signals. (b) Pipeline Architecture with delay blocks.

Comparison between the conventional XF, FX and HFX Correlators has been done in [121] for the space based interferometry and the conclusions arrived at, by the author's observation states that the FX Correlator seems to be the best option. Also in [42, 122, 123] the authors recommend the use of FX architecture to design a Correlator for large arrays using ASIC flow. In addition, the GPU based Correlator used in CHIME Pathfinder radio telescope [86] suggests the use of FX correlator. From this it can be easily concluded that irrespective of the implementation (FPGA, ASIC or GPU) the FX-Correlator is preferred on designing correlators for large arrays.

3.3 Architectures for X-Section in FX-Correlator

The architecture for X-section of FX-Correlator is mainly classified into two types, namely the matrix type and the pipeline type based on the arrangement of the Complex Multiplier and Accumulation unit (CMAC, refer section 3.4) in a triangular or a chain fashion structure respectively as shown in Figure 3-10. The CMAC is the basic cell used in X-section to perform Complex multiplication between the two complex samples from the filter bank in the F-section and accumulate the result over time. Figure 3-11 portrays two types of CMAC cells with dedicated register and with a memory bank for accumulation.

In the matrix architecture there are three types, in the first method a dedicated CMAC is used for every individual baseline, and in the other two types of matrix structure, the CMACs are shared among baselines. The second method uses an input data buffer which stores the data required for one correlation and at the end of the integration time, the CMAC's output data is read, buffer is cleared and the data for the next pair of antennas are loaded in the data buffer for the next correlation process to start over. Whereas, in the third method, the CMAC reads data from an accumulation register for each clock cycle, processes the data and stores the result back into the accumulation register. The reuse of CMACs for multiple baselines under the pipeline type, also uses the same methodology but involves sending the samples to the CMACs serially on a single bus with a specific delay where the delay is proportional to the block size of the data being sent from a signal. The five sub classifications of the architectures are based on the allocation

of a dedicated CMAC for each baseline and the reuse of CMACs among baselines are depicted in Figure 3-12.

The difference between the two types lies in the length of the delay between the CMACs. In the Matrix structure, the delay is equal to the number of samples in a single integration and hence requires all the blocks of data from a signal to have the same number of samples. Instead, in the latter category, the delay is based on each clock cycle where a data sample from each antenna is being fed to the CMAC serially on every clock cycle from an accumulation register.

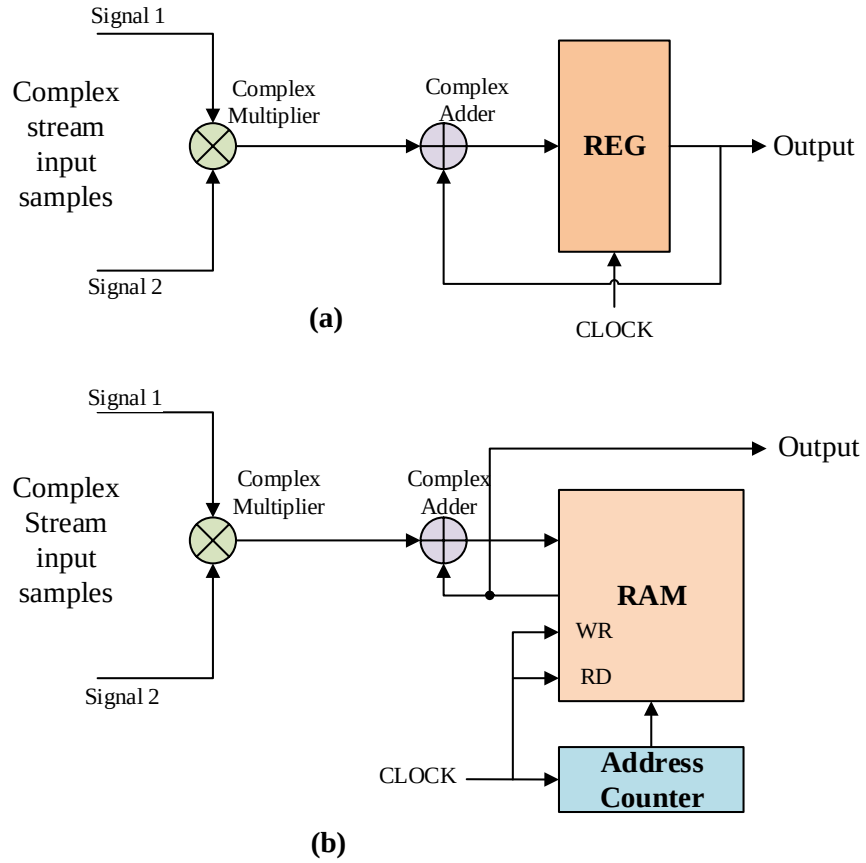

Figure 3-11: (a) Complex Multiplier and Accumulator cell (CMAC) using dedicated register for accumulation. (b) Complex Multiplier and Accumulator cell (CMAC) using memory bank for accumulation.

A summary of all the five architectural designs, is shown in Table 3-2 [124]. In the first architecture, it uses a dedicated CMAC for each baseline and does not require memory for buffering, resulting in less power consumption. Whereas, all

other architectures use memory for buffering which increases the overall power consumption.

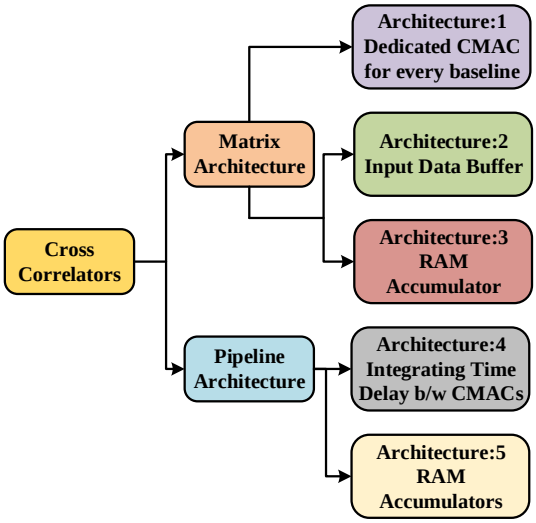

Figure 3-12: The different architectures based on matrix and pipeline structures for performing cross-correlation.

Architectures:	Arch:1	Arch:2	Arch:3	Arch:4	Arch:5
No. of antennas	2,024	2,025	2,040	2,000	2,000
CMACs per IC	30,976	22,500	10,404	2,001	667
Channels per IC	284	3	24	1	1
Clk freq (Hz)	2.84E+07	1.13E+08	2.4E+08	4.00E+08	4.00E+08
Input Rate per IC (b/s)	4.00E+10	4.86E+09	3.92E+10	6.40E+09	6.40E+09
Output Rate per Ic (b/s)	4.33E+09	1.26E+10	1.23E+10	1.03E+10	7.71E+09
Power per IC (W)	2.25	7.73	17.05	11.49	1150
Total No. of ICs to process all Baselines in one subband	276	1	8	1	3
Total No. of ICs required in a system	9,718	3,333	3,333	10,000	30,000
Memory Power (%)	0%	18.7%	63.5%	82.6%	94.1%
Memory area (%)	0%	25.6%	67.3%	93.9%	97.5%
Total Power (W)	21,859	25,771	56,823	114,873	344,873

Table 3- 2 Input and Output data rates, dump size and dump time of correlators in SKA telescopes [124]

On comparing pipeline architectures (4 & 5) with the other three types, the system requires a greater number of ICs (Integrated circuits (ASICS)) that used to perform the complex multiplication with accumulation operation and consumes more power. The percentage of area occupied in the die by the memory is about 67% for architecture 3 and more than 94% in architectures 4 and 5, thus causing high power consumption. The architecture 2 occupies around 25% of total die area for the memory and consumes only 19% of the total power. Compared to architecture 1, architecture 2 consumes slightly higher power and reduces the overall ICs required by the system and hence used to design the straw-man correlator design using 90 nm CMOS technology [124].

The choice of shorter gate length technology which is capable to operate in higher clock speed helps to increase the data rate and reduce the number of ICs required to process the signal from all antennas. Henceforth, from Table 3-2 it has been concluded that the power consumption in a cross correlator is minimal if there are less memory operations. The RAM accumulators involve more memory operations and hence it should be avoided in both matrix and pipeline structures. Also, the pipeline architecture consumes more power as it involves more memory read and write cycles and hence proving that the Matrix structure (Arch:1 and Arch:2) is much better than the other architectures discussed in Table 3-2.

3.4 Complex Multiplier and Accumulator (CMAC)

CMAC, the basic unit in all X-section architectures of FX-Correlators, performs complex multiplication between two complex inputs and accumulate the multiplied complex output over a certain defined time period (Dump period). The complex multiplication can be implemented in three methods: Cartesian [125], Karatsuba [126], and Polar [127]. Cartesian method is the direct method of performing the complex multiplication using four multipliers, an adder and one subtractor. The Complex multiplication of two complex number $(M_r + iN_i)$ and $(O_r + iP_i)$ is given by the equation,

$$\begin{aligned} CM_{Cartesian} &= (M_r + iN_i) \times (O_r + iP_i) \\ &= [(M_r \times O_r) - (N_i \times P_i)] \\ &+ i[(M_r \times P_i) + (N_i \times O_r)] \end{aligned} \quad (3\text{-}10)$$

In Karatsuba multiplication, it calculates three intermediate functions involving multiplication initially and then the final outputs are calculated using subtractors. The intermediate functions are calculated as follows,

$$KM_1 = (M_r \times O_r) \quad (3\text{-}11)$$

$$KM_2 = (N_i \times P_i) \quad (3\text{-}12)$$

$$KM_3 = (M_r + N_i) \times (O_r + P_i) \quad (3\text{-}13)$$

Finally, the real and imaginary outputs of the multiplication are calculated by subtracting the intermediate functions as shown in equation (3-14 & 3-15). In total, using this method requires three multipliers, three adders and two subtractors.

$$KM_{real} = KM_1 - KM_2 \quad (3\text{-}14)$$

$$KM_{imag} = KM_3 - KM_1 - KM_2$$

Or (3-15)

$$KM_{imag} = KM_3 - (KM_1 + KM_2)$$

If the multiplication inputs are in polar coordinates whose magnitude and phase are represented as $m = \sqrt{x^2+y^2}$ & $\theta = \tan(\frac{y}{x})$ respectively, then the multiplication can be performed by adding the phases and multiplying the magnitudes, given by the following equation,

$$ZM_{Polar} = \left(m_1 e^{i\theta_1} \times m_2 e^{i\theta_2}\right) = m_1 m_1 e^{i(\theta_1+\theta_2)} \quad (3\text{-}16)$$

In the polar method of multiplication, the addition needs to be converted to the cartesian coordinates before adding. The conversion involves some extra hardware resources for the calculation of $\sin(\theta)$, $\cos(\theta)$ and two multiplications. This makes the use of polar multiplication unproductive for complex multiply and accumulation units in large interferometers, which reduces the performance and increases the design cost.

3.5 Review of hardware reduced Multipliers

The wise choice of multiplier for the power efficient correlator architecture will further reduce the power dissipation and area. The very basic multiplier used to perform complex multiplication is the Array multiplier. Several multiplier algorithms have been implemented to improve the performance and to reduce the design complexity in terms of critical path delay, compact-area and low power consumption. The fast multiplier algorithms such as Dadda-tree, Wallace-tree, Modified-Booth algorithm and Vedic multiplication algorithm are used to increase the multiplier efficiency and to reduce the complexity on calculation.

3.5.1 Array Multipliers

The array multiplier [128, 129] has a regular structure, which uses a normal array of half adders and full adders to add the partial products produced by an array of AND gates. A $M \times M$ multiplier requires $M \times (M-1)$ adders to add.

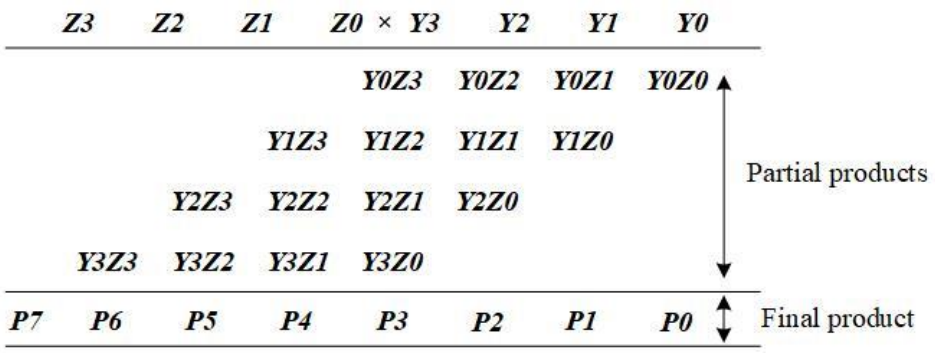

Figure 3-13: Basic 4×4 *multiplication.*

The delay of a normal array multiplier is given by,

$$D = 2M \times \text{Adder delay} \tag{3-17}$$

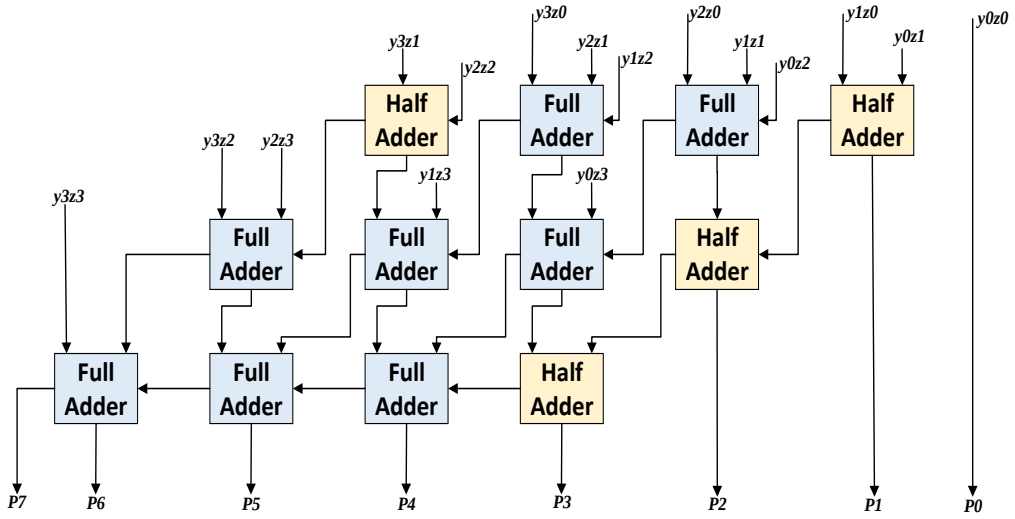

Figure 3-14: 4×4 *array multiplier using fast carry save adder. The partial products yizj are generated by AND gate arrays.*

Let's consider the multiplication of two four-bit numbers as shown in Figure 3-13. Here, $YiZj$ are the partial products generated using the logic AND gates, and Pk are the final products after adding the partial product rows, where $i\ and\ j$ ranges from 0 to $M-1$ and k ranges from 0 to $2M-1$ and $M=4$ in this case. Fast array multipliers use carry-save adders to perform the addition of partial products which can pass the carry to the next stage to improve the speed but yet has a high delay and occupies significant area. The Figure 3.14 represents the block diagram of an array multiplier architecture using carry save adder to perform the 4×4 Multiplication in Figure 3-12.

Using array multipliers to design the CMACs will increase the design complexity and power consumption of large interferometer correlators. The delay, complexity and power consumption of array multipliers shall be optimised with reduction tree structures or using other multiplier algorithms.

3.5.2 Optimisation methods for Multipliers

There are several optimization techniques available to reduce power, area and delay in multipliers. In large Interferometer like SKA-LOW, the multipliers used in the correlator design should be well balanced on all these three aspects. A single gate count increase in one multiplier will have a big impact on the total area and power of the overall design. The comparison study on different fast multipliers [130-134] shows that the Booth multiplication in combination with Wallace or Dadda tree reduction algorithms are well balanced on power, speed and delay. The Vedic multipliers [135-138] reduce the number of stages required and increase the speed of multiplication but increases the required hardware.

3.5.2.1 Wallace-tree and Dadda-tree reduction technique

The Multipliers based on the tree reduction technique use the concept of Carry save adder to perform multiplication by decreasing the critical path delay through the long chain of adders. The Wallace-tree [139] and Dadda-tree [140] algorithms reduce the number of Half-adders and Full-adders required for adding the partial-products in the array-multiplier. This reduction of adders reduces the hardware complexity and cell-routing area in the multiplier structure.

The Wallace-tree algorithm initially calculates the partial-product matrix generated from the AND gate arrays similar to array multiplier and then compresses the partial-product rows into two. Finally using fast adder, it adds these two rows to generate the expected output. The Wallace-tree reduces the number of partial-products as soon as possible by combining the partial-products with the same weights in the reduction stage using full-adders and half-adders until it becomes two rows. In this reduction process, the present sum bits are driven to the same position in the next-stage and the present carry-bits to the next-stage succeeding position as shown in Figure 3-15. The Wallace tree reduction method uses three steps as follows:

Step 1: Perform logical AND operation between or multiply every bit of first number with each bit of the other number to produce the partial products of size PP. Based on the multiplied bit position, the weights of wire differ. The

weight is the digit radix carried by that wire. For instance, $y_i z_j$ is the product of two bits in the binary numbers y and z, where i and j are the bit positions and the weight is $2^i 2^j = 2^{i+j}$. Therefore, the weight of $y_i z_j$ is 2^{i+j}.

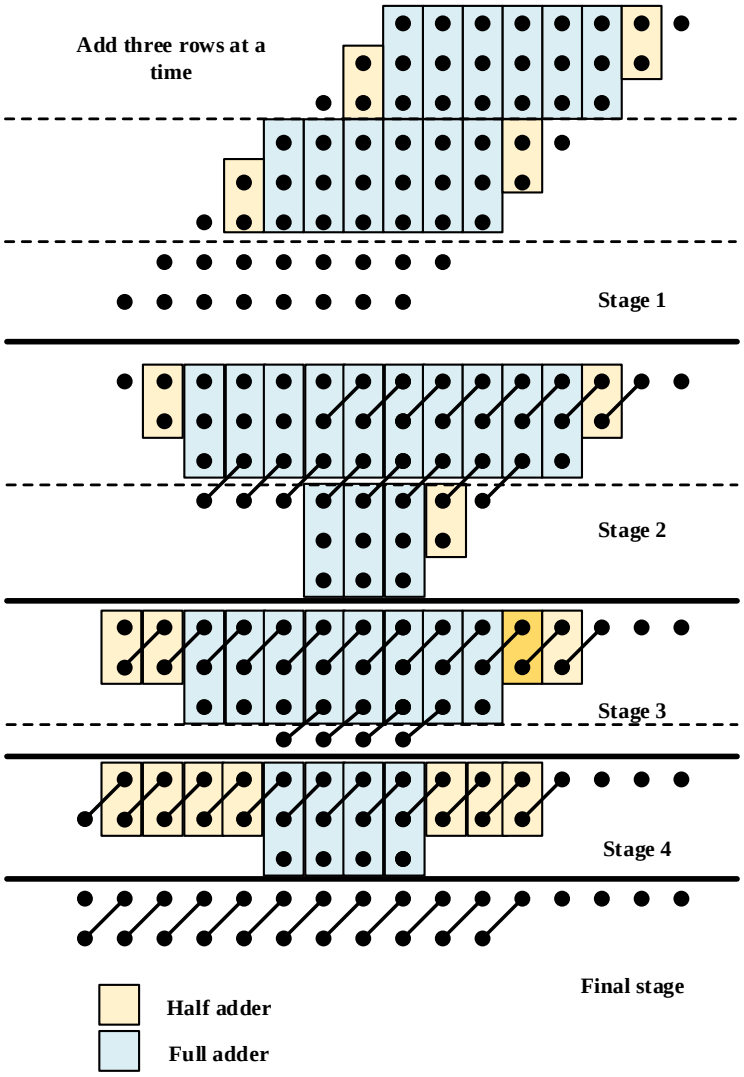

Figure 3-15: 8×8 *Wallace-tree multiplier operation using dot diagram.*

$$PP = no.\,bits\ in\ first\ number \times no.\,bits\ in\ second\ number \quad (3\text{-}18)$$

Step 2: Deduct the partial product rows to two by using full adders and half adders. Input, three wires having same weight to a full adder, two wires having same weight to half adder and one wire to next layer as shown in Figure 3-15 Stage-1 to Stage-4.

Step 3: Finally use some fast adder to add the grouped wires in the final stage as shown in figure 3-15.

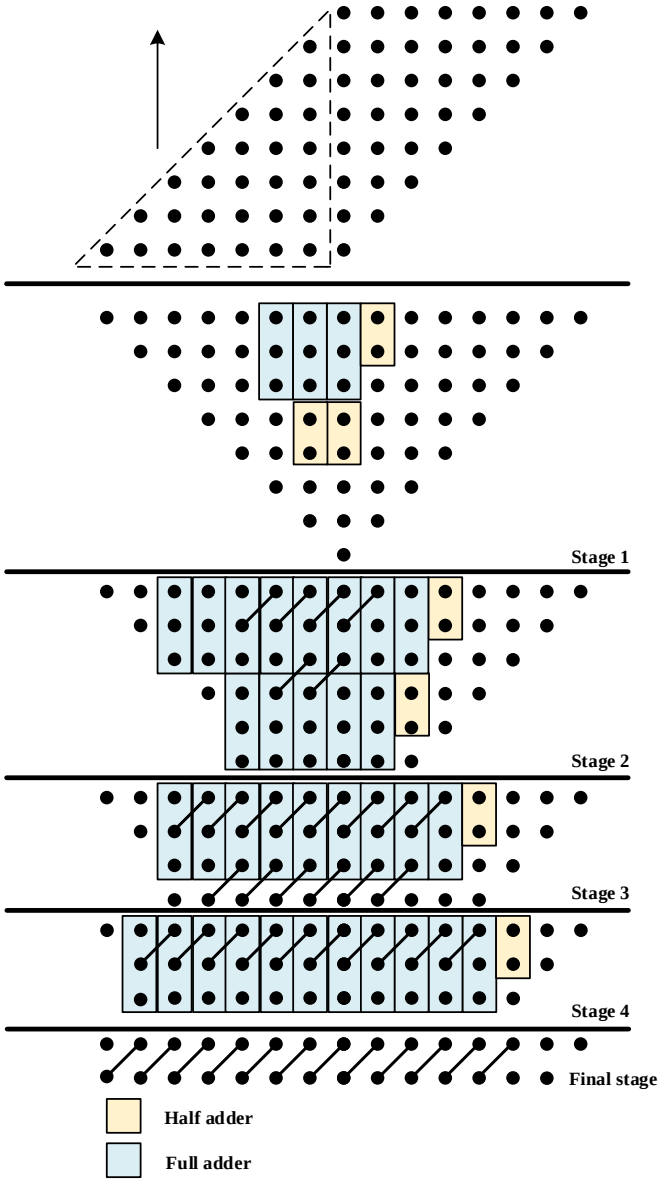

Figure 3-16: 8×8 *Dadda-tree multiplier operation using dot diagram.*

The advantage of using Wallace tree reduction is that it has a propagation delay of $(1) \times Adder\ delay$ in each layer. Hence the delay is considerably reduced in Wallace-tree multiplier and is given by the equation (3-19).

$$D = \log(M) \times \text{Adder delay} \qquad (3\text{-}19)$$

If the ratio between the equations (3-17) and (3-19) is considered, the delay of an array multiplier 2(M) is reduced to more than a factor of ten and improved gain in the throughput for the Wallace tree.

The Dadda-tree reduction algorithm is almost similar to the Wallace -tree structure with a slight difference in utilising the adders. In the initial stage, it distributes the partial-products to the rows horizontally using the half-adders and in the later stages, it uses full-adders. This difference in the selection of adders in different stages reduces the logic components required to calculate the multiplication in Dadda-tree method. Comparatively, Dadda-tree uses less hardware and provides faster response to some extent compared to the Modified-Wallace-tree structure, with the Modified-Wallace-tree being more hardware-efficient than the Normal-Wallace-tree but at the cost of response-time. The Figure 3-16 shows the operation of Dadda tree reduction method using dot diagram on the partial products generated.

The Dadda-tree follows the same three steps as Wallace tree on the reduction process. But in Step 2, the reduction process has some additional complex rules to obtain the optimal product than Wallace-tree reduction. It attempts to minimise the gates used and delay required for the input and output. Also, in Step 3, it requires a slightly bigger adder to obtain the final result. The reduction process is governed by the sequence d_i which is the maximum height of the wire and is defined by,

$d_1 = 2$ and $d_{i+1} = floor(1.5\, d_i)$. which produce the sequence, (3-20)

$$d_1 = 2, d_2 = 3, d_3 = 4, d_4 = 6, d_5 = 9, d_6 = 13, \ldots$$

A largest value for i is always chosen as the initial value so that the $d_i < \min(m1, m2)$, where $m1, m2$ is the multiplier and multiplicand bit position values. The main aim of the algorithm is to minimise the height of every individual column in each stage i to maintain the height either equal to or less than the value of d_i.

The following rules have been applied in the reduction path of Dadda-tree algorithm.

Rule 1: If the height of the column c_j is less than d_i, then no reduction is required in that stage for that column and move to next column c_{j+1}.

Rule 2: If the column height $c_j = d_i + 1$, then employ a half adder to add the top two partial products in that column. The sum comes to the same column and the carry is forwarded to the top of next column c_{j+1}.

Rule 3: For other conditions, employ a full adder to add the top three partial products and place the sum in the same column and forward the carry to the top of next column c_{j+1}. Restart the c_j from step 1 until the rows are reduced to two.

The logic delay of the Dadda-tree is almost equal to the delay of the Wallace-tree multiplier as shown in the equation below,

$$D \cong \log(M) \times \text{Adder delay} \tag{3-21}$$

3.5.2.2 Booth Algorithm

The number of adders required is based on the number of partial products generated in the initial stage. The partial products are generated using logic AND gate arrays or Booth-algorithm [141] or Modified-Booth-algorithm [142]. The Booth algorithm reduces the partial products generated for the multiplication which further reduce the number of adders required. The Booth algorithm (Radix-2) makes signed multiplication to be implemented in the hardware easily and speed up the process of multiplication. In this algorithm, the recoding technique is applied to the multiplier and the multiplicand is unchanged. In the recoding of multiplier, every individual digit is assumed to have zero, negative, and positive value and these are expressed as encoded signed digits (SD). The signed digits 0 and +1 are represented as 0 and 1, but the signed digit -1 is expressed as the equation (3-22) [143].

$$y = -y_{m-1}2^{m-1} + \sum_{i=0}^{m-2} y_i 2^i \qquad (3\text{-}22)$$

The procedure to implement the Booth recoding is as follows and represented in Table 3-3 where the y_i and y_{i-1} are the pair of numbers, and z_{i-1} is the recoded digit:

Step 1: The order starts from the Least Significant Bit (LSB) to the Most Significant Bit; every 0 digit of the actual number is replaced with 0 of the recoded value till a 1 appears.

Step 2: Once the 1 is read, add 1 in that position of recoded value and skip all the 1's which appear after that until reading 0.

Step 3: After the 0 is encountered replace it with 1 and repeat the step 1.

y_i	y_{i-1}	Z_{i-1}	Value	Condition
0	0	0	0	String of 0's
0	1	1	+1	String of 1's End
1	0	1	-1	String of 1's beginning
1	1	0	0	String of 1's

Table 3- 3: Recoding procedure in Booth algorithm [144]

After the recoding procedures, zero padding to LSB of the multiplier is done and 2-bit pairing from LSB to MSB is done. If the pair is 00 or 11, no action is required and skipped to the next pair. If 01 is encountered, then the multiplicand is added to the partial product and if 10 is detected, then the multiplicand is subtracted from the partial product. This procedure is repeated from LSB to MSB. Even though the Booth multiplier is fast, it causes an inconvenience in the design of Parallel multipliers as it has a variable behaviour in the adding and subtracting operations. In addition, the algorithm is not effective if the number has isolated 1's.

These disadvantages are addressed in the Modified-Booth algorithm or also called as Radix-4 Booth algorithm which do 3-bit pairing on the multiplier. The Modified-Booth algorithm reduces the number of partial products required for multiplication into half with Radix-4 recoding technique. In this method, the sign bit is extended to one position to make the string even and 0 is appended in the multiplier LSB. Based on the value of vectors, every partial product scaling factor is estimated as 0, +y, -y, +2y or -2y and it is represented in the recoding Table 3-4.

y_{i+1}	y_i	y_{i-1}	Partial Product scaling factor
0	0	0	0
0	0	1	1
0	1	0	1
0	1	1	2
1	0	0	-2
1	0	1	-1
1	1	0	-1
1	1	1	0

Table 3- 4: Recoding procedure in Radix-4 Booth algorithm (Modified-Booth algorithm) [144]

Based on this, the partial product rows are generated using the partial product generator (discussed in Chapter-4) and arranged based on the simplified sign extension method [145]. Finally, the partial products are summed to obtain the final product.

3.6 Summary

The FX-correlator is the best choice for correlation of signals in large interferometers since the multiply and accumulate unit is not dependent on the frequency channel count. The different correlator architectures used in radio interferometers have been discussed in this chapter in which the Matrix architecture

has more advantages than the pipeline architecture. Moreover, in matrix architecture, the RAM accumulator type consumes more power and therefore, it should be avoided. The selection of Multiplier is more important in large interferometer correlators, as this is the basic component for calculating complex multiplications. A small gate count reduction in one multiplier makes a very big difference in the overall architecture design and hence, helps to reduce the overall power and area of the design.

CHAPTER 4: DESIGN AND IMPLEMENTATION OF DEDICATED CORRELATOR CELLS

This chapter details the novel architectural design of X-section for the FX-correlator for large interferometers. The optimisation process includes the design of new area efficient and power optimised multiplier used in the correlation cells, dedicated Correlator processing cells and the overall matrix architecture structure.

In this research approach, a dedicated correlator multiplier named as, Correlator-System-Multiplier-and-Accumulator (CoSMAC) and Processing element for IQ sampled signals (PE_IQ) are designed to produce two 16-bit integer complex multiplications within the same clock period. The optimization is achieved by utilising the conjugate complex symmetry relation between discreate Fourier transform (DFT) samples. Also, using this CoSMAC a new processing element is designed to calculate both the cross-correlation and auto-correlation functions within the same clock period.

A new multiplier design named as Modified-Booth-Wallace-Multiplier Design is proposed and incorporated into these CoSMAC and PE to further improve their performance. This power and area efficient dedicated correlation cells replace the conventional CMACs in the matrix architecture discussed in Chapter 3. This proposed architecture eliminates the redundant cells and reduces half the number of ASIC processor cells required to perform the complete correlation in large interferometers. This optimisation in ASIC reduces the memory requirement and the number of memory operations required in the correlation process. This in turn, reduces the overall power consumption required for calculating correlation in large interferometers.

The core idea of this work is to reduce the hardware requirement without degrading the speed and performance of a real-time correlator.

4.1 Design Considerations

The design optimisation is targeted only for the X-section of the FX-Correlator and hence some assumptions are made on the inputs for this section from

the F-part. It is assumed that the samples from the F-section are pre-processed with the Filter banks individually for each signal and are corner turned [146, 147]. Also, it's been assumed that all the input signals are quantized discrete frequency channel sequenced complex samples with real and imaginary components. The 8-bit word length is used for real and imaginary components which will gain high dynamic range and low quantization noise. The input registers are of 16-bit length and store a complex sample of two's complement number (8-bit real + 8-bit imaginary). The accumulation time period or the "Dump rate" is fixed for all the baselines of correlated data [148].

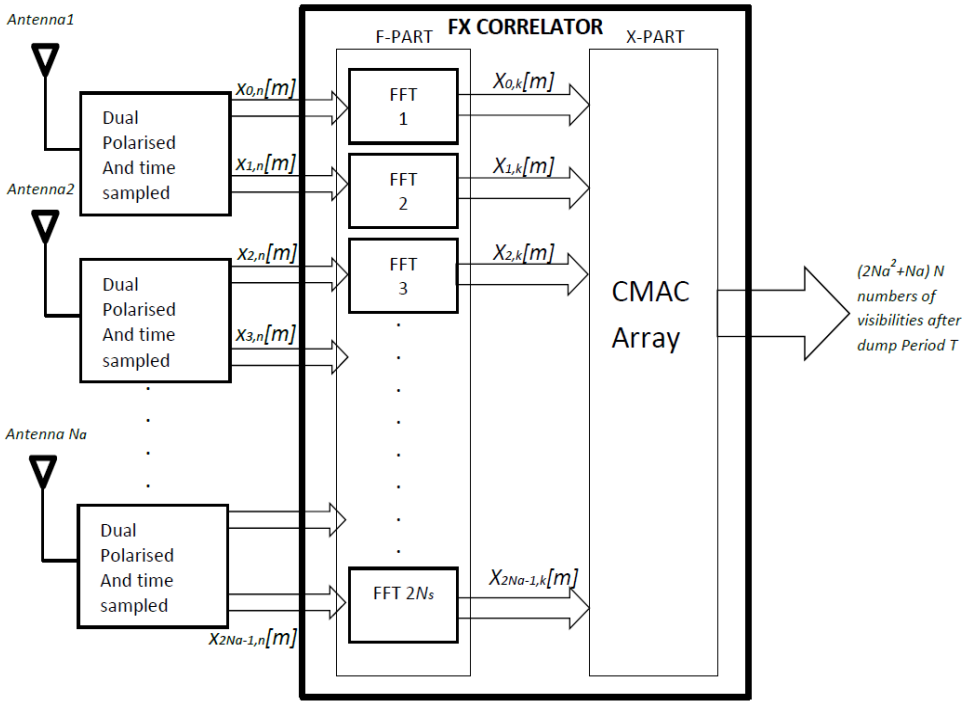

Figure 4-1: Generic architecture of an FX correlator using CMAC Arrays.

4.2 A generic FX-Correlator with CMAC

In this section, a generic FX-correlator and an existing CMAC are discussed along with the general computational matrices for analysis [149]. Let us consider that Na number of dual polarized antennas [150, 151] are producing a total of $2Na$ input signals for the correlation. This $2Na$ number of signals are oversampled at the rate of Ns and produces outputs defined as $x_{i,n}[m]$. The Figure 4-1 shows the general architecture of FX-Correlator in which Na is the number of dual polarized

antennas, i ranges from $0\ to\ (2Na-1)$, n ranges from $0\ to\ (N-1)$ where N is the number of discrete samples, and m varies from $0\ to\ (T-1)$ where m is the time slice index value for the accumulation dump period T. In F-section of the FX-Correlator, the Filter banks/FFT converts this time sampled $x_{i,n}[m]$ signals into the frequency sampled (DFT) signals $X_{i,k}[m]$, where k is the discrete frequency sample index varying from $0\ to\ (N-1)$. Therefore, in total, the overall possible frequency channels produced by the F-section is about Nfc. These Nfc channels are corner turned and fed to the X-section as inputs. In the X-section, it calculates T_{cc} number of cross-correlation baselines and T_{ac} auto-correlation baselines for the total of T_b baselines [123].

$$Nfc = N \times 2Na \tag{4-1}$$

$$T_{cc} = 2Na^2 - Na \tag{4-2}$$

$$T_{ac} = 2Na \tag{4-3}$$

$$T_b = 2Na^2 + Na \tag{4-4}$$

The cross-correlation is performed between each pair of distinct inputs and the auto-correlation is calculated by correlating a signal with itself to form the baselines. Considering all N channels, each baseline has N number of complex multiplications which are called as visibilities. Thus, for the total Na Number of antennas, the total visibility spectrum has T_v number of visibilities.

$$T_v = (2Na^2 + Na)N \tag{4-5}$$

The cross-correlation of two frequency sampled signals $X_{i,k}[m]$ and $X_{j,k}[m]$ calculated in the X-section is represented as Co_q, where i and j are the signal index ranging from $0\ to\ (2Na-1)$ and q is the cross-correlation baseline index ranging from $1\ to\ T_{cc}$. The cross correlation Co_q is calculated as discussed in Chapter 2 and is given by the following equation,

$$Co_q = \sum_{m=0}^{T-1} X_{i,k}[m] \times X_{j,k}[m]^* \tag{4-6}$$

For computational example, let's consider two frequency signals $X_{0,k}[m]$ and $X_{1,k}[m]$ from $X_{i,k}[m]$ signals, where i ranges from $0\ to\ (2Na-1)$ and k varies from $0\ to\ (N-1)$. Here, these two frequency signals have T temporal slices and is given by the following equations,

$$X_{0,K}[m] = \left\{ \begin{matrix} X_{0,0}[m], X_{0,1}[m], \cdots, X_{0,\frac{N}{2}-1}[m] \\ , X_{0,\frac{N}{2}}[m], X_{0,\frac{N}{2}+1}[m], \cdots, X_{0,N-1}[m] \end{matrix} \right\} \tag{4-7}$$

And,

$$X_{1,K}[m] = \left\{ \begin{matrix} X_{1,0}[m], X_{1,1}[m], \cdots, X_{1,\frac{N}{2}-1}[m] \\ , X_{1,\frac{N}{2}}[m], X_{1,\frac{N}{2}+1}[m], \cdots, X_{1,N-1}[m] \end{matrix} \right\} \tag{4-8}$$

Where, in both equation (4-7) and equation (4-8), $m = 0,1, \ldots, (T-1)$.

$$\begin{aligned} & Co_1 \\ & = Diag \left\{ \begin{bmatrix} X_{0,0}[0] & X_{0,0}[1] & \cdots & X_{0,0}[T-1] \\ X_{0,1}[0] & X_{0,1}[1] & \cdots & X_{0,1}[T-1] \\ \vdots & \vdots & \vdots & \vdots \\ X_{0,N-1}[0] & X_{0,N-1}[1] & \cdots & X_{0,N-1}[T-1] \end{bmatrix} \right. \\ & \left. \times \begin{bmatrix} X_{1,0}[0]^* & X_{1,1}[0]^* & \cdots & X_{1,N-1}[0]^* \\ X_{1,0}[1]^* & X_{1,1}[1]^* & \cdots & X_{1,N-1}[1]^* \\ \vdots & \vdots & \vdots & \vdots \\ X_{1,0}[T-1]^* & X_{1,1}[T-1]^* & \cdots & X_{1,N-1}[T-1]^* \end{bmatrix} \right\} \end{aligned} \tag{4-9}$$

Solving the equations (4-7) & (4-8) in (4-6) to obtain the cross-correlation baseline Co_1 which can be considered algebraically as the extracted diagonal elements of the product of an $N \times T$ matrix with the conjugate transpose of another $N \times T$ matrix, and can be given by the MATLAB diag function as shown in

equation (4-9). The rows in the output matrix (4-10) are called visibilities which are obtained by multiplying the time samples of two signals at a time instance m and accumulated over the dump period of T. Therefore, it requires N number of CMACs to calculate a single cross-correlation baseline.

$$Co_1 = \begin{bmatrix} X_{0,0}[0] \times X_{1,0}[0]^* + X_{0,0}[1] \times X_{1,0}[1]^* \\ + \cdots + X_{0,0}[T-1] \times X_{1,0}[T-1]^* \\ X_{0,1}[0] \times X_{1,1}[0]^* + X_{0,1}[1] \times X_{1,1}[1]^* \\ + \cdots + X_{0,1}[T-1] \times X_{1,1}[T-1]^* \\ \vdots \\ X_{0,N-1}[0] \times X_{1,N-1}[0]^* + X_{0,N-1}[1] \times X_{1,N-1}[1]^* \\ + \cdots + X_{0,N-1}[T-1] \times X_{1,N-1}[T-1]^* \end{bmatrix} \quad (4\text{-}10)$$

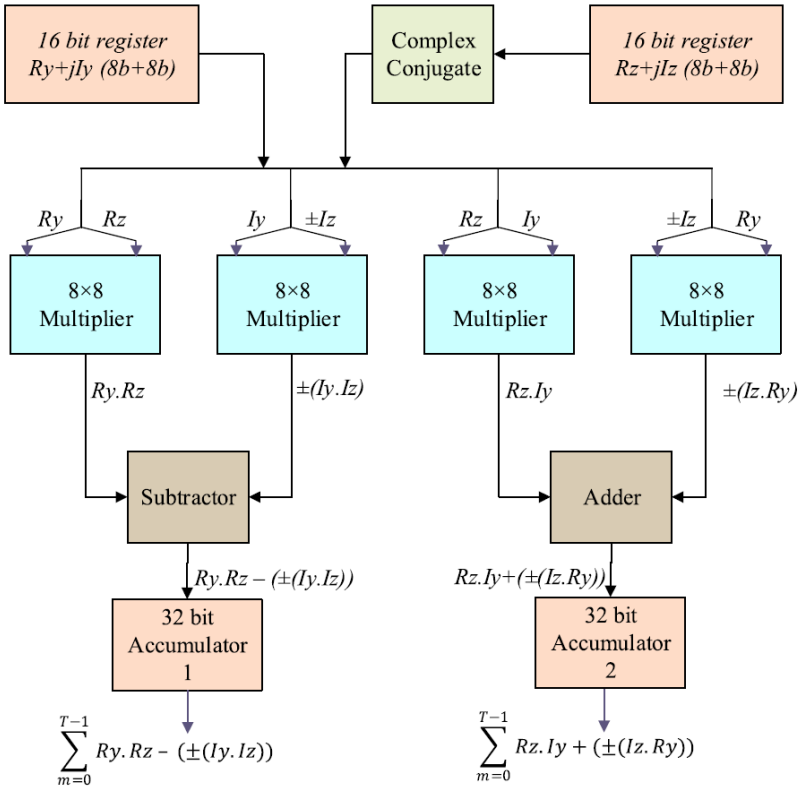

Figure 4-2: Conventional CMAC cell with the complex conjugate block at the input for calculating Correlations between two complex samples.

Therefore, for one baseline, if N =64, it requires 128 × 16 bits (8b real+8b imaginary) of input registers to store 128 samples and 64 CMACs to calculate the visibilities in parallel. Here, each CMAC has four real multipliers, an adder and one subtractor to produce a complex product. In addition to this, two accumulators

are required to integrate the product over the dump period T as shown in Figure 4-2. Hence, it requires 256 real multipliers, 64 adders, 64 subtractors and 128 accumulators to calculate one Cross correlation baseline. Apart from this, it requires an additional N implementation of conjugate operations (64 sign conversions) required for calculating one baseline.

4.3 Design of Dedicated Correlator Cells

The standard CMAC equation (4-10) is used to derive a novel algorithm for the new dedicated CoSMAC and further it is modified to PE. These correlator cells calculate the cross-correlation for $\left(\frac{N}{2}-1\right)$ conjugate frequency channels from the cross-correlation of the other $\left(\frac{N}{2}-1\right)$ channels in a baseline at no cost, which eliminates the transmission of $\left(\frac{N}{2}-1\right)$ channels from the F-section. Hence, it is not required to implement the storage and computations for the conjugate channels to produce the full visibility spectrum in real-time for image formation as conventional CMAC's.

4.3.1 Design of Correlator-system-multiplier-and-accumulator (CoSMAC) for real inputs from the antenna arrays.

The traversing of DFT coefficient vectors known as twiddle factors ($W_N^k = e^{-\frac{j2\pi k}{N}}$) in unit circle gives a clear picture about its symmetry and periodicity for the real inputs to the DFT [152], as shown in Figure 4-3 (a). This makes it to form a mirror image of the DFT samples across the horizontal axis as shown in Figure 4-3 (b). This is shown as an example here for $N = 8$, but holds for all $N = 2^r$, with r being an integer. In Figure 4-3 (b), only $5 = \frac{8}{2} + 1$ samples are required to specify the DFT sample spectrum. Hence in general, at most $\frac{N}{2} + 1$ complex values are required to specify the DFT samples of a length N sequence [153]. For the simplification purpose the input for DFT is considered as real inputs and The DFT samples may be generated by FFT or Filter-banks in the F-section. Consequently, the DFT samples $X_{0,1}[m]\ to\ X_{0,\frac{N}{2}-1}[m]$ in equation (4-7) and $X_{1,1}[m]\ to\ X_{1,\frac{N}{2}-1}[m]$ in equation (4-8) are always equal in reverse order to

respectively the complex conjugate of DFT samples $X_{0,N-1}[m]\ to\ X_{0,\frac{N}{2}+1}[m]$, $X_{1,N-1}[m]\ to\ X_{1,\frac{N}{2}+1}[m]$ and vice versa. By applying this property in equation (4-9), the input matrix transforms as follows,

$$\begin{aligned} Co_1 \\ = Diag\left\{\begin{bmatrix} X_{0,0}[0] & X_{0,0}[1] & \cdots & X_{0,0}[T-1] \\ X_{0,1}[0] & X_{0,1}[1] & \cdots & X_{0,1}[T-1] \\ \vdots & \vdots & \vdots & \vdots \\ X_{0,N-1}[0] & X_{0,N-1}[1] & \cdots & X_{0,N-1}[T-1] \end{bmatrix}\right. \\ \left.\times \begin{bmatrix} X_{1,0}[0] & X_{1,N-1}[0] & \cdots & X_{1,1}[0] \\ X_{1,0}[1] & X_{1,N-1}[1] & \cdots & X_{1,1}[1] \\ \vdots & \vdots & \vdots & \vdots \\ X_{1,0}[T-1] & X_{1,N-1}[T-1] & \cdots & X_{1,1}[T-1] \end{bmatrix}\right\} \end{aligned} \tag{4-11}$$

Then by simplifying the equation (4-11), the output matrix is obtained as shown below,

$$Co_1 = \begin{bmatrix} X_{0,0}[0] \times X_{1,0}[0] + X_{0,0}[1] \times X_{1,0}[1] \\ + \cdots + X_{0,0}[T-1] \times X_{1,0}[T-1] \\ X_{0,1}[0] \times X_{1,N-1}[0] + X_{0,1}[1] \times X_{1,N-1}[1] \\ + \cdots + X_{0,1}[T-1] \times X_{1,N-1}[T-1] \\ \vdots \\ X_{0,N-1}[0] \times X_{1,1}[0] + X_{0,N-1}[1] \times X_{1,1}[1] \\ + \cdots + X_{0,N-1}[T-1] \times X_{1,1}[T-1] \end{bmatrix} \tag{4-12}$$

Hence applying this mirror image symmetry eliminates the requirement of N conjugate operations per baseline and in total $(2Na^2 + Na)N$ conjugate operations for $(2Na^2 + Na)$ baselines. Now, let's consider the frequency samples $X_{0,1}[0]$ = Ry+jIy, $X_{1,1}[0]$ = Rz+jIz and their cross-correlation product $X_{0,1}[0] \times X_{1,N-1}[0]$ & $X_{0,N-1}[0] \times X_{1,1}[0]$ which is equivalent to $X_{0,1}[0] \times X_{1,1}[0]^*$ & $X_{0,1}[0]^* \times X_{1,1}[0]$ as shown in the equation below,

$$X_{0,1}[0] \times X_{1,1}[0]^* = X_{0,1}[0] \times X_{1,N-1}[0]$$
$$= (RyRz + IyIz) + j(RzIy - RyIz) \quad (4\text{-}13)$$

$$X_{0,1}[0]^* \times X_{1,1}[0] = X_{0,N-1}[0] \times X_{1,1}[0]$$
$$= (RyRz + IyIz) - j(RzIy - RyIz) \quad (4\text{-}14)$$

From equation (4-13) and (4-14), it is inferred that the coefficients in both cases remain the same and the outputs appear to be the conjugate of each other. Henceforth, only one Cross correlation is enough to be calculated and the other can be obtained by applying the property of conjugation.

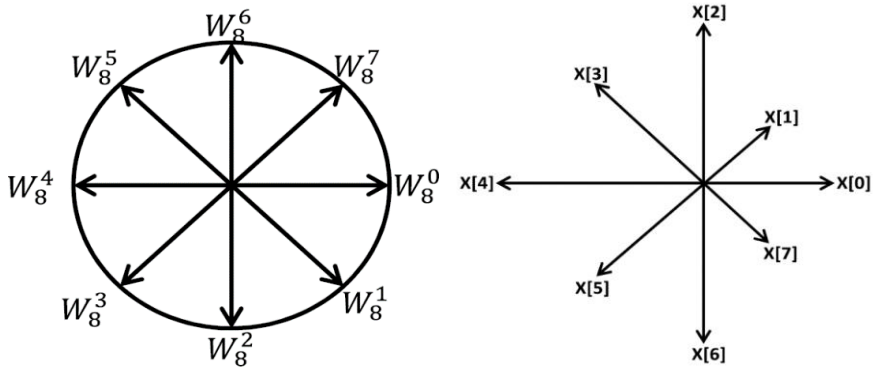

(a) (b)

Figure 4-3: (a) Symmetry and periodicity of DFT coefficient vectors (twiddle factors) traversing the unit circle for N = 8. (b) Mirror-image symmetry of DFT samples across the horizontal axis for N = 8. The displayed vector sample magnitudes are arbitrarily chosen variables.

Now, exploiting this property, the computation of equation (4-12) can be portioned into dual redundant column matrix parts, a $\left(\frac{N}{2}+1\right)$-tuple and a $\left(\frac{N}{2}-1\right)$-tuple. The first $\left(\frac{N}{2}+1\right)$ rows of the N-tuple in equation (4-12) can thus be extracted as the $\left(\frac{N}{2}+1\right)$-tuple (the 1st part) constituted by equation (4-16) with the algebraically corresponding input matrix product (of $\left(\frac{N}{2}+1\right)$ DFT samples of two

signals for T time slices) containing this part as the diagonal trace being given by equation (4-15) which can be derived by backtracking from equation (4-16).

$$Co_1 = \begin{bmatrix} X_{0,0}[0] & X_{0,0}[1] & \cdots & X_{0,0}[T-1] \\ X_{0,1}[0] & X_{0,1}[1] & \cdots & X_{0,1}[T-1] \\ \vdots & \vdots & \vdots & \vdots \\ X_{0,\frac{N}{2}-1}[0] & X_{0,\frac{N}{2}-1}[1] & \cdots & X_{0,\frac{N}{2}-1}[T-1] \\ X_{0,\frac{N}{2}}[0] & X_{0,\frac{N}{2}-1}[1] & \cdots & X_{0,\frac{N}{2}-1}[T-1] \end{bmatrix}$$
$$\begin{bmatrix} X_{1,0}[0] & X_{1,N-1}[0] & \cdots & X_{1,\frac{N}{2}+1}[0] & X_{1,\frac{N}{2}}[0] \\ X_{1,0}[1] & X_{1,N-1}[1] & \cdots & X_{1,\frac{N}{2}+1}[1] & X_{1,\frac{N}{2}}[1] \\ \vdots & \vdots & \vdots & \vdots & \vdots \\ X_{1,0}[T-1] & X_{1,N-1}[T-1] & \cdots & X_{1,\frac{N}{2}+1}[T-1] & X_{1,\frac{N}{2}}[T-1] \end{bmatrix} \quad (4\text{-}15)$$

$$Co_1 = \begin{bmatrix} X_{0,0}[0] \times X_{1,0}[0] + X_{0,0}[1] \times X_{1,0}[1] \\ + \cdots + X_{0,0}[T-1] \times X_{1,0}[T-1] \\ X_{0,1}[0] \times X_{1,N\_1}[0] + X_{0,1}[1] \times X_{1,N-1}[1] \\ + \cdots + X_{0,1}[T-1] \times X_{1,N-1}[T-1] \\ \vdots \\ X_{0,\frac{N}{2}-1}[0] \times X_{1,\frac{N}{2}+1}[0] + X_{0,\frac{N}{2}-1}[1] \times X_{1,\frac{N}{2}+1}[1] \\ + \cdots + X_{0,\frac{N}{2}-1}[T-1] \times X_{1,\frac{N}{2}+1}[T-1] \\ X_{0,\frac{N}{2}}[0] \times X_{1,\frac{N}{2}}[0] + X_{0,\frac{N}{2}}[1] \times X_{1,\frac{N}{2}}[1] \\ + \cdots + X_{0,\frac{N}{2}}[T-1] \times X_{1,\frac{N}{2}}[T-1] \end{bmatrix} \quad (4\text{-}16)$$

$$= \begin{bmatrix} X_{0,1}[0] \times X_{1,N\_1}[0] + X_{0,1}[1] \times X_{1,N-1}[1] \\ + \cdots + X_{0,1}[T-1] \times X_{1,N-1}[T-1] \\ \vdots \\ X_{0,\frac{N}{2}-1}[0] \times X_{1,\frac{N}{2}+1}[0] + X_{0,\frac{N}{2}-1}[1] \times X_{1,\frac{N}{2}+1}[1] \\ + \cdots + X_{0,\frac{N}{2}-1}[T-1] \times X_{1,\frac{N}{2}+1}[T-1] \end{bmatrix}^* \quad (4\text{-}17)$$

$$= \begin{bmatrix} X_{0,N-1}[0] \times X_{1,1}[0] + X_{0,N-1}[1] \times X_{1,1}[1] \\ + \cdots + X_{0,N-1}[T-1] \times X_{1,1}[T-1] \\ \vdots \\ X_{0,\frac{N}{2}+1}[0] \times X_{1,\frac{N}{2}-1}[0] + X_{0,\frac{N}{2}+1}[1] \times X_{1,\frac{N}{2}-1}[1] \\ + \cdots + X_{0,\frac{N}{2}+1}[T-1] \times X_{1,\frac{N}{2}-1}[T-1] \end{bmatrix} \quad (4\text{-}18)$$

The DFT samples $X_{0,0}[m], X_{1,0}[m], X_{0,\frac{N}{2}}[m]\ and\ X_{1,\frac{N}{2}}[m]$ and their cross correlation products form a unique constant set which are calculated independently. The lower $\left(\frac{N}{2}-1\right)$ rows of equation (4-12) (the second part) is obtained from the conjugate of the column matrix formed by the second to the second last row of the first part in equation (4-16), in mirror image order, whose equivalent forms are provided in equations (4-17) and (4-18).

$$\begin{aligned} & Ao_1 \\ & = Diag\left\{\begin{bmatrix} X_{0,0}[0] & X_{0,0}[1] & \cdots & X_{0,0}[T-1] \\ X_{0,1}[0] & X_{0,1}[1] & \cdots & X_{0,1}[T-1] \\ \vdots & \vdots & \vdots & \vdots \\ X_{0,N-1}[0] & X_{0,N-1}[1] & \cdots & X_{0,N-1}[T-1] \end{bmatrix}\right. \\ & \left.\times\begin{bmatrix} X_{0,0}[0]^* & X_{0,1}[0]^* & \cdots & X_{0,N-1}[0]^* \\ X_{0,0}[1]^* & X_{0,1}[1]^* & \cdots & X_{0,N-1}[1]^* \\ \vdots & \vdots & \vdots & \vdots \\ X_{0,0}[T-1]^* & X_{0,1}[T-1]^* & \cdots & X_{0,N-1}[T-1]^* \end{bmatrix}\right\} \end{aligned} \tag{4-19}$$

$$\begin{aligned} & = \begin{bmatrix} X_{0,0}[0] & X_{0,0}[1] & \cdots & X_{0,0}[T-1] \\ X_{0,1}[0] & X_{0,1}[1] & \cdots & X_{0,1}[T-1] \\ \vdots & \vdots & \vdots & \vdots \\ X_{0,\frac{N}{2}-1}[0] & X_{0,\frac{N}{2}-1}[1] & \cdots & X_{0,\frac{N}{2}-1}[T-1] \\ X_{0,\frac{N}{2}}[0] & X_{0,\frac{N}{2}-1}[1] & \cdots & X_{0,\frac{N}{2}-1}[T-1] \end{bmatrix} \\ & \times\begin{bmatrix} X_{0,0}[0] & X_{0,N-1}[0] & \cdots & X_{0,\frac{N}{2}+1}[0] & X_{0,\frac{N}{2}}[0] \\ X_{0,0}[1] & X_{0,N-1}[1] & \cdots & X_{0,\frac{N}{2}+1}[1] & X_{0,\frac{N}{2}}[1] \\ \vdots & \vdots & \vdots & \vdots & \vdots \\ X_{0,0}[T-1] & X_{0,N-1}[T-1] & \cdots & X_{0,\frac{N}{2}+1}[T-1] & X_{0,\frac{N}{2}}[T-1] \end{bmatrix} \end{aligned} \tag{4-20}$$

Thus, exploiting the complex conjugate symmetry of cross-correlation products, the required arithmetic operations is reduced to only $\left(\frac{N}{2}+1\right)$ to determine all the N visibilities per baseline. The $\left(\frac{N}{2}-1\right)$ conjugate frequency samples are not needed in accounting for their cross-correlation visibility contribution which is thus obtained at almost zero cost. In a similar fashion, the channel-wise auto-correlations (auto-correlation baselines) Ao_1 and Ao_2 for these two signals can also be obtained without conceding redundant arithmetic. The

generation of auto-correlation function Ao_1 is given in the equations from (4-19) to (4-22).

Like before, redundancy is exploited in the generation of Ao_1, since the auto-correlation of the frequency samples $X_{0,\frac{N}{2}+1}[m]$to $X_{0,N-1}[m]$ is always equal to the Auto correlation of the frequency samples from $X_{0,\frac{N}{2}-1}[m]$ to $X_{0,1}[m]$, as the samples are the complex conjugate of each other. The equation (4-21) shows the first part of Ao_1 with the corresponding input matrix product containing this part as the diagonal trace being given by the equation (4-20). The equation (4-22) shows the second part of Ao_1 generated by directly utilizing the second to the second last rows of equation (4-21) in a mirrored order as all the products' accumulations are real. In the same way the Ao_2 has been derived.

$$= \begin{bmatrix} X_{0,0}[0] \times X_{0,0}[0] + X_{0,0}[1] \times X_{0,0}[1] \\ + \cdots + X_{0,0}[T-1] \times X_{0,0}[T-1] \\ X_{0,1}[0] \times X_{0,N\_1}[0] + X_{0,1}[1] \times X_{0,N-1}[1] \\ + \cdots + X_{0,1}[T-1] \times X_{0,N-1}[T-1] \\ \vdots \\ X_{0,\frac{N}{2}-1}[0] \times X_{0,\frac{N}{2}+1}[0] + X_{0,\frac{N}{2}-1}[1] \times X_{0,\frac{N}{2}+1}[1] \\ + \cdots + X_{0,\frac{N}{2}-1}[T-1] \times X_{0,\frac{N}{2}+1}[T-1] \\ X_{0,\frac{N}{2}}[0] \times X_{0,\frac{N}{2}}[0] + X_{0,\frac{N}{2}}[1] \times X_{0,\frac{N}{2}}[1] \\ + \cdots + X_{0,\frac{N}{2}}[T-1] \times X_{0,\frac{N}{2}}[T-1] \end{bmatrix} \quad (4\text{-}21)$$

$$Ao_1 = \begin{bmatrix} X_{0,0}[0] \times X_{0,0}[0] + X_{0,0}[1] \times X_{0,0}[1] \\ + \cdots + X_{0,0}[T-1] \times X_{0,0}[T-1] \\ X_{0,1}[0] \times X_{0,N\_1}[0] + X_{0,1}[1] \times X_{0,N-1}[1] \\ + \cdots + X_{0,1}[T-1] \times X_{0,N-1}[T-1] \\ \vdots \\ X_{0,\frac{N}{2}-1}[0] \times X_{0,\frac{N}{2}+1}[0] + X_{0,\frac{N}{2}-1}[1] \times X_{0,\frac{N}{2}+1}[1] \\ + \cdots + X_{0,\frac{N}{2}-1}[T-1] \times X_{0,\frac{N}{2}+1}[T-1] \\ X_{0,\frac{N}{2}}[0] \times X_{0,\frac{N}{2}}[0] + X_{0,\frac{N}{2}}[1] \times X_{0,\frac{N}{2}}[1] \\ + \cdots + X_{0,\frac{N}{2}}[T-1] \times X_{0,\frac{N}{2}}[T-1] \end{bmatrix} \quad (4\text{-}22)$$

The auto-correlation of a complex sample (in any of the equivalent forms using complex conjugate symmetry) involves only two real multipliers and the output has no imaginary part, which is also equal to the auto-correlation of its conjugate sample as shown in the equations below,

$$\begin{aligned} X_{0,1}[0] \times X_{0,1}[0]^* &= X_{0,1}[0] \times X_{0,N-1}[0] \\ &= X_{0,N-1}[0] \times X_{0,N-1}[0]^* \\ &= X_{0,N-1}[0] \times X_{0,1}[0] \\ &= (RyRy + IyIy) \end{aligned} \tag{4-23}$$

$$\begin{aligned} X_{1,1}[0] \times X_{1,1}[0]^* &= X_{1,1}[0] \times X_{1,N-1}[0] \\ &= X_{0,N-1}[0] \times X_{0,N-1}[0]^* \\ &= X_{0,N-1}[0] \times X_{0,1}[0] \\ &= (RzRz + IzIz) \end{aligned} \tag{4-24}$$

Hence, based on equations (4-13) and (4-14) the requirement of $2N$ input registers for calculating one baseline is reduced to just $N + 2$ registers Also, the presented computational minimization algorithm results in nearly 50% reduction of the arithmetic and storage memory requirement in calculating a single baseline, since the N arithmetic operations are reduced to just $\left(\frac{N}{2} + 1\right)$.

Based on the above equations, a new dedicated correlator system multiplier and accumulator is designed as shown in Figure 4-4 and named as CoSMAC. This new CoSMAC provides the product components for two mirror-image symmetric (complex conjugate) cross-correlations in a single clock cycle. Unlike the generic CMAC, the CoSMAC does the conjugation in a single final step (single sign conversion) after the product accumulation for the dump time T (T time slices), thus saving power. Also, a single CoSMAC can be used to calculate four Auto correlation functions as the auto correlation has no imaginary part. To summarise,

one CoSMAC is used to calculate two Cross correlations or four Auto correlations visibilities for a baseline.

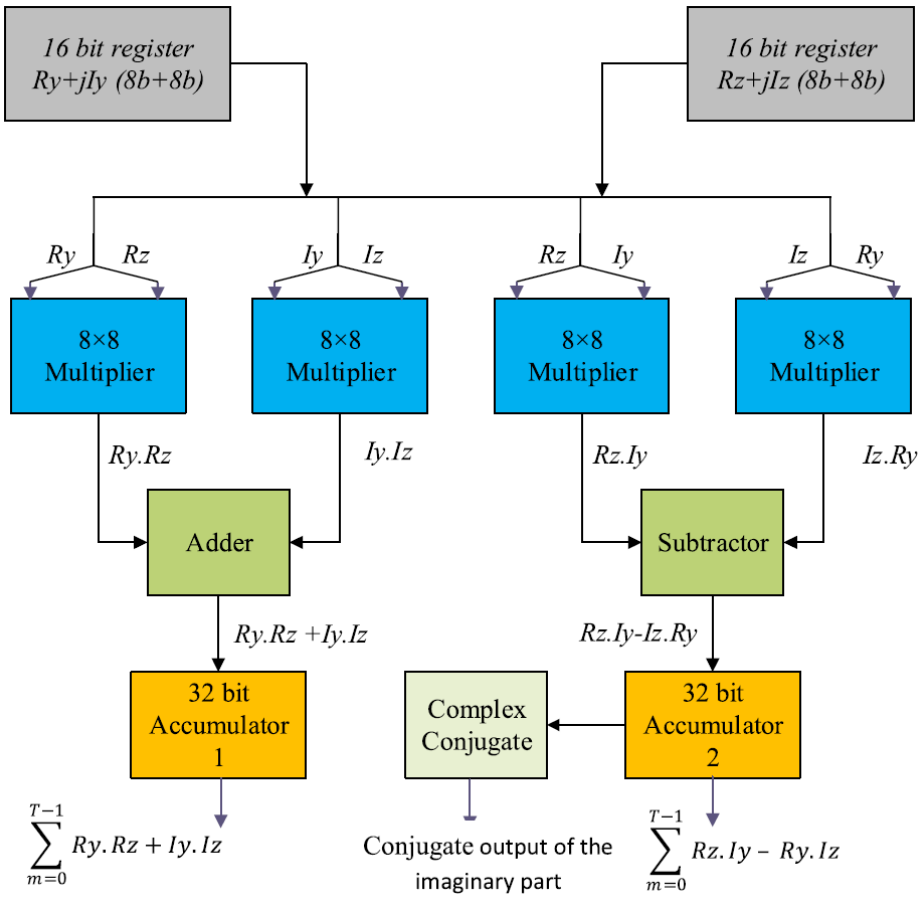

Figure 4-4: Block diagram of proposed dedicated Correlator-System_Multiplier-and-Accumulator (CoSMAC) cell for X-section of FX-Correlator.

4.3.2 Design of Processing Element (PE) based on the CoSMAC

The CoSMAC design is further modified with some additional components, a multiplexer in the input and a demultiplexer in the output as shown in Figure 4-5. The Processing Element design performs both Cross correlation and Auto correlation of two complex samples in one clock period. The selection of each of the two operations is controlled by a select line, SEL. The 2x1 multiplexers act as an input control unit while the 1x2 demultiplexers serve as output control unit for CoSMAC based on the control signal SEL. SEL is an internally wired level triggering mux-control signal derived from the 50% duty cycle of the global clock. It toggles twice within every clock period for every new frequency sample pair of

two distinct signals. The Subtractor block in CoSMAC is replaced with an Adder/Subtractor to perform both Auto and Cross correlations. Two additional dedicated accumulators are added for storing the final Auto and Cross correlation outputs separately.

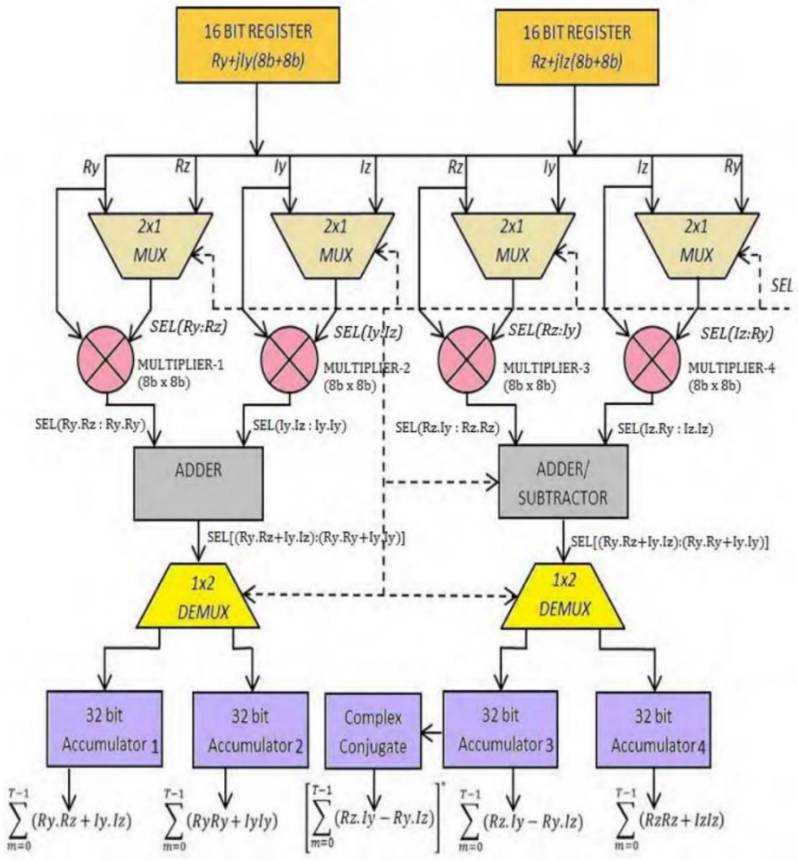

Figure 4-5: Block diagram of proposed Processing Element (PE) cell for X-section of FX-Correlator.

The two 16-bit registers are loaded with new inputs $Ry + jIy$ and $Rz + jIz$, at every clock interval, which are each 8b+8b complex numbers in two's complement form. When SEL is 'HIGH', the Multiplexers in the input section selects the operands for cross-correlation and the PE will produce the real and imaginary magnitude parts as shown in equations (4-15) or (4-16) (similar to equations (4-13) and (4-14)) along with the sign conversion of the imaginary part for the complex conjugate cross-correlation product (for the conjugate channel) in equation (4-16). At the same time, the Demultiplexers select the dedicated Accumulators for Cross Correlation and integrate the products over the time period T. Similarly, if SEL is 'LOW', Multiplexers choose the Auto Correlation

coordinates and the Demultiplexers select the dedicated Accumulators for Auto Correlation to integrate the Auto correlation outputs (4-23) and (4-24). After the integration over the time period T, the data from the accumulators are read out for the next process. Table 4-1 summarizes the visibilities obtained from a single Processing Element after the integration time period T.

Output Data	Baseline	Coordinate	Correlation
$\sum_{m=0}^{T-1}(Ry.Rz + Iy.Iz)$	Baseline 1 (Accumulator 1)	Real (Common for two Visibilities)	Cross
$\sum_{m=0}^{T-1}(Rz.Iy - Ry.Iz)$	Baseline 1 (Accumulator 3)	Imaginary (First Visibility)	Cross
$\left[\sum_{m=0}^{T-1}(Rz.Iy - Ry.Iz)\right]^{*}$	Baseline 1 (Conjugation output using Accumulator 3)	Imaginary (Second Visibility)	Cross
$\sum_{m=0}^{T-1}(RyRy + IyIy)$	Baseline 2 (Accumulator 2)	Real (First and Fourth Visibilities)	Auto
$\sum_{m=0}^{T-1}(RzRz + IzIz)$	Baseline 3 (Accumulator 4)	Real(First and Sixth Visibilities	Auto

Table 4- 1: Visibilities calculated by one processing element (PE)

The Accumulator 1 and Accumulator 3 produce the Cross correlation visibilities for the first baseline, where the former gives out the real coordinate value which is common to both the visibilities and the latter produces the imaginary coordinate value of the first visibility which is then fed to the conjugation unit to calculate the imaginary coordinate value for the second visibility after the integration time period T. Similarly, Accumulator 2 and Accumulator 4 produce the first and second Auto correlation visibilities and are identical to the third and fourth visibilities since the Autocorrelation of their conjugates remain the same. By using the conventional method for the above operation, four CMACs (based on one CMAC for a Cross correlation and one CMAC for two Auto correlations) are

required to calculate all the six visibilities. In other words, this process involves the use of sixteen multipliers, four adders, four subtractors and eight accumulators. Whereas the proposed processing element uses only four multipliers, two adder blocks and four accumulators for the operation. The multiplexers and demultiplexers are additional hardware elements used in the design but cost low when compared to the multipliers and adder blocks used in the conventional method. Overall, all the six visibilities are obtained through one Processing element which hence proves to be efficient in terms of area and power utilization.

4.3.3 Design of (PE_IQ) Processing Element for IQ sampled signals (complex inputs) from the antenna arrays

The designs CoSMAC and PE are utilised in the X-Section to calculate the correlation efficiently for the real inputs from the antennas, but in some interferometer techniques, they use antennas that produce complex inputs (IQ sampled inputs) [160]. In this case, the same mirror image symmetry property can be used but with slight changes in the input side of the Processing Element. For this, consider the two frequency sampled signals $X_{0,k}[m]$ and $X_{1,k}[m]$ on equations (4-7) & (4-8) used in the calculation of cross correlation of two signals in equation (4-6). These are the complex samples obtained after performing DFT, either by using real or complex inputs. Here in this section, the inputs for the DFT are considered as complex sampled (IQ sampled) signals (In section 4.3.1 the inputs for the DFT are considered as real). Let's consider the DFT outputs $X_{0,k}[m]$ and $X_{1,k}[m]$ are obtained from the complex inputs $x_{0,n}[m]$ and $x_{1,n}[m]$ given in equation (4-25) and (4-26), where n varies from 0 to N-1 and m is the time slice index value for the accumulation dump period T. Here, the $x_{0,0}[m]$ to $x_{0,N-1}[m]$ in $x_{0,\mathrm{n}}[m]$ and $x_{1,0}[m]$ to $x_{1,N-1}[m]$ in $x_{1,\mathrm{n}}[m]$ are complex samples (IQ samples, where I is the real coordinates and Q is the imaginary coordinates).

$$x_{0,\mathrm{n}}[m] = \begin{Bmatrix} x_{0,0}[m], x_{0,1}[m], \cdots, x_{0,\frac{N}{2}-1}[m] \\ , x_{0,\frac{N}{2}}[m], x_{0,\frac{N}{2}+1}[m], \cdots, x_{0,N-1}[m] \end{Bmatrix} \qquad (4\text{-}25)$$

And,

$$x_{1,\mathrm{n}}[m] = \begin{Bmatrix} x_{1,0}[m], x_{1,1}[m], \cdots, x_{1,\frac{N}{2}-1}[m] \\ , x_{1,\frac{N}{2}}[m], x_{1,\frac{N}{2}+1}[m], \cdots, x_{1,N-1}[m] \end{Bmatrix} \quad (4\text{-}26)$$

The complex sampled signal $x_{0,\mathrm{n}}[m]$ and $x_{1,\mathrm{n}}[m]$ can be written as

$$x_{0,\mathrm{n}}[m] = xr_{0,\mathrm{n}}[m] + j\, xi_{0,\mathrm{n}}[m] \quad (4\text{-}27)$$

$$x_{1,\mathrm{n}}[m] = xr_{1,\mathrm{n}}[m] + j\, xi_{1,\mathrm{n}}[m] \quad (4\text{-}28)$$

Where, $xr_{0,\mathrm{n}}[m]$ and $xr_{1,\mathrm{n}}[m]$ are the real coefficients, $xi_{0,\mathrm{n}}[m]$ and $xi_{1,\mathrm{n}}[m]$ are the imaginary coefficients of the complex samples $x_{0,\mathrm{n}}[m]$ and $x_{1,\mathrm{n}}[m]$ respectively. Applying DFT to the equation (4-27) and (4-28), we get equations as follows,

$$X_{0,\mathrm{k}}[m] = \sum_{n=0}^{N-1} xr_{0,\mathrm{n}}[m] e^{\frac{-j2\pi nk}{N}} + \sum_{n=0}^{N-1} jxi_{0,\mathrm{n}}[m] e^{\frac{-j2\pi nk}{N}}$$

$$X_{0,\mathrm{k}}[m] = Xr_{0,\mathrm{k}}[m] + j\, Xi_{0,\mathrm{k}}[m] \quad (4\text{-}27)$$

$$Similarly, \quad X_{1,\mathrm{k}}[m] = Xr_{1,\mathrm{k}}[m] + j\, Xi_{1,\mathrm{k}}[m] \quad (4\text{-}28)$$

Where, $Xr_{0,\mathrm{k}}[m]$, $Xr_{1,\mathrm{k}}[m]$ are the real coefficients and $Xi_{0,\mathrm{k}}[m], Xi_{1,\mathrm{k}}[m]$ are the imaginary coefficients of the frequency sampled signal $X_{0,\mathrm{k}}[m]$ *and* $X_{1,\mathrm{k}}[m]$ respectively. The frequency samples $Xr_{0,\mathrm{k}}[m]$ & $Xr_{1,\mathrm{k}}[m]$ are given by

$$Xr_{0,\mathrm{k}}[m] = \left\{ \begin{matrix} Xr_{0,0}[m], Xr_{0,1}[m], \cdots, Xr_{0,\frac{N}{2}-1}[m] \\ , Xr_{0,\frac{N}{2}}[m], Xr_{0,\frac{N}{2}+1}[m], \cdots, Xr_{0,N-1}[m] \end{matrix} \right\} \quad (4\text{-}29)$$

$$Xi_{0,\mathrm{k}}[m] = \left\{ \begin{matrix} Xi_{0,0}[m], Xi_{0,1}[m], \cdots, Xi_{0,\frac{N}{2}-1}[m] \\ , Xi_{0,\frac{N}{2}}[m], Xi_{0,\frac{N}{2}+1}[m], \cdots, Xi_{0,N-1}[m] \end{matrix} \right\} \quad (4\text{-}30)$$

In equations (4-29) & (4-30), the $Xr_{0,\mathrm{k}}[m]$ and $Xi_{0,\mathrm{k}}[m]$ will have the mirror image symmetry property as shown in Figure 4-3 which is described as an example for an 8 point DFT (N=8). That is, the DFT samples $Xr_{0,1}[m]$ to $Xr_{0,\frac{N}{2}-1}[m]$ in equation (4-29) and DFT samples $Xi_{0,1}[m]$ to $Xi_{0,\frac{N}{2}-1}[m]$ in equation (4-30) are equal in reverse order to the complex conjugate of the DFT samples $Xr_{0,\frac{N}{2}+1}[m]$ to $Xr_{0,N-1}[m]$ and $Xi_{0,\frac{N}{2}+1}[m]$ *to* $Xi_{0,N-1}[m]$ respectively. But this symmetric property of $Xi_{0,\mathrm{k}}[m]$ changes when it is multiplied with the factor j as given in equation (4-27) or simply say it is phase shifted to 90° as shown in Figure 4-6.

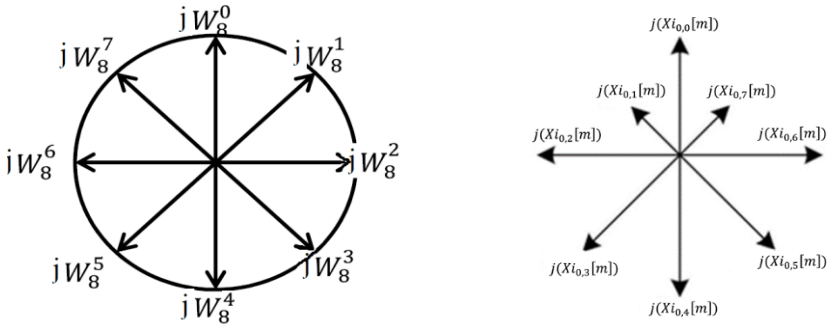

(a) *(b)*

Figure 4-6: (a) Symmetry and periodicity of DFT coefficient vectors (twiddle factors) traversing the unit circle for N = 8 but phase shifted to 90° . (b) Mirror-image symmetry of DFT samples across the horizontal axis for N = 8 but phase shifted to 90°.

It's also been known that the DFT samples in equation (4-29) and (4-30) are also complex values, i.e., the $Xr_{0,\mathrm{k}}[m] = Xr_{0,\mathrm{k}}[m]_{real} + j\,Xr_{0,\mathrm{k}}[m]_{img}$ and $Xi_{0,\mathrm{k}}[m] = Xi_{0,\mathrm{k}}[m]_{real} + j\,Xi_{0,\mathrm{k}}[m]_{img}$. Therefore, by using these values and

applying the mirror image symmetry property on equation (4-29) and (4-30), which can be rewritten as,

$$Xr_{0,\mathrm{k}}[m] = \begin{Bmatrix} Xr_{0,0}[m], Xr_{0,1}[m]_{real} + j\, Xr_{0,1}[m]_{img}, \cdots \\ Xr_{0,\frac{N}{2}-1}[m]_{real} + Xr_{0,\frac{N}{2}-1}[m]_{img}, Xr_{0,\frac{N}{2}}[m] \\ Xr_{0,\frac{N}{2}-1}[m]_{real} - jXr_{0,\frac{N}{2}-1}[m]_{img}, \cdots \\ , Xr_{0,1}[m]_{real} - j\, Xr_{0,1}[m]_{img} \end{Bmatrix} \quad (4\text{-}31)$$

$$Xi_{0,\mathrm{k}}[m] = \begin{Bmatrix} Xi_{0,0}[m], Xi_{0,1}[m]_{real} + j\, Xi_{0,1}[m]_{img}, \cdots \\ Xi_{0,\frac{N}{2}-1}[m]_{real} + Xi_{0,\frac{N}{2}-1}[m]_{img}, Xi_{0,\frac{N}{2}}[m] \\ Xi_{0,\frac{N}{2}-1}[m]_{real} - Xi_{0,\frac{N}{2}-1}[m]_{img}, \cdots \\ , Xi_{0,1}[m]_{real} - j\, Xi_{0,1}[m]_{img} \end{Bmatrix} \quad (4\text{-}32)$$

Where, the samples $Xr_{0,0}[m]$ and $Xr_{0,\frac{N}{2}}[m]$ are real and independent. Now, multiplying the j factor with equation (4-32) and is given by,

$$\begin{aligned} & j \times Xi_{0,\mathrm{k}}[m] \\ & = \begin{Bmatrix} jXi_{0,0}[m], -Xi_{0,1}[m]_{img} + j\, Xi_{0,1}[m]_{real}, \cdots \\ -Xi_{0,\frac{N}{2}-1}[m]_{img} + jXi_{0,\frac{N}{2}-1}[m]_{real}, \mathrm{j}Xi_{0,\frac{N}{2}}[m], \\ Xi_{0,\frac{N}{2}-1}[m]_{img} + jXi_{0,\frac{N}{2}-1}[m]_{real}, \dots, \\ Xi_{0,1}[m]_{img} + j\, Xi_{0,1}[m]_{real} \end{Bmatrix} \end{aligned} \quad (4\text{-}33)$$

For instance, consider calculating the $X_{0,1}[m]$ and $X_{0,\mathrm{N}-1}[m]$ in equation (4-27) using equation (4-31) and (4-33),

$$\begin{aligned} X_{0,1}[m] &= Xr_{0,1}[m] + j\, Xi_{0,1}[m] \\ X_{0,1}[m] &= \left(Xr_{0,1}[m]_{real} + jXr_{0,1}[m]_{img}\right) \\ &\quad + \left(-Xi_{0,1}[m]_{img} + jXi_{0,1}[m]_{real}\right) \end{aligned} \quad (4\text{-}34)$$

$$X_{0,1}[m] = (Xr_{0,1}[m]_{real} - Xi_{0,1}[m]_{img}) + \mathrm{j}(Xr_{0,1}[m]_{img} + Xi_{0,1}[m]_{real})$$

$$X_{0,\mathrm{N}-1}[m] = Xr_{0,\mathrm{N}-1}[m] + j\,Xi_{0,\mathrm{N}-1}[m]$$

$$X_{0,\mathrm{N}-1}[m] = \left(Xr_{0,1}[m]_{real} - j\,Xr_{0,1}[m]_{img}\right) + \left(Xi_{0,1}[m]_{img} + j\,Xi_{0,1}[m]_{real}\right)$$

$$X_{0,\mathrm{N}-1}[m] = (Xr_{0,1}[m]_{real} + Xi_{0,1}[m]_{img}) + j(Xi_{0,1}[m]_{real} - Xr_{0,1}[m]_{img}) \quad (4\text{-}35)$$

Similarly, the $X_{1,1}[m]$ and $X_{1,\mathrm{N}-1}[m]$ frequency samples are calculated, and it's given by,

$$X_{1,1}[m] = (Xr_{1,1}[m]_{real} - Xi_{1,1}[m]_{img}) + \mathrm{j}(Xr_{1,1}[m]_{img} + Xi_{1,1}[m]_{real}) \quad (4\text{-}36)$$

$$X_{1,\mathrm{N}-1}[m] = (Xr_{1,1}[m]_{real} + Xi_{1,1}[m]_{img}) + j(Xi_{1,1}[m]_{real} - Xr_{1,1}[m]_{img}) \quad (4\text{-}37)$$

On comparing the equations (4-34) and (4-35), it's been clear that the calculation of samples $X_{0,1}[m]$ and $X_{0,\mathrm{N}-1}[m]$ requires the same coefficients but different adder/subtractor operation for calculating real and imaginary values. Hence, it's clear that the property of mirror image symmetry can also be used to reduce the number of $x_{i,n}[m]$ samples (IQ samples) from $(N)i$ to $(\frac{N}{2}+1)i$ samples to calculate all the $(N)i$ number of $X_{i,\mathrm{k}}[m]$ frequency samples, where i is the index number of the signals , n is the index number of time domain samples in a signal ranges from *0* to *N-1* , k is the index number of frequency domain samples in a signal ranges from *0* to *N-1* and *N* is the number of samples per signal. Now, let's consider the cross-correlation equation (4-10) for calculating the two signals

$X_{0,\mathrm{k}}[m]$ and $X_{1,\mathrm{k}}[m]$. Based on the above equations from (4-25) to (4-37), the equation (4-10) can be written as,

$$Co_1 = \begin{bmatrix} Xr_{0,0}[0] \times Xr_{1,0}[0]^* + Xr_{0,0}[1] \times Xr_{1,0}[1]^* \\ + \cdots + Xr_{0,0}[T-1] \times Xr_{1,0}[T-1]^* \\ Xr_{0,1}[0] + j\,Xi_{0,1}[0] \times (Xr_{1,1}[0] + j\,Xi_{1,1}[0])^* + \cdots \\ +Xr_{0,1}[T-1] + j\,Xi_{0,1}[T-1] \times (Xr_{1,1}[T-1] + j\,Xi_{1,1}[T-1])^* \\ \vdots \\ Xr_{0,\mathrm{N}-1}[0] + j\,Xi_{0,\mathrm{N}-1}[0] \times (Xr_{1,\mathrm{N}-1}[0] + j\,Xi_{1,\mathrm{N}-1}[0])^* + \cdots \\ +Xr_{0,\mathrm{N}-1}[T-1] + j\,Xi_{0,\mathrm{N}-1}[T-1] \times (Xr_{1,\mathrm{N}-1}[T-1] + j\,Xi_{1,\mathrm{N}-1}[T-1])^* \end{bmatrix} \quad 4\text{-}38$$

For the hardware design of the new correlator cell PE_IQ, consider the visibility calculation in the second and last rows from the equation (4-38), i.e. given by,

$$\sum_{m=0}^{T-1} \left(Xr_{0,1}[m] + j\,Xi_{0,1}[m]\right) \times \left(Xr_{1,1}[m] + j\,Xi_{1,1}[m]\right)^* \right) \quad (4\text{-}39)$$

And,

$$\sum_{m=0}^{T-1} \left(Xr_{0,\mathrm{N}-1}[m] + j\,Xi_{0,\mathrm{N}-1}[m]\right) \times \left(Xr_{1,\mathrm{N}-1}[m] + j\,Xi_{1,\mathrm{N}-1}[m]\right)^* \right) \quad (4\text{-}40)$$

Substitute equations (4-34) to (4-36) in equation (4-39) and (4-40), which is given by,

$$\sum_{m=0}^{T-1} \begin{pmatrix} [(Xr_{0,1}[m]_{real} - Xi_{0,1}[m]_{img}) + j(Xr_{0,1}[m]_{img} + Xi_{0,1}[m]_{real})] \times \\ [(Xr_{1,1}[m]_{real} - Xi_{1,1}[m]_{img}) + j(Xr_{1,1}[m]_{img} + Xi_{1,1}[m]_{real})]^* \end{pmatrix} \quad (4\text{-}41)$$

$$\sum_{m=0}^{T-1} \begin{pmatrix} [(Xr_{0,1}[m]_{real} + Xi_{0,1}[m]_{img}) + j(Xi_{0,1}[m]_{real} - Xr_{0,1}[m]_{img})] \times \\ [(Xr_{1,1}[m]_{real} + Xi_{1,1}[m]_{img}) + j(Xi_{1,1}[m]_{real} - Xr_{1,1}[m]_{img})]^* \end{pmatrix} \quad (4\text{-}42)$$

Comparing the equations (4-41) and (4-42), it's been clear that, both the processes use the same coefficients, and each requires one adder and one subtractor to calculate the inputs before correlation. On further solving the visibility equations (4-39) and (4-40) lead to estimate their particular real and imaginary values, which is given by,

$$\sum_{m=0}^{T-1} [(Xr_{0,1}[m] \times (Xr_{1,1}[m]) + (Xi_{0,1}[m] \times Xi_{1,1}[m])] + j[(Xr_{1,1}[m] \times Xi_{0,1}[m]) - (Xr_{0,1}[m] \times Xi_{1,1}[m])] \quad (4\text{-}43)$$

And,

$$\sum_{m=0}^{T-1} [(Xr_{0,\mathrm{N}-1}[m] \times (Xr_{1,\mathrm{N}-1}[m]) + (Xi_{0,\mathrm{N}-1}[m] \times Xi_{1,\mathrm{N}-1}[m])] + j[(Xr_{1,\mathrm{N}-1}[m] \times Xi_{0,\mathrm{N}-1}[m]) - (Xr_{0,\mathrm{N}-1}[m] \times Xi_{1,\mathrm{N}-1}[m])] \quad (4\text{-}44)$$

The equations (4-43) and (4-44) prove that it requires one adder, one subtractor, four multipliers and four accumulators as same as PE (section 4.3.3) to calculate the cross correlation.

The Figure 4-7 shows the block diagram of the proposed PE_IQ correlator cell to calculate the cross correlation in the X-section of FX correlator for IQ sampled input signals from the antennas. The hardware structure uses the same PE architecture (Figure 4-5) but a slight modification in the input section to accommodate the mirror image symmetric property for the IQ sampled signals. The 8-bit registers of the PE_IQ correlator cell swaps the input coefficients between the registers based on the SEL signal and feed the corresponding subtractors and adders to calculate the inputs as shown in the Figure 4-7. When SEL signal is 'HIGH', the PE_IQ will produce the real and imaginary magnitude parts as shown in equation (4-43) using the values loaded in the 8-bit input registers during the positive edge of the global clock. At the same time the demultiplexers select the 32-bit Accumulator 1 and Accumulator 3 and integrate the products over the time period of T. Similarly, if SEL is 'LOW', the 8-bit input registers swap the same set of

values between them for PE_IQ to produce the output as shown in equation (4-44) and the demultiplexers select the Accumulator 2 and Accumulator 4 at the same time to integrate the output over time period T. Thus, in the same clock cycle with same set of inputs, a single PE_IQ correlator cell is capable to calculate two cross correlation visibilities per baseline.

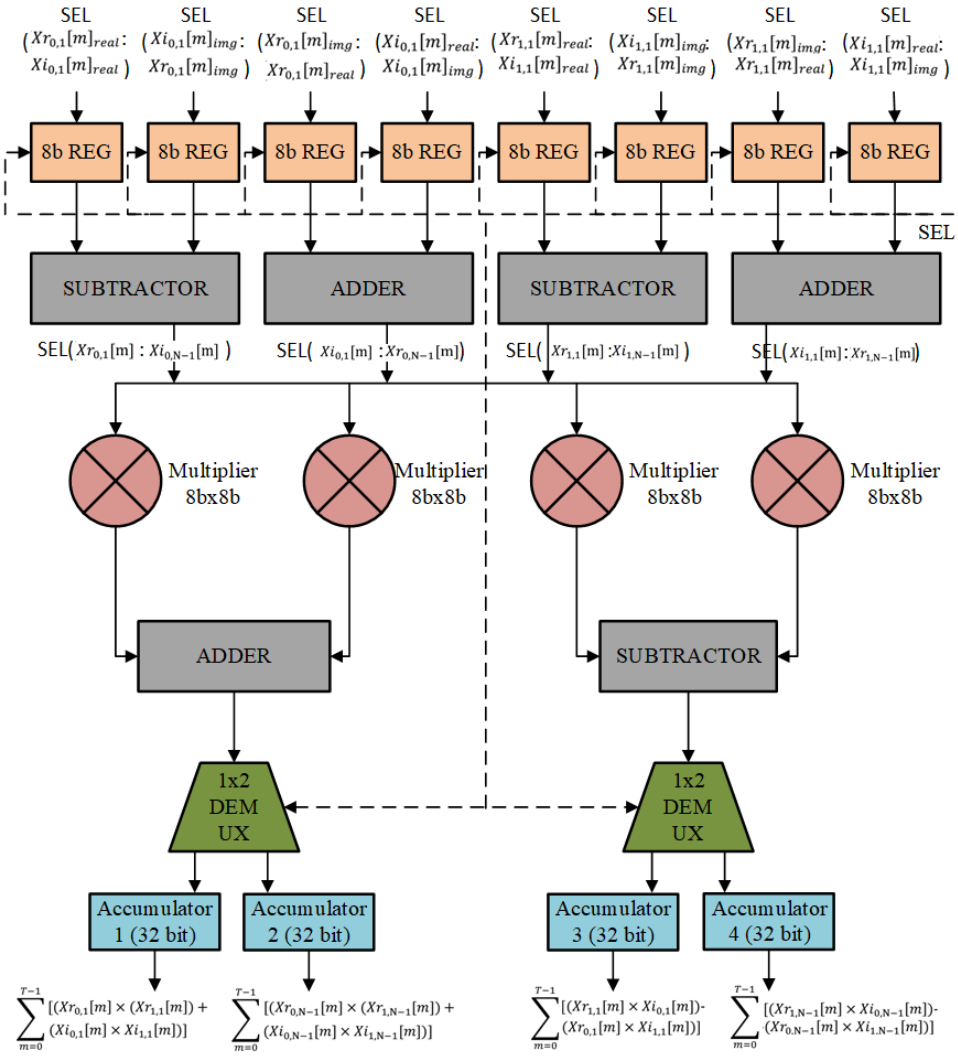

Figure 4-7: Block diagram of proposed PE_IQ cell for X-section of the FX-Correlator.

The dataflow within the CoSMAC (Figure 4-4), PE (Figure 4-5) and PE_IQ (Figure 4-7) cells are also quite simple and regular when compared with the existing CMAC (Figure 4-2) cell. Hence, these proposed new cells for minimized baseline calculations do not impose any extra dataflow management overhead compared to the existing state-of-the-art.

4.4 Design of power efficient ASIC Multiplier

The correlators are the most power consuming units in large interferometers since the correlator size increases if the number of antennas and the total bandwidth from these antennas increases as discussed in Chapter 3. Both the three proposed correlator cells and the CMAC architectures employ the same type of multipliers and the power reduction in proposed correlator cells are primarily due to the architectural change. It is possible to further reduce the power consumption of these proposed correlator cells by choosing a core power-efficient multiplier, since, it is the most power consuming block in any correlator implementation. In this design, different algorithms analysed in Chapter 3 are combined to form a power-efficient and fast multiplier-accumulator for use in the PE, PE_IQ, CoSMAC or in the conventional CMAC architectures. Fast multiplier algorithms such as Dadda-tree, Wallace tree, Modified-Booth-algorithm with various fast-adders, are compared and used to design the proposed new multiplier structure for FX correlator. It has been assumed that the input signals are 8-bit two's complement numbers.

4.4.1 Fast multiplier algorithms

The gate-counts required for the design of Normal-Wallace tree, Modified-Wallace-tree and Dadda-tree structures in the reduction phase are tabulated in Table 4-2 excluding the gate-count required for the partial-product generation and the final two row addition. From the Table 4-2, it is evident that the Dadda-tree structure requires less gate-count than the other two methods. The number of adders utilised in the reduction phase depends entirely on the number of partial products generated initially using AND-gate (2-Input) or Booth-algorithm [141] or Modified-Booth-algorithm [142]. The Modified-Booth-algorithm reduces the number of partial products generated for the multiplication by half (Chapter 3) and hence decreases the hardware used to add the partial products.

Reduction Algorithm	FA	HA	Total Gates
Normal- Wallace-tree	38	15	402
Modified- Wallace-tree	39	3	363
Dadda-tree	35	7	343

Table 4- 2: Gate required for different reduction tree Algorithms

Hence the proposed multiplier design utilises Modified Booth algorithm for partial products' reduction and Modified-Wallace-tree and Dadda-tree architectures for the reduction process. In order to attain the final product, usually some fast adders are used to accumulate the final two rows obtained from the reduction-tree. It is always important to take care that the inputs for this adder are not available at the same time when designing these adders. In this regard, the technique proposed in [154] requires considerable number of logic-gates to generate the final output which was resolved in [155], but is applicable only to the most significant bit part of the accumulation. The design of a novel and efficient multiplier for interferometry considers the design aspects proposed in [155] and [156] in-conjunction with the above described partial-product reduction-algorithm. The most efficient multiplier designed after a careful examination of the possible combinations is planned to incorporate into the CMAC, CoSMAC, PE_IQ and PE cells.

4.4.2 Reduction tree structure with Modified-Booth-algorithm

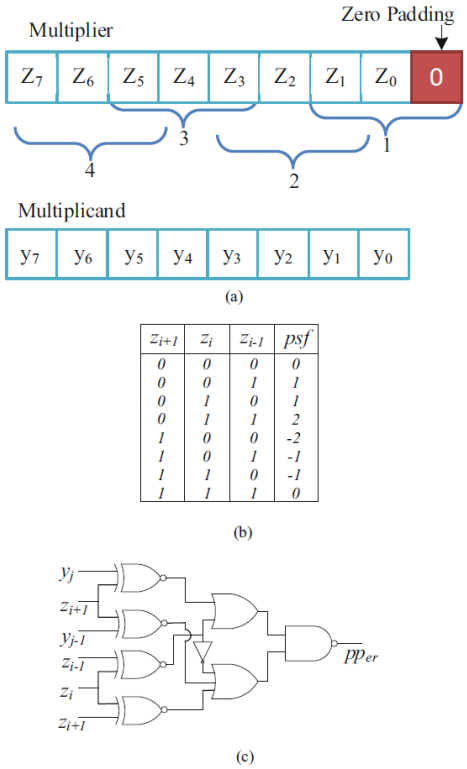

z_{i+1}	z_i	z_{i-1}	*psf*
0	0	0	0
0	0	1	1
0	1	0	1
0	1	1	2
1	0	0	-2
1	0	1	-1
1	1	0	-1
1	1	1	0

Figure 4-8: Modified Booth Multiplier (a) Zero padding and dividing the multiplier value, (b) Partial-product scaling factor (psf), (c) Partial-product generator.

As an illustration, let us consider two 8-bit values y_j (multiplicand) and Z_i(multiplier), where i and j represent the bit-position ranging from 0 to 7. The Multiplier value Z is padded with one Zero in the LSB and divided into overlapping sets of 3-bits each by the Modified-Booth-algorithm as shown in Figure 4-8. The partial-product scale factor (*psf*) $(0, +y, +2y, -y \; and \; -2y)$ is determined for each set. Here, $+y$ represents placement of the multiplicand bits as they are, $-y$ denotes the two's complement of the multiplicand bits, $+2y$ signifies doubling of the multiplicand bits and $-2y$ denotes the two's complement of the doubled multiplicand bits. The partial-products (PP_{er}) are generated using the partial-product generator as shown in Figure 4-8 (c), where e represents the position and r denotes the row-number. The partial-product rows thus obtained, are arranged based on the simplified sign-extension method [145] as shown in Figure 4-9.

$$
\begin{array}{cccccccccccccccc}
 & & & & & & & & y_7 & y_6 & y_5 & y_4 & y_3 & y_2 & y_1 & y_0 \\
 & & & & & & & & Z_7 & Z_6 & Z_5 & Z_4 & Z_3 & Z_2 & Z_1 & Z_0 \\
\hline
 & & & & & & & \overline{pp_{80}} & pp_{80} & pp_{80} & pp_{80} & pp_{70} & pp_{60} & pp_{50} & pp_{40} & pp_{30} & pp_{20} & pp_{10} & pp_{00} \\
 & & & & & & 1 & \overline{pp_{81}} & pp_{81} & pp_{71} & pp_{61} & pp_{51} & pp_{41} & pp_{31} & pp_{21} & pp_{11} & pp_{01} & & \\
 & & & & & 1 & \overline{pp_{82}} & pp_{82} & pp_{72} & pp_{62} & pp_{52} & pp_{42} & pp_{32} & pp_{22} & pp_{12} & pp_{02} & & & \\
 & & & & 1 & \overline{pp_{83}} & pp_{83} & pp_{73} & pp_{63} & pp_{53} & pp_{43} & pp_{33} & pp_{23} & pp_{13} & pp_{03} & & & & \\
\end{array}
$$

Figure 4-9: Partial-product rows formed using Modified-Booth-algorithm and the simplified sign-extension method.

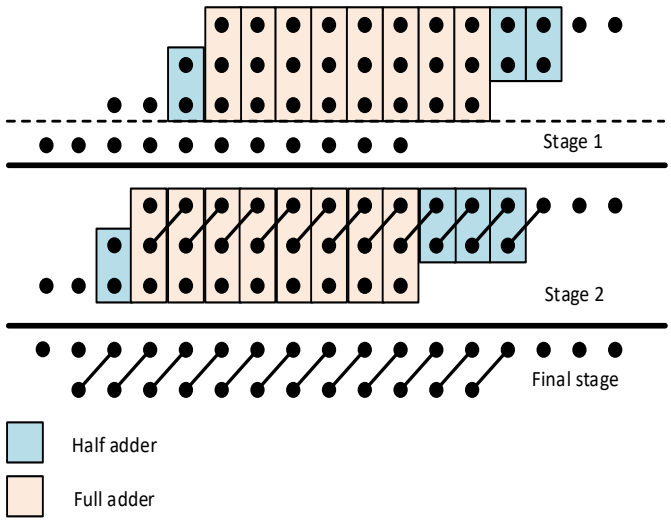

Figure 4-10: Wallace-tree reduction for the Partial-product rows generated using Modified-Booth-algorithm.

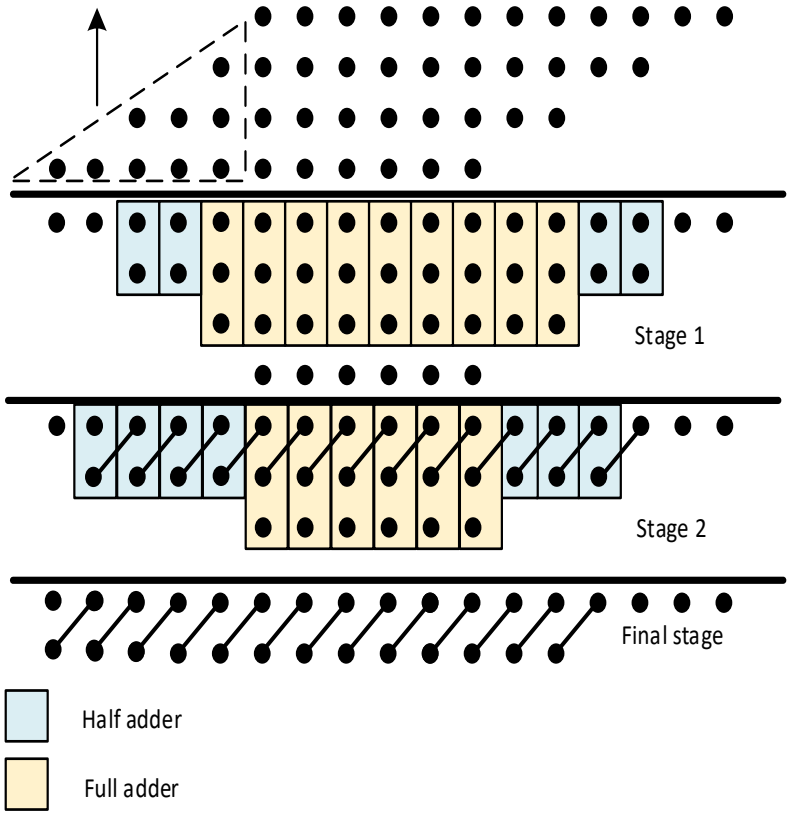

Figure 4-11: Dadda-tree reduction for the Partial-products rows generated using Modified-Booth-algorithm.

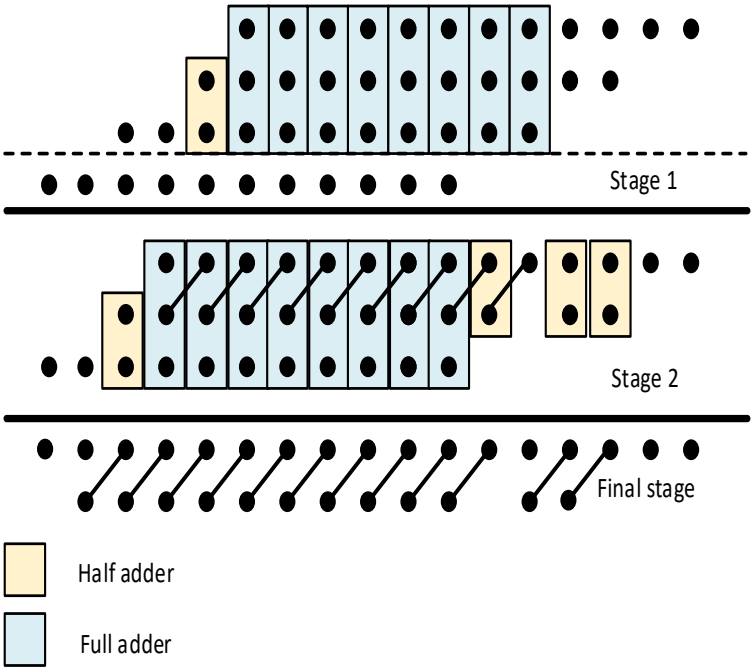

Figure 4-12: Proposed new Wallace-tree reduction scheme for the Partial-product rows generated using Modified-booth-algorithm.

The Wallace-tree and the Dadda-tree reduction algorithms are then applied to reduce the gate-count and the time-delay required to perform the partial-product summation. The results of each have been depicted in Figures 4-10 and 4-11 respectively. For simplicity and clarity, the partial products in the Figure 4-9 are represented using the dot symbol in the multiplier structures in Figures 4-10 and 4-11. In addition, the application of Modified-Booth-algorithm for the partial-product generation reduces the number of hardware stages required to perform partial addition to two stages.

In a nutshell, the Wallace-tree structure uses less hardware when compared to the Dadda-tree structure as portrayed in Figures 4-10 and 4-11 and hence, the Wallace-tree design will consume less power and have reduced hardware complexity than the Dadda-tree structure in this regard.

4.4.3 Proposed Modified-Booth-Wallace-Multiplier

The reduction tree structure described in the previous section employs both half-adder and full-adder in the first stages. However, the proposed new rules in the reduction-tree algorithm helps to further reduce the number of adders. In this regard, let us consider c as a column index and no_pp as the number of partial products in the particular column. The reduction-tree algorithm follows the following conditions (Lemma),

Rule-1: In stage-one, partial-product reduction should be implemented using full-adders only and half-adders should be avoided.

Rule 2: Half-adders can be employed in the first-stage MSB columns if and only if the no_pp of column c including the carry-bit from column $c-1$ is equal to no_pp of column $c-1$ excluding the carry bit from column $c-2$.

Based on these two new rules, the reduction-tree algorithm implemented in Figures 4-10 and 4-11 is modified and the new simplified corresponding structures are shown in Figures 4-12 and 4-13 respectively.

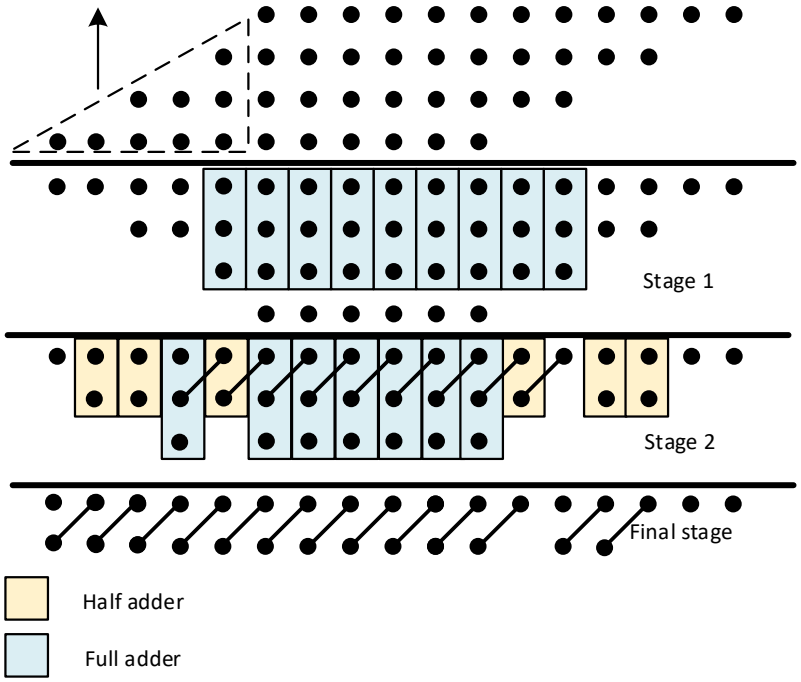

Figure 4-13: Proposed new Dadda-tree reduction scheme for the Partial-product rows generated using the Modified-Booth-algorithm.

The gate-count in Table 4-3 only includes the reduction-tree structure and excludes the gate-count for the partial-product generation and the final-adder structure for adding the last two rows. It is clearly seen that the gate count using the proposed new reduction-tree algorithms are lower when compared to the previous Wallace-tree and Dadda-tree algorithms. Although, there is no significant reduction in the gate-count using the proposed new reduction-tree algorithms, the values obtained is for a single multiplier only. Now considering, for instance, as stated in section 4.2, for Na number of antennas, there are $2Na^2 + Na$ number of baselines ($2Na^2$ – Na number of cross correlation and 2Na number of auto-correlation) and for each baseline it has N number of complex multiplication products. In total, we have $(2Na^2 + Na)N$ number of complex products. For calculating one complex product, four multipliers are used in each CMAC. So, to calculate one baseline the CMAC architecture requires 4N numbers of multipliers and overall it needs $(2Na^2 + Na) \times 4N$ number of multipliers for calculating all the baselines. Hence, for a small interferometer with N = 64 and Na = 256 it requires 33,619,968 multipliers. A single gate-count decrease in a multiplier will thus have a very significant improvement in the overall correlator ASIC design.

Reduction Algorithm	Full Adder	Half Adder	Total Gates
Wallace-tree	16	7	165
Dadda-tree	15	11	168
Wallace-tree (Proposed)	16	5	159
Dadda-tree (Proposed)	16	6	162

Table 4- 3: Gate Count Required for Different Reduction Tree Structures Using Modified Booth Algorithm

4.4.4 Modified ripple-carry-adder design

The findings from Table 4-3 reveal that the proposed new Wallace-tree architecture is the right choice of reduction-tree structure and the adder circuit for adding the last two rows is based on the final-stage values in Figure 4-12. The ripple-carry adder is the basic parallel adder and the simplest to design. But, the adder's delay increases with the increase in the number of full adders employed. Other adders like carry-lookahead adder, carry-bypass adder and carry-select adder are faster than the ripple-carry adder, but consume additional logic-gate overhead to perform the operation faster. The final stage rows in Figure 4-12 help to improve the ripple-carry-adder shown in Figure 4-14 by using a half-adder to generate S5 since the column five has just one input value and bits S0 to S16 are the required final product value.

As mentioned earlier, a small increase in the gate-count in a single multiplier will increase the overall hardware cost of a correlator. The proposed design in this work is mainly targeted to minimize the area and power utilization of these correlation cells. The Modified-Booth-algorithm and the proposed new reduction-tree structure serve as a solution to reduce the overall delay before the final-stage. The proposed structure using the ripple-carry-adder for the last two rows also meets

the requirement for handling 11Tbps of data, since it has lower delay when compared with the conventional method.

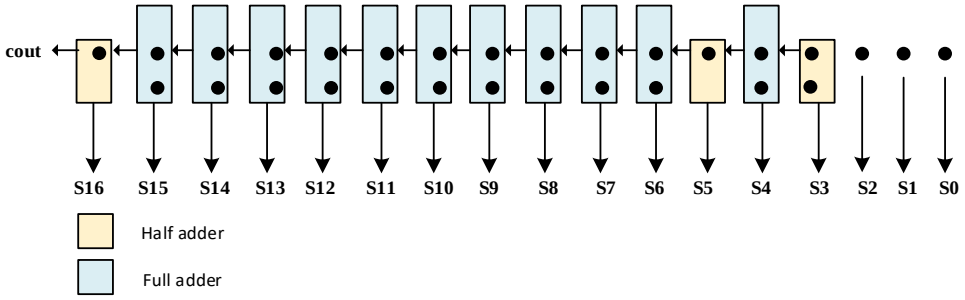

Figure 4-14. Modified ripple-carry-adder for adding the last two rows in Figure 4-12.

The addition of the last two rows using the different adder types mentioned earlier result in less delay, the design with ripple carry adder is preferred, as it occupies less area and consumes less power. Hence, in this implementation the design uses ripple carry adder for the final stage adder to add the last two rows is shown in Figure 4-14. The proposed Modified-Booth-Wallace -Multiplier design to perform the 8×8 complex multiplication in correlation cells is shown in Figure 4-15.

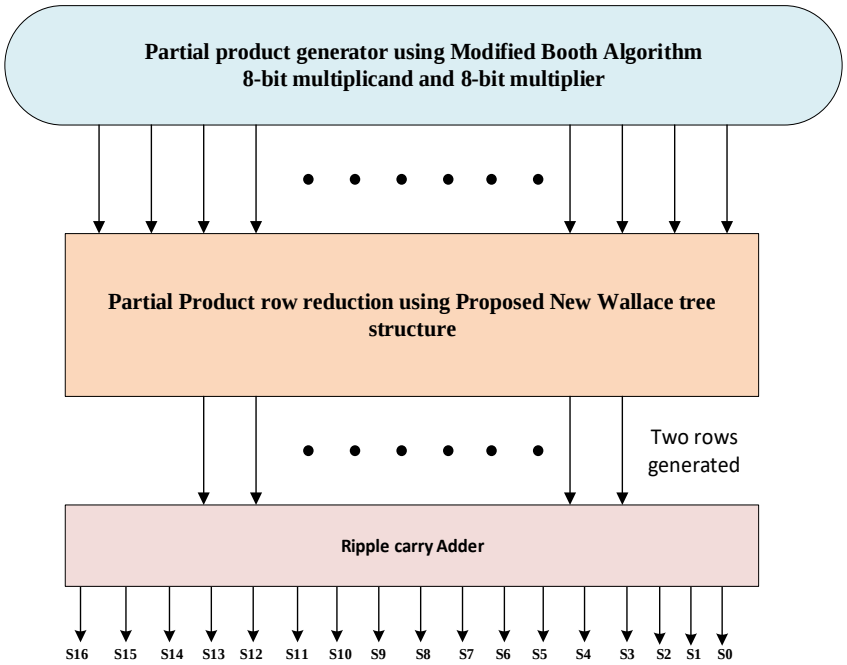

Figure 4-15. Proposed Modified-Booth-Wallace-multiplier for performing 8×8 complex multiplication for correlation cells (CMAC, CoSMAC, PE_IQ and PE).

4.5 Implementation and Analysis of Correlator Cells

Verilog hardware description language (HDL) is utilized to create the register transfer level (RTL) design for both the proposed and conventional (existing) cells. The 28nm HPP (high performance process) GF CMOS standard cell library is used to synthesize the design along-with timing constraints based on the clock frequency $f_{clk} = 400\,MHz$ and dump time $T = 64$ (64 time slices). The physical layer standard cells in this deep nanometric CMOS library are available with various process-voltage-temperature (PVT) corners [157]. In order to evaluate the worst-case situation, CMOS standard cells with slow corner specification along with 0.765 V drain-to-source voltage and $-40℃$ operating temperature are instanced. The synthesis is carried out using the Cadence Encounter RTL compiler and Cadence SOC Encounter is used for the Layout implementation. The pre-simulation and post-simulation process are carried out using Mentor graphics model sim. The implementation and analysis are done only for the CMAC, CoSMAC and PE correlator cells. The Functionality of PE_IQ is almost same as that of the PE and also, it requires some work around in the input section and hence decided to implement and analysis it in the future work.

The proposed CoSMAC and PE correlator cells are implemented using the 28nm CMOS technology. The existing CMAC cell designs mentioned in other works are in different technology, whose area and power efficiency are not accurately comparable with the proposed CoSMAC and PE implementations in 28nm CMOS technology. The supply voltage of the 28nm CMOS process is considerably scaled to 0.85V, the proposed designs will be inherently more power efficient compared to previous CMAC cells housed in lower technologies (larger channel lengths) with higher supply voltages. Also, the chip-size will be much smaller for the proposed new cells in the advanced CMOS technology. Therefore, the conventional CMAC architecture is also implemented in 28 nm to emphasize the efficiency of the proposed correlator-cells with respect to power and area utilization.

4.5.1 Implementation of correlator-cells with Modified-Booth-Wallace-Multiplier

The conventional CMAC cell, CoSMAC and PE are synthesized using 28nm HPP CMOS standard library cells. The Figures 4-16, 4-17 and 4-18 show the RTL view of the correlator-cells. In all the three correlator cells they have four 8-bit temporary registers t1, t2, t3 & t4 which are used to store the real input values Rx, Ry and imaginary input values $Iz\ and\ Iy$ respectively. The output accumulators are 32-bit each to store either 64-bit (32-bit real + 32-bit imaginary) complex number for cross correlation or to store 32-bit real number for auto-correlation. The output data from the adder, subtractor block in Figures 4-19 and 4-17, and adder/subtractor block in Figure 4-18 are integrated in this 32-bit accumulator registers for the dump period of T and finally the accumulated value is read out and cleared in the next clock cycle. The RTL view of correlator-cells with conventional multiplier or with Modified-Booth-Wallace-Multiplier looks similar, since only the internal architecture of the multiplier block differs. Therefore, the RTL diagrams shown in Figure 4-16, 4-17 and 4-18 are common for both conventional and proposed multiplier architectures. The RTL view of the Modified-Booth-Wallace-Multiplier is shown in Figure 4-19.

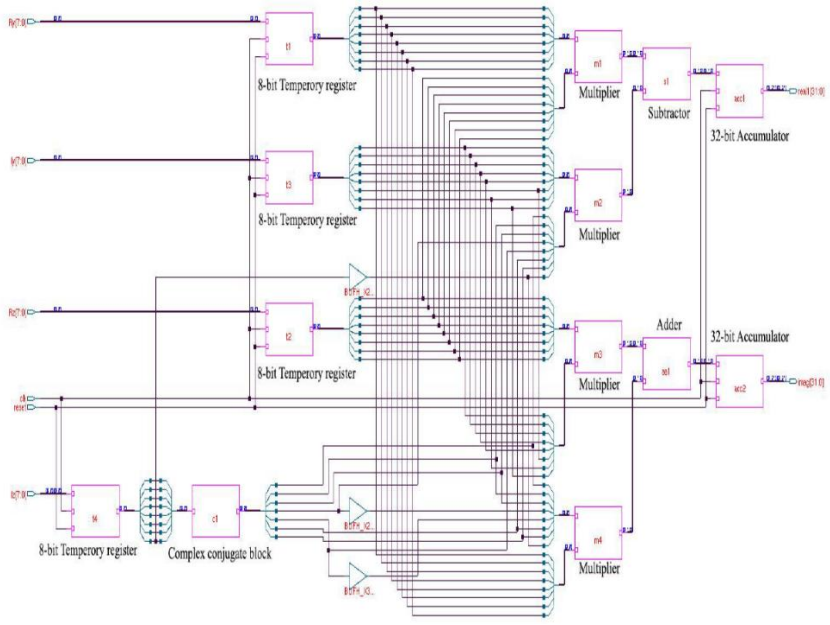

Figure 4-16: RTL Diagram of CMAC for calculating one Cross correlation visibility per clock cycle in single cross correlation baseline.

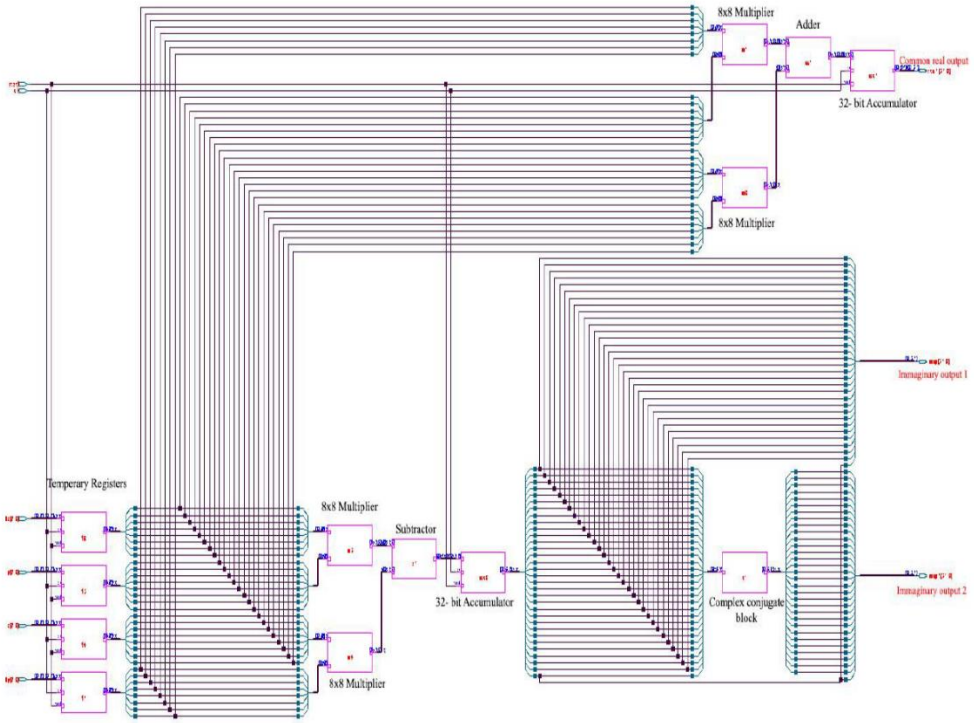

Figure 4-17: RTL diagram of a CoSMAC cell for calculating two cross correlation visibilities for a single baseline in single clock cycle.

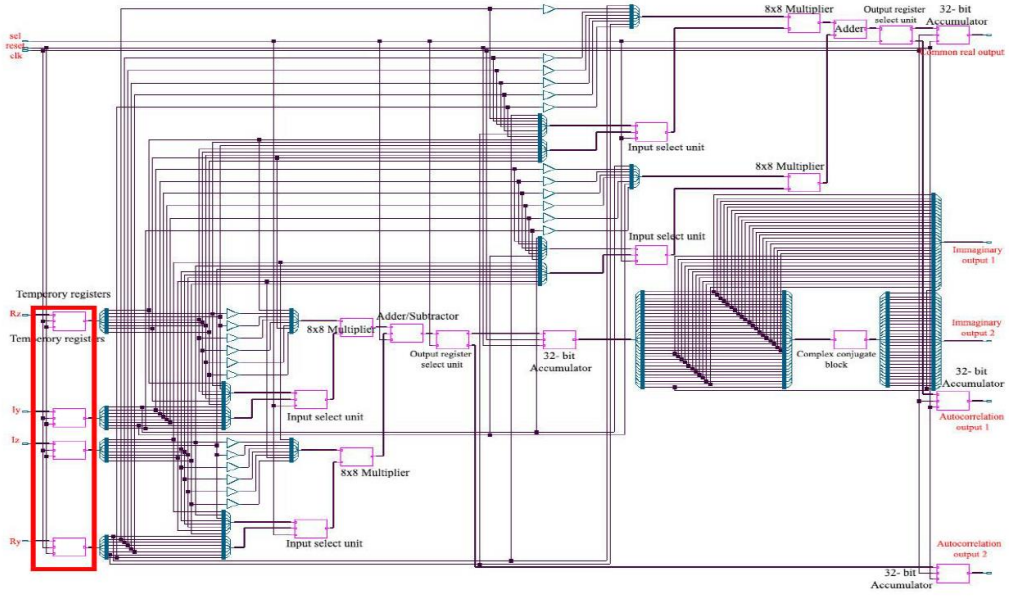

Figure 4-18: RTL diagram of a PE cell for calculating two cross correlation visibilities for a single baseline and two visibilities for two Auto Correlation baselines in a single clock cycle.

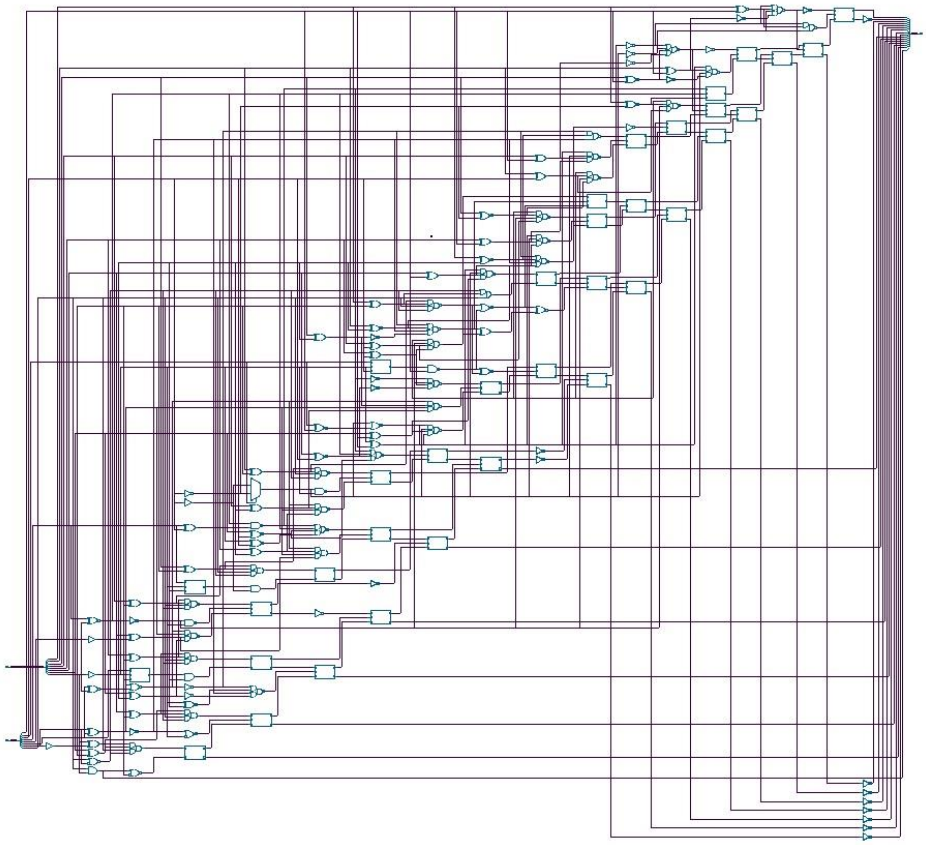

Figure 4-19: RTL diagram of proposed Modified-Booth-wallace-Multiplier

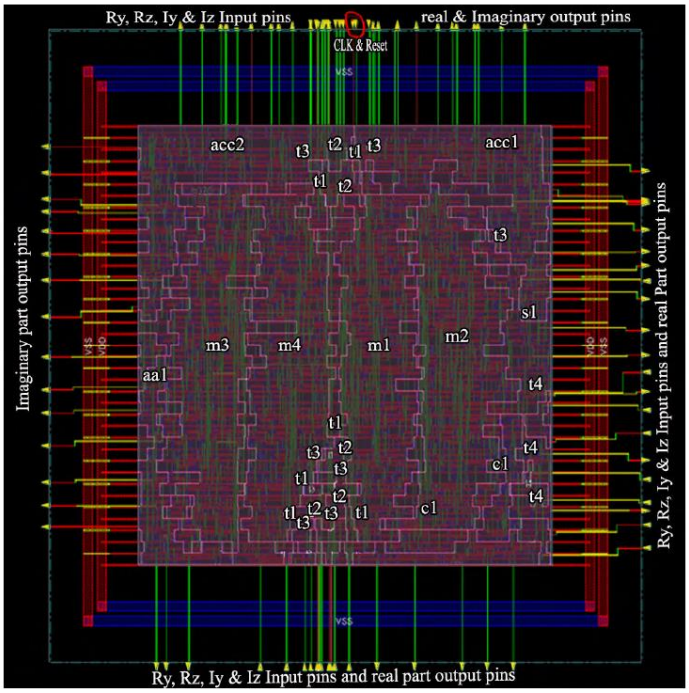

Figure 4-20: Merged physical layout and amoeba view of conventional CMAC with Modified-Booth-wallace-multiplier, size (1431 μm^2)

The proposed multiplier implementation on conventional CMAC shall also be considered as a new optimised CMAC design that can be used to calculate simple complex number multiplications with less gate count.

The mask layouts of the correlator-cells with Modified-Booth-Wallace-Multiplier, using the GLOBALFOUNDRIES 28nm CMOS28HPP RVT C38 0.85-volt SC12MC High Performance Standard cells of ARM IP, are shown in Figures 4-20, 4-21, and 4-22 respectively. The routing is implemented using a five metal BEOL (back-end-of-line) stack. In these three Figures 4-20, 4-21 and 4-22, the Logic components m1, m2, m3 and m4 are 8×8 multipliers; t1, t2, t3 and t4 are 8-bit input registers to store Ry, Rz, Iy and Iz; acc1, acc2, acc3 and acc4 are 32-bit accumulators; c1 is a complex conjugate block; aa1 is a 16-bit adder; In Figure 4-22 s1 is a 16-bit adder/subtractor whereas s1 in Figures 4-20 and 4-21 is a 16-bit subtractor; In Figure 4-22 d1 and d2 are the output register select blocks; and mu1, mu2, mu3 and mu4 are the input select blocks. The SEL signal for PE is derived from the clock, it is internally wired and hence not shown at the cell edge in Figure 4-22.

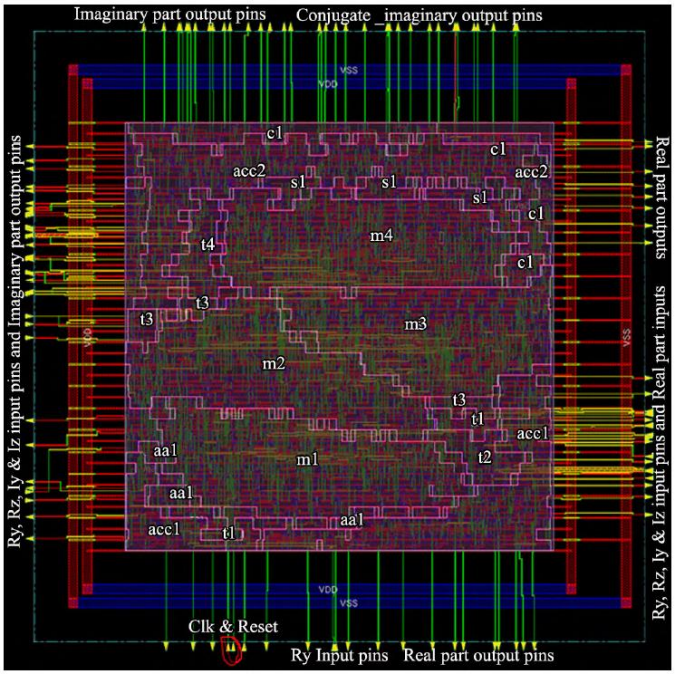

Figure 4-21: Merged physical layout and amoeba view of new CoSMAC cell with Modified-Booth-wallace-multiplier, size ($1495\ \mu m^2$*)*

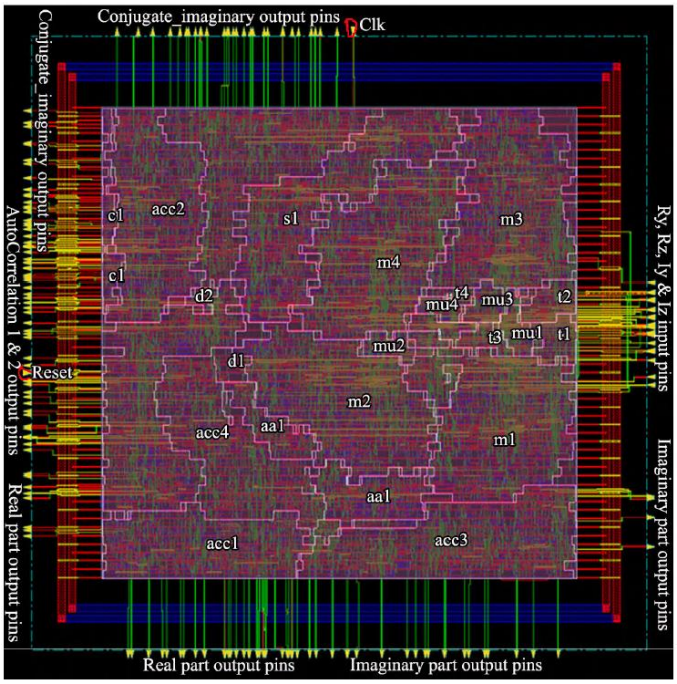

Figure 4-22: Merged physical layout and amoeba view of new PE cell with Modified-Booth-wallace-multiplier, size ($3115\ \mu m^2$*)*

4.5.2 Area and Power utilization of correlator-cells

The power and area utilisation for a conventional CMAC, and the newly designed CoSMAC and PE cells using both conventional multiplier and Modified-Booth-Wallace-Multiplier are summarised in Table 4-4. Although, the power dissipation and area for the conventional CMAC cell seems to be less, it is only for calculating one visibility per baseline. The CoSMAC cell which is designed to exploit the computationally minimized X-part algorithm, calculates two visibilities per baseline, utilising a slightly higher area and dissipating almost the same amount of power.

The calculation of two visibilities involves two conventional CMAC cells and has an overall power dissipation of twice its initial value which is higher than the use of a CoSMAC cell for the same. On the other hand, a PE cell calculates six visibilities (two Cross correlations and four Auto correlations) in one clock cycle and hence the overall area utilised, and power dissipated listed in Table 4-4 is lower per visibility compared to the CoSMAC and far lower compared to the conventional CMAC. Meanwhile, calculation of these six visibilities in PE can be

done using CMAC cells in two ways ; either by the allocation of individual CMAC cells or by using the concept of CMAC reuse [104]. The former method increases both the area and power dissipated whereas the latter utilises less area but with the cost of three times the power of a single CMAC cell.

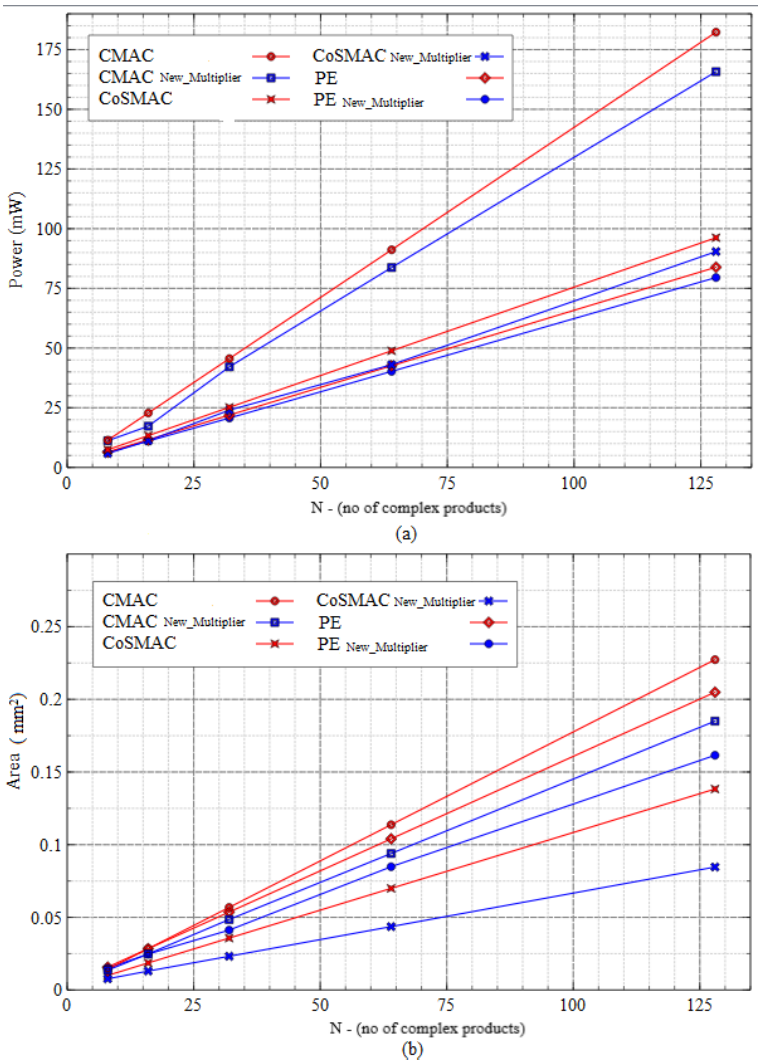

Figure 4-23: Power and Area utilization comparison of correlator-cells using proposed (Modified-Booth-Wallace-Multiplier) and conventional multiplier design for calculating N number of cross products, (a) Power consumption, (b) Area utilization.

Therefore, the use of a PE cell in this regard utilises less area and dissipates less power and hence proves to be a more efficient replacement for the CMAC. The calculation of one cross-correlation baseline for different sample length $N = 2^r, where\ (r = 3,4,5,6,7)$, requires N number of CMACs and $\left(\frac{N}{2} + 1\right)$ CoSMACs. It is evident that as N increases, the power consumed also increases

linearly. For lower values of N, the power consumed by a CoSMAC is slightly lower than that of a CMAC but for larger values of N, the power consumed by a CoSMAC is almost half of that consumed by a CMAC cell as shown in Figure 4-23 (a). Similarly, the use of PEs to calculate Autocorrelation baselines along with the Cross correlations of the same inputs yields less power consumption than CMAC and CoSMAC.

	CMAC		**CoSMAC**		**PE**	
	1*	**2****	**1***	**2****	**1***	**2****
Dynamic Power(µW)	712	698	740	728	1290	1265
Standard cellInstances	1019	991	1093	1059	2581	2541
Area (µm2)	1476	1431	1537	1495	3153	3115
Cross products calculated per clock	1	1	2	2	2	2

1* Design with conventional Multiplier 2** Design incorporating the new multiplier

Table 4- 4: Power and area of 28nm HPP CMOS ASIC synthesized correlator-cells design.

The area and the power dissipation estimates are less for the new correlator cells when compared to the conventional CMAC. The CoSMAC architecture uses fewer cells than the CMAC architecture to calculate the cross-correlation baselines as shown in Figure 4-23 (b). It can be inferred that as the value of N increases, the initial slightly higher area by a PE reduces as compared to that of a CMAC as shown in Figure 4-23 (b). Similarly, the proposed multiplier design adds additional optimization to correlator cells and further reduce the area and power as shown in Figure 4-23. Therefore, the use of CMAC in constructing Correlator for large interferometers incurs more area and higher power dissipation. The overall power and area utilization of the correlator-cells using conventional and proposed multiplier for different values of N are obtained using Encounter RTL tool and summarized in the Table 4-5 and Table 4-6 respectively. The comparison of Table 4-5 with Table 4-6 shows that the power consumption and area utilization of the correlator-cells design are significantly reduced if the N value increases.

4.6 Summary

The implementation process is carried out using the 28nm CMOS technology standard cell libraries for CMAC, CoSMAC and PE correlation cells. The analysis among the three implemented correlator cells proves that the area and power of the overall correlator cell is minimised by replacing the conventional CMAC cell with the newly designed CoSMAC and PE cells. When the number of antennas increases, the difference between the utilisation factor of CMAC is very high when compared to CoSMAC and PE. In addition, the optimised Modified-Booth-Wallace-Multiplier design further reduces the power consumption and area of all the three correlator cells. The optimised multiplier uses modified booth algorithm for partial product generation and Wallace tree for the reduction process with some additional conditions.

Design	N =8		N =16		N =32		N =64		N =128	
	Power (mW)	Area (mm^2)	Power (mW)	Area (mm^2)	Power (mW)	Area (mm^2)	Power (mW)	Area (mm^2)	Power (mW)	Area (mm^2)
CMAC*	5.7	0.0118	11.394	0.0236	22.788	0.0472	45.575	0.0945	91.15	0.1889
CoSMAC*	3.7	0.0077	6.66	0.0138	12.582	0.0261	24.424	0.0507	48.108	0.0999
CMAC+	11.394	0.0142	22.788	0.0284	45.575	0.0568	91.15	0.1137	182.3	0.2273
CoSMAC+	7.401	0.0100	13.322	0.0186	25.163	0.0357	48.848	0.0699	96.215	0.1383
PE+	6.451	0.0157	11.612	0.0284	21.934	0.0536	42.578	0.1040	83.866	0.2049

* Calculating one Cross- correlation baseline, + Calculating one cross- and two auto-correlation baselines

Table 4- 5: Power and area usage of array of correlator-cell with conventional multiplier for different values of N.

Design	N =8		N =16		N =32		N =64		N =128	
	Power (mW)	Area (mm^2)	Power (mW)	Area (mm^2)	Power (mW)	Area (mm^2)	Power (mW)	Area (mm^2)	Power (mW)	Area (mm^2)
CMAC*	5.586	0.0114	8.92	0.0224	20.64	0.0457	41.32	0.0915	83.25	0.1826
CoSMAC*	2.92	0.0053	5.16	0.0106	11.732	0.0208	21.294	0.0412	46.1	0.0822
CMAC+	11.17	0.0136	17.28	0.0248	42.13	0.0485	83.72	0.0939	165.75	0.1850
CoSMAC+	5.84	0.0077	11.17	0.0130	23.98	0.0232	43.032	0.0436	93.4	0.0846
PE+	6.3	0.0150	11.01	0.0247	20.68	0.0412	40.224	0.0848	79.53	0.1615

* Calculating one Cross- correlation baseline, + Calculating one cross- and two auto-correlation baselines

Table 4- 6: Power and area usage of array of correlator-cell with Modified-Booth-Wallace Multiplier for different values of N.

CHAPTER 5: DESIGN OF NON-REDUNDANT MATRIX ARCHITECTURE ALGORITHM

In matrix format, the complex multiplier and accumulators (CMAC) are arranged in an array structure with each baseline associated with an individual unit, whereas in the pipeline architecture, the CMACs are arranged in series as shown in Figure 5-1. In general, the memory read and write operations consume more power; memory will refresh frequently to hold the state which also consumes power. In the pipeline architecture, it uses a common bus among the CMACs and the data from the F section are serially transmitted with some integration time between each CMAC, which involves more memory. In the thesis, a summary of all the five architectural designs is shown in Table 3-2. In the first architecture, it uses a dedicated CMAC for each baseline and does not require memory for buffering, resulting in less power consumption. Whereas, all other architectures use memory for buffering which increases the overall power consumption. On comparing pipeline architectures (4 & 5) with the other three types, the system requires a greater number of ICs that are used to perform the complex multiplication with accumulation operation and consumes more power. The percentage of area occupied in the die by the memory is about 67% for architecture 3 and more than 94% in architectures 4 and 5, thus causing high power consumption. The constant memory access performed in the Pipeline architecture escalates the power consumption relatively higher. This makes the matrix architecture more efficient and faster.

The basic baseline computing cell in X-section of a FX correlator architecture is the Complex multiplier and Accumulator which does the cross and auto correlation of signal samples received from the F-Section after FFT. The Section 4.2 clearly explains the baseline calculation of large interferometers in FX correlators using conventional CMAC as a basic cell in its X-section. The conventional CMAC cell calculates only one visibility per baseline and it must be reused multiple times to calculate more than one visibility which consumes more power. In this design process, the conventional CMAC is replaced by the new

COSMAC and PE ASIC correlation cells with the power-efficient multiplier designs proposed in the previous sections. The PE is greater in area when compared to conventional CMAC cell, but it calculates more outputs than the CMAC. Also, in the dedicated CMAC matrix architecture, it requires to use individual CMACs to calculate all the visibilities in parallel. For example, four CMACs are required to calculate two cross and four autocorrelations or two CMACs to calculate cross correlation first and again reused to calculate the autocorrelation. Both the approaches will have more area when compared to PE. This replacement reduces the number of correlation cells required for the computations of the baselines of a correlator.

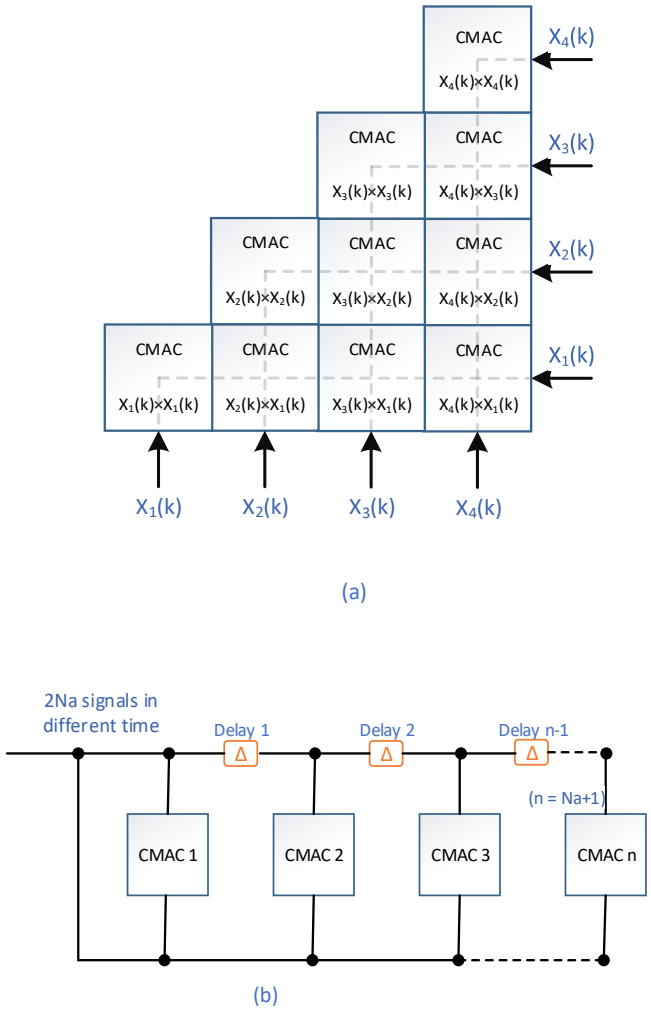

Figure 5-1: Conventional designs (a) Matrix Architecture for four signals (b) Pipeline architecture for 2Na number of signals.

5.1 Non-redundant Matrix Algorithm

To calculate the total number of baselines for Na number of dual polarised antennas in a single input memory read, it requires $2Na^2 + Na$ number of CMACs. In Figure 5-1 (a), the matrix architecture is used to calculate correlation between the two dual polarised antennas (4 signals). It requires 10 CMACs to calculate all baselines with a single memory read, ie., the input buffers in each CMAC is loaded by the samples accrued at the same integration time period m from the four signals (2 dual polarised antennas, $Na = 2$). But, by using CoSMAC and PE it requires only 6 cells to calculate all 10 baselines in a single input memory read as shown in Figure 5-2. When reusing the CMACs to calculate autocorrelation after performing cross-correlation, it requires two input memory read operations. This reduces the number of CMACs required to $2Na^2 - Na$. Two auto-correlations can be calculated using a single CMAC and hence for calculating four auto-correlation baselines in Figure 5-1 (a) it needs two CMACs to be reused.

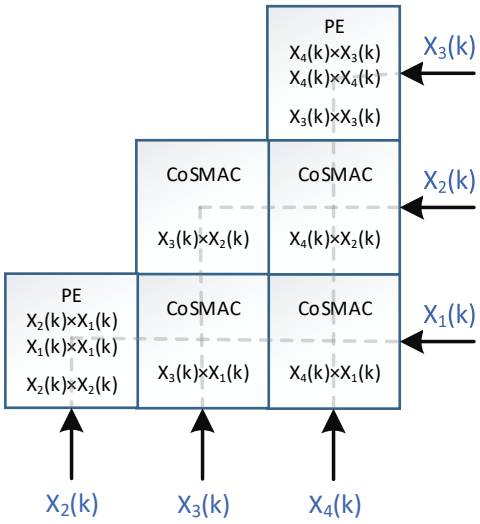

Figure 5-2: Matrix Architecture to calculate correlation for four signals using CoSMAC and PE with single input memory read.

In the first input memory read, controller loads the six CMACs input buffers with cross-correlation values to be calculated and in the next cycle it loads two CMAC buffers with the auto-correlation values. The remaining four CMACs are

not involved in the calculation of the baseline but still consumes power. The power usage can be reduced by turning-off the four CMACs during the auto-correlation baseline computation process but is still slightly higher than the power dissipation for baseline calculations employing CoSMAC and PE cells with single input-memory read in a single-cycle (Refer Table 4-4). The CMAC implementation also involves extra circuitry to control the operations in the two cycles.

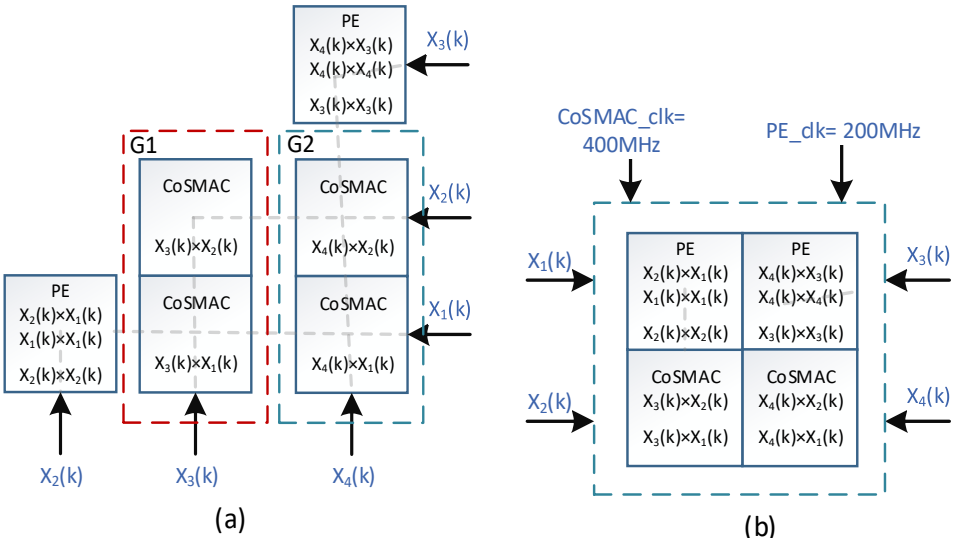

Figure 5-3: (a) Grouping of Cross-Correlation operation performed by CoSMACs, (b) Four Correlation cells (2 CoSMAC + 2 PE) to calculate 10 baselines.

In the proposed matrix architecture employing the CoSMAC and PE cells, the operation of these correlation cells is altered slightly to improve the performance. The two different clocks of 200 MHz and 400 MHz range have been employed. The PE is driven by the 200 MHz clock and the CoSMAC is driven by the 400 MHz clock since the PE operates both in the positive and the negative edges of the same clock to calculate cross and auto correlation. The cross-correlation is obtained during the positive-edge trigger and the auto-correlation is available at the negative-edge trigger. It means that the PE is also effectively operating at 400 MHz clock. In Figure 5-3 (a), the cross-correlations performed by the CoSMACs is grouped into G1 and G2. In G1, the frequency sample $X_3(K)$ of signal X_3 is common for the two CoSMACs and similarly in G2, the frequency sample $X_4(K)$ of the signal X_4 is mutual on both the CoSMACs. Only the frequency samples

$X_1(K)$ and $X_2(K)$ of the signals X_1 and X_2 respectively are varying in both the groups, and hence, each group can be replaced with a single CoSMAC. This reduces the number of required input buffers and allows the sharing of an input buffer by the G1 and G2 CoSMACs. Here, the shared second input buffer is loaded with the sample $X_1(K)$ in the first-cycle and then by $X_2(K)$ in the next cycle of the 400 MHz clock. Therefore, all the 10 baselines are calculated within the same time-period by using four correlator cells (2 CoSMACs + 2PEs) as shown in the Figure 5-3 (b).

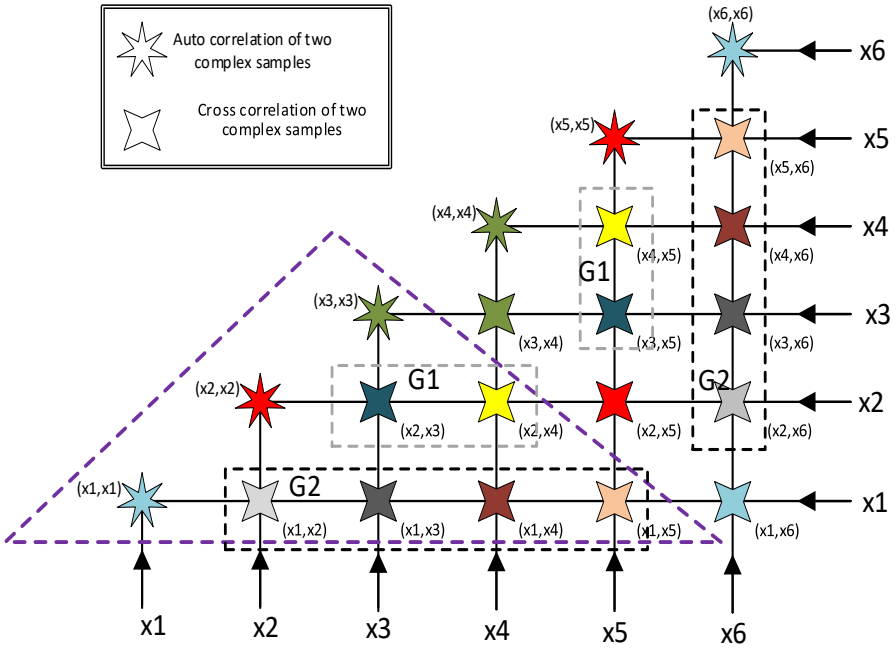

Figure 5-4: Baseline formation of Na=3 dual polarised antennas with the grouping of baselines that shares the common Correlator cell (CoSMAC and PE)

In the same way, the baselines for odd number of dual polarised antennas Na = 3 are performed as shown in Figure 5-4. The identical colour of stars represents the baselines calculated in the same Correlator cell. For example, the N products (N "visibilities") for each of the auto- correlation baselines (x1, x1), (x6, x6) and the cross-correlation baseline (x1, x6) of signals x1 and x6 are all calculated using the same PE in N cycles of a 200 MHz clock. The single CoSMAC used to calculate the cross-correlation baselines (x5, x4) and (x2, x4) of signals x2, x4 and x5 are all

represented in the same colour. In the first cycle of 2N cycles of the 400 MHz clock, the first visibility of N visibilities of the baseline (x5, x4) is calculated and in the second cycle of 2N cycles of the 400 MHz clock the first visibility of the N visibilities of (x2, x4) baseline is calculated. The computations of the 2N CoSMAC cycles at 400 MHz are completed in N cycles of the 200 MHz PE clock. When comparing the column and row G2 groups, the signals x2, x3, x4 and x5 are common, and only x1 and x6 are different. Hence, only one of these groups of 4 CoSMACs is needed with signal samples $X_1(m,K)$ and $X_6(m,K)$ loaded in a shared buffer in alternate cycles in a 2N cycle period of the 400MHz CoSMAC clock. In this case, the buffer will be smaller but there will be frequent memory access.

On the other hand, in another scheme, all the signal samples $X_1(m,K)$ could be loaded in the shared buffer for the first N cycles and then all the signal samples $X_6(m,K)$ could be loaded in the same buffer for the next N cycles. This way the buffer will be larger, but memory access will be reduced. Similarly, for the column and row G1 groups, signals x3 and x4 are common while signals x2 and x5 are different. Hence, only one of these two groups consisting of 2 CoSMACs is needed with signal samples $X_2(m,K)$ and $X_5(m,K)$ loaded in alternate cycles in a 2N cycle period of the 400MHz CoSMAC clock. Also, as above, in another scheme all the signal samples $X_2(m,K)$ could be loaded in the shared buffer for the first N cycles, and then, all the signal samples $X_5(m,K)$ could be loaded in the same buffer for the next N cycles. For the auto- correlation baselines (x2, x2), (x5, x5) and the cross-correlation baseline (x2, x5) of the signals x2 and x5, all of these can be calculated employing the same single PE in N cycles of its 200MHz clock with cross-correlations completed in the rising-edge and the autocorrelations completed in the falling-edge for each sample pair $X_2(m,K)$, $X_5(m,K)$. Similarly, for the auto- correlation baselines (x3, x3), (x4, x4) and the cross-correlation baseline (x3, x4) of signals x3 and x4, all of these can be calculated employing another PE. Hence, in accordance with the above explanation, all the 21 baselines for three dual-polarized antennas (Na=3) are calculated using three PEs and six CoSMACs as represented by the cells within the triangle in the Figure 5-4. The redundant

processing cells are thus eliminated in this new matrix architecture resulting in a reduction of hardware cost by over 50%. Also, this proposed architecture simplifies the buffer design and makes it possible to have a shared input buffer for every group to hold the second complex sample for complex multiplication. i.e., G1 and G2 can have separate common buffers to hold x2 in G1 and x1 in G2 during first cycle and replace it with x5 and x6 respectively in the next cycle. This reduces the required buffer size in the architecture which streamlines the memory read and simplifies the data corner turner operations required for the correlation.

In general, the proposed architecture just requires $Na \times Na$ number of correlation cells (the required number of CoSMAC cells = $Na^2 - Na$ while the required number of PE cells = Na) to calculate the total of $2Na^2 + Na$ baselines for all the Na dual polarised antennas. In comparison, the conventional method requires $2Na^2 - Na$ complex multipliers (CMACs) to calculate the same number of correlation baselines.

5.2 Reusability technique

When the number of antennas increases, it becomes difficult to complete the baseline calculations in parallel within a single VLSI chip, since the large number of correlation cells required cannot be squeezed within a single chip. For instance, for 512 ($Na = 512$) dual polarized antennas, there are 524,800 baselines for correlation calculations, which means it requires 523,776 CMACs to perform all the correlation operations using the conventional matrix architecture. However, it is not possible to accommodate all these CMACs to implement these computations within a single VLSI Chip (single IC). Therefore, if say, $n \times n$ array of CMACs are fabricated on a single IC, then it can be reused multiple times to calculate all these 524,800 baselines, or, by concurrently employing multiple of these $n \times n$ array IC's for several times all the baseline calculations can be completed. Now considering, $n = 64$ there would be an array of 4096 CMACs on a single IC. This IC must be reused multiple times, say, Z_{times} to calculate all the baselines for the 512 antennas. This reuse factor can be calculated using equation (5-1) below and for 512 dual polarized antennas, it is equal to 128 times.

$$Z_{times} = \frac{2Na^2 - Na}{n^2} \tag{5-1}$$

To reduce the required number of iterations of reuse, say, q number of array ICs can be used concurrently so that the reuse factor can be reduced to $\frac{Z_{times}}{q}$ times to complete the calculations for all the baselines. For example, eight concurrent 64 × 64 array CMAC ICs need to be reused 16 times to calculate the visibilities for all the 524,800 baselines of 512 dual polarized antennas. Whereas, in the proposed non-redundant matrix architecture for the same 512 ($Na = 512$) antennas and with $n = 64$ it requires only half of the hardware resources. As explained above, the proposed architecture requires only $Na \times Na$ number of correlation cells. For calculating visibilities for 524,800 baselines, it requires only 262,144 ASIC correlation cells (261,632 CoSMACs and 512 PEs). Hence, the reuse factor Z_{times} is reduced Z'_{times} to almost half as indicated in equation (5-2) below, compared to equation (5-1) above, and, for Na = 512 the reuse factor is just 64 times.

$$Z'_{times} = \frac{Na^2}{n^2} \tag{5-2}$$

On the other hand, if eight 64 × 64 array single-chip correlation cell ICs are employed concurrently, they need to be reused only 8 times to calculate the baseline correlations for all the 512 dual-polarized antennas. The proposed new matrix architecture thus reduces the required number of IC's and the total time needed to process the overall bandwidth produced from the Na number of dual-polarized antennas.

Let's consider the operating frequency of the CMAC IC is at the clock rate of f_{clk}. This has the capability of processing the total bandwidth of $Tb = \frac{f_{clk}}{Z_{times}}$. To calculate the complete integration time of m, the memory accessed by this IC should hold N number of samples from all the signals received from the antennas. But, the proposed architecture based on correlator cell with the clock rate of same

f_{clk} can process the total bandwidth of $Tb = \frac{f_{clk}}{Z'_{times}}$. Also, in this case the memory requires to hold only $\frac{N}{2} + 1$ number of samples per signal for any time-slice m, to calculate the visibilities for the overall integration time (dump period).

For example, with the operating frequency of $200\ MHz$ CMAC architecture IC, using 64×64 array structure, it is possible to process the bandwidth of $Tb = 1.565\ MHz$ for 512 antennas. While using the proposed architecture with same frequency and 64×64 array format, it is possible to process the bandwidth of $Tb = 2.94\ MHz$ for 512 antennas. Also, the memory size required to store N number of samples per signal is reduced to $\frac{N}{2} + 1$. The proposed architecture has each sample size of 16 bit (8b+8b) complex numbers and the outputs from accumulator after the integration time period is of 64-bit complex number. The 64×64 array structure using the proposed architecture is capable of calculating baselines for 64 antennas, i.e. it can process 128 input samples or 2048 bits per iteration from 64 dual polarised antennas after the FFT process in F-section. For the clock frequency of $400\ MHz$ the IC can process 102.4 GBps (Giga bytes) or 51.2 giga complex samples per second. Figure 5-5 shows the estimated power utilisation of both CMAC architecture and CoSMAC & PE architecture for calculating all the correlated baselines for different number of antennas. As the number of antennas increases the proposed architecture utilise much less power than the CMAC architecture. The power is not linearly increased in Figure 5-5, since it's not directly depend on the number of antennas but it's totally based on the reuse factor and the count of Correlation cells. This is because the number of correlations required is not linearly increased as antennas grows (correlations = $2Na^2+Na$, Na is the number of antennas).

5.3 Summary

The conventional CMAC cell used in Matrix architecture is replaced with the proposed CoSMAC and PE cells. This proposed architecture reduces the number of required correlation cells to Na^2 for calculating the total of $2Na^2 + Na$ baselines for all the Na dual polarised antennas. The conventional matrix

architecture method needs $2Na^2 - Na$ CMACs to perform the same baseline calculations in parallel. The proposed architecture nearly reduces half of the hardware requirements without degrading the performance. The reusability factor and the number of ICs required to perform the overall correlation is also reduced to Z'_{times}.

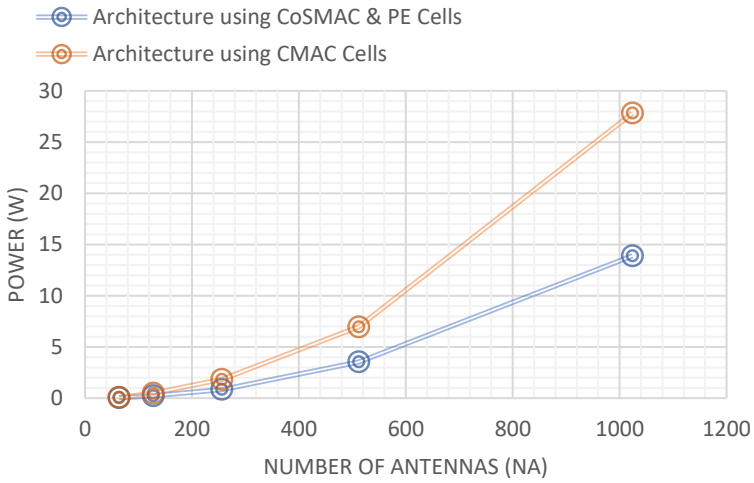

Figure 5-5: Graphical representation of Power utilization by different values of Na (number of dual polarized antennas) using CMAC and CoSMAC & PE cells

CHAPTER 6: CONCLUSION

The research outcomes of this thesis work are described and summarised in this chapter. The key findings of this research work are concluded and all the key contributions to knowledge are identified. Details on the future scope of this design are also discussed with some recommendations for improvement.

6.1 Research Summary

This research work describes and discusses the design of an area efficient ASIC correlator architecture of the X-section in FX-correlators. An insight into radio astronomy, importance of interferometry techniques and types used in finding out celestial bodies of space throws light on the current state of the art systems and architectures. In addition, the Fourier transform is widely used in understanding the real-time signal characteristics in the frequency domain. Various correlator and multiplier architectures are analysed enlightening on the pros and cons of each category. The disadvantages of the conventional designs are mitigated, and this novel research work has been proposed and implemented.

Conclusions are drawn on the choice of correlators and multipliers used in large interferometers after a thorough analysis of the existing systems. The FX-correlator is preferred since the multiply and accumulate unit is not dependent on the frequency channel count. Moreover, it is evident that the selection of multipliers is more important, as this is the basic component for calculating complex multiplications and a small gate count reduction in a multiplier makes an impact on the performance of the system in terms of power dissipation and area of the design.

Large interferometers require massive computational and memory hardware to process the received big data signals for suitable radio-astronomical image formation which also involves calibration of raw visibilities to sky visibilities (sky brightness). This is necessary for generating the enormous number of channel-wise and base-line-wise visibilities through cross- and auto- correlation among the signals at over 11 Tbps composite throughput rate. This thesis reduces the

computational requirement by nearly 50% without degrading the speed and performance of the correlator. Mathematical computations and the simulation results discussed in this regard also reveal that the computationally minimized CoSMAC, PE and PE_IQ (only mathematical computation) algorithm proposed for the baseline calculations in the X-part of the FX-correlator and the corresponding optimized hardware architecture exploits the redundancies in correlation products and generates the complete visibility spectrum (including those for the conjugate channels) for image formation using only $N/2 + 1$ (just about 50%) frequency channel samples from the F-section. The performance analysis of the suggested CoSMAC and PE cells in the ASIC (VLSI) implementation clearly prove that the energy efficiency is enhanced many-folds in addition to enabling the processing of Tera-scale input data-rate by the X-section. This reduction lowers the memory capacity and the number of memory read operations which greatly reduce the power consumption as the memory operations significantly increase the power utilisation. This work thus provides a computational solution for some emerging Big-data problems.

Development and implementation of a new multiplier that is optimized through a combination of Modified-Booth-algorithm and a modified reduction-tree algorithm (a modification of the Wallace-tree algorithm) for further improving the computational efficiency in FX correlator interferometry has been done. The area and power utilization are reduced further by incorporating this new optimized multiplier in the correlator cells. The optimised multiplier designed and implemented in this work has six transistors less in number when compared to the existing fast multiplier architecture. Therefore, in total, for Na number of antennas $[(2Na^2 + Na) \times 4N] \times 6$ number of transistors are reduced.

This minimized multiplier is geared towards exploratory ASIC design for the X/B (Correlator/ Beam-former) – engine of the SKA Mid CBF. The 28 nm CMOS process has been of interest to SKA consortiums for possible ASIC implementations for the Mid CBF and this work constitutes a self-contained proof-of-concept optimized multiplier on the 28 nm CMOS process.

The final proposed matrix architecture algorithm replaces the conventional CMAC cell with the proposed CoSMAC and PE correlation cells. This reduces the number of required correlation cells to Na^2 for calculating the total of $2Na^2 + Na$ baselines for all the Na dual polarised antennas. The proposed architecture nearly reduces half of the hardware requirements without degrading the performance and reduces the reusability factor and the number of ICs required to perform the overall correlation by $\frac{Na^2}{n^2}$. Comparisons between the existing systems and the proposed architecture improved correlator cells (CoSMAC and PE) with the new modified multiplier demonstrates that this design is more suitable for large interferometer projects like SKA.

6.2 Future Scope

The design methodology employed in this research work achieved the research outcome targeted. Fabrication, packing and lab testing of a Correlator/Beam former chip may be undertaken as 28 nm foundry costs decline and/or 28 nm MPW Fabruns become available, of which the proposed multiplier in this work will be a standard cell. A fully customized ASIC implementation of X/B – engine tailored to SKA Mid CBF is expected to be more power-efficient and/or hardware-efficient than a comparable off-the-shelf FPGA based solution. This is because for a given processing bandwidth and for the same semiconductor technology node, precise mapping of entire FPGA logic resources to the X/B-engine cells such as this optimized multiplier may not be achievable

The possible areas of further improvement in the design and performance as concluded below.

1) The proposed PE_IQ hardware structure for calculating two visibilities per baseline for IQ sampled signals has to be implemented and verified
2) The multiplier design proposed in this work is optimised for area and power with moderate speed. The use of ripple carry adder in the final additive stage of the reduction tree process doesn’t enhance the speed.

Some high-speed adders can be used to replace this ripple carry adder to increase the speed where the power and area are not a concern.

3) The Matrix architecture algorithm proposed in Chapter 5 has to be implemented and verified.
4) An additional optimised memory design will further improve the overall performance of the proposed algorithm.
5) An optimised high speed Serialiser and Deserialiser (SerDes) design is required to reduce the I/O requirements in ASIC design.
6) The use of High bandwidth memory to design the I/O buffers will give an added advantage for this design. (Some basic functionality and performance test of HBM are conducted in FPGA to analyse the feasibility of using this in ASIC design for future work)

REFERENCES

[1] J. L. Russell, "Kepler's laws of planetary motion: 1609–1666," *The British journal for the history of science*, vol. 2, no. 1, pp. 1-24, 1964.

[2] A. Mills and P. J. Turvey, "Newton's telescope, an examination of the reflecting telescope attributed to Sir Isaac Newton in the possession of the Royal Society," *Notes and Records of the Royal Society of London*, vol. 33, no. 2, pp. 133-155, 1979.

[3] L. Belkora, *Minding the heavens: the story of our discovery of the Milky Way*. CRC Press, 2002.

[4] Hoyle, Fred. "The big bang in astronomy." *New Scientist* 92 (1981): 521-524.

[5] S. Singh and B. Bang, *The Origin of the Universe*. Harper Perennial, 2005.

[6] A. R. Thompson, J. M. Moran, and G. W. Swenson, *Interferometry and synthesis in radio astronomy*. Wiley New York et al., 1986.

[7] Davis, J., and W. J. Tango. "A new very high angular resolution stellar interferometer." *Proceedings of the Astronomical Society of Australia*. Vol. 6. 1985.

[8] F.Ghigo, "Pre History of Radio Astronomy," Available: https://www.nrao.edu/whatisra/hist_prehist.shtml

[9] F. Ghigo, "Grote Reber," Available: https://www.nrao.edu/whatisra/hist_reber.shtml

[10] B. H. Bunch and A. Hellemans, *The history of science and technology: a browser's guide to the great discoveries, inventions, and the people who made them, from the dawn of time to today*. Houghton Mifflin Harcourt, 2004.

[11] Prof.F.G.Smith, "Radio Astronomy," Available: https://web.archive.org/web/20131110022209/http://www.phy.cam.ac.uk/history/years/radioast.php

[12] "Interferometry ", Available: https://en.wikipedia.org/wiki/Interferometry

[13] P. Hariharan, *Basics of interferometry*. Elsevier, 2010.

[14] Radio Astronomy [Online]. Available: https://en.wikipedia.org/wiki/Radio_astronomy

[15] D. P. Munns, *A single sky: How an international community forged the science of radio astronomy*. MIT Press, 2012.

[16] W. T. Sullivan III, *Cosmic noise: a history of early radio astronomy*. 2009.

[17] Michelson, Albert A. "I. On the application of interference methods to astronomical measurements." *The London, Edinburgh, and Dublin Philosophical Magazine and Journal of Science* 30.182 (1890): 1-21.

[18] Michelson, Albert A., "No. 184. On the application of interference methods to astronomical measurements," vol. 184, pp. 1-6, 1920.

[19] Ryle, Martin. "A new radio interferometer and its application to the observation of weak radio stars." *Proceedings of the Royal Society of London. Series A. Mathematical and Physical Sciences* 211.1106 (1952): 351-375.

[20] Bolton, J. G., and O. B. Slee. "Galactic radiation at radio frequencies. V. The sea interferometer." *Australian Journal of Physics* 6.4 (1953): 420-433.

[21] Bolton, J. G., and G. J. Stanley. "Variable source of radio frequency radiation in the constellation of Cygnus." *Nature* 161.4087 (1948): 312-313.

[22] Brown, R. Hanbury, and Richard Q. Twiss. "LXXIV. A new type of interferometer for use in radio astronomy." *The London, Edinburgh, and Dublin Philosophical Magazine and Journal of Science* 45.366 (1954): 663-682.

[23] Jennison, R. C., and V. Latham. "The brightness distribution within the radio sources Cygnus A (19N4A) and Cassiopeia A (23N5A)." *Monthly Notices of the Royal Astronomical Society* 119.2 (1959): 174-183.

[24] Brown, R. Hanbury, H. P. Palmer, and A. R. Thompson. "XCVII. A rotating-lobe interferometer and its application to radio astronomy." *The London, Edinburgh, and Dublin Philosophical Magazine and Journal of Science* 46.379 (1955): 857-866.

[25] R. L. Adgie, H. Gent, O. B. Slee, A. D. Frost, H. P. Palmer, and B. J. N. Rowson, "New limits to the angular sizes of some quasars," vol. 208, no. 5007, pp. 275-276, 1965.

[26] W. Christiansen and P. Warburton, "The Distribution of Radio Brightness over the Solar Disk at a Wavelength of 21 Centimetres. III. The Quiet Sun? Two-Dimensional Observations," vol. 8, no. 4, pp. 474-486, 1955.

[27] N. Labrum, E. Hartin, T. Krishnan, and W. Payten, "A compound interferometer with a 1.5 minute of arc fan beam," 1963.

[28] Read, R. "Two-element interferometer for accurate position determinations at 960 Mc." *IRE Transactions on Antennas and Propagation* 9.1 (1961): 31-35.

[29] J. Lequeux, "Mesures interférométriques à haute résolution du diamètre et de la structure des principales radio sources à 1420 MHz," in *Annales d'Astrophysique*, 1962, vol. 25, p. 221.

[30] R. S. Roger, C. Costain, J. Lacey, T. Landecker, and I. Bowers, "A supersynthesis radio telescope for neutral hydrogen spectroscopy at the Dominion Radio Astrophysical Observatory," vol. 61, no. 9, pp. 1270-1276, 1973.

[31] Ryle, M., and Ann C. Neville. "A radio survey of the North Polar region with a 4.5 minute of arc pencil-beam system." *Monthly Notices of the Royal Astronomical Society* 125.1 (1962): 39-56.

[32] J. W. Baars *et al.*, "The synthesis radio telescope at Westerbork," vol. 61, no. 9, pp. 1258-1266, 1973.

[33] Ryle, Martin. "The 5-km radio telescope at Cambridge." *Nature* 239.5373 (1972): 435-438.

[34] Thompson, A. Richard, et al. "The very large array." *The Astrophysical Journal Supplement Series* 44 (1980): 151-167..

[35] Linfield, Roger. "VLBI observations of jets in double radio galaxies." *The Astrophysical Journal* 244 (1981): 436-446.

[36] Mitra, A. N. "India's scientific community: A cultural crisis?." *Current Science* 69.10 (1995): 802-808.

[37] R. Perley *et al.*, "The expanded very large array," vol. 97, no. 8, pp. 1448-1462, 2009.

[38] M. Ishiguro and W. J. Welch, "Astronomy with millimeter and submillimeter wave interferometry," in *Astronomical Society of the Pacific Conference Series, Proceedings of IAU Colloquium 140, held in Sengokubara, Hakone, Japan, 5-9 October 1992, San Francisco: Astronomical Society of the Pacific (ASP),| c1994, edited by Ishiguro, M.; Welch, Wm. J.*, 1994.

[39] Ho, Paul TP, James M. Moran, and Kwok Yung Lo. "The submillimeter array." *The Astrophysical Journal Letters* 616.1 (2004): L1.

[40] Wootten, Alwyn, and A. Richard Thompson. "The Atacama large millimeter/submillimeter array." *Proceedings of the IEEE* 97.8 (2009): 1463-1471.

[41] P. Diamond, "The Square Kilometre Array: a physics machine for the 21st Century (Presentation Video)," in *Space Telescopes and Instrumentation 2014: Optical, Infrared, and Millimeter Wave*, 2014, vol. 9143, p. 91430M: International Society for Optics and Photonics.

[42] D'Addario, Larry R., and Douglas Wang. "An integrated circuit for radio astronomy correlators supporting large arrays of antennas." *Journal of Astronomical Instrumentation* 5.02 (2016): 1650002.

[43] R. N. Bracewell, *Two-dimensional imaging*. Prentice-Hall, Inc., 1995.

[44] R. N. Bracewell and R. N. Bracewell, *The Fourier transform and its applications*. McGraw-Hill New York, 1986.

[45] Brigham, E. Oran, and C. K. Yuen. "The fast Fourier transform." *IEEE Transactions on Systems, Man, and Cybernetics* 8.2 (1978): 146-146.

[46] White, R. G. "DC Champeney, Fourier Transforms and Their Physical Applications, Academic Press, London (1973) Price π5. 20." *Journal of Sound Vibration* 28.4 (1973): 782-782.

[47] A. R. Thompson, J. M. Moran, and G. W. Swenson, "Introductory Theory of Interferometry and Synthesis Imaging," in *Interferometry and Synthesis in Radio Astronomy*: Springer, 2017, pp. 59-88.

[48] Wiener, Norbert. "Generalized harmonic analysis." *Acta mathematica* 55 (1930): 117-258.

[49] Khintchine, Alexander. "Korrelationstheorie der stationären stochastischen Prozesse." *Mathematische Annalen* 109.1 (1934): 604-615.

[50] A. R. Thompson, J. M. Moran, and G. W. Swenson, "Analysis of the interferometer response," in *Interferometry and Synthesis in Radio Astronomy*: Springer, 2017, pp. 89-108.

[51] SKA. organisation. Square Kilometre Array [Online]. Available: http://www.skatelescope.org/

[52] Carilli, Christopher, and Steve Rawlings. "Science with the Square Kilometer Array: Motivation, key science projects, standards and assumptions." *arXiv preprint astro-ph/0409274* (2004).

[53] I. S. A. Committe, "Recommendations on Key Science Projects," 2003.

[54] Dewdney, Peter, W. Turner, R. Millenaar, R. McCool, J. Lazio, and T. Cornwell. "SKA1 system baseline design." *Document number SKA-TEL-SKO-DD-001 Revision* 1, no. 1 (2013).

[55] Magro, Alessio. "A Real-Time, GPU-Based, Non-Imaging Back-End for Radio Telescopes." *arXiv preprint arXiv:1401.8258* (2014).

[56] Turner, W., T. Cornwell, A. McPherson, and P. Diamond. "SKA phase 1 system (level 1) requirements specification." *SKA-TEL-SKO-0000008* (2014).

[57] SKA Organisation, "SKA Phase 1 System (Level 0) Requirements Specification" [Online]. Available: https://www.skatelescope.org/wp-content/uploads/2014/03/SKA1-Level0-Requirements.pdf

[58] SKA Organisation, "Low frequency aperture arrays" [Online]. Available: https://www.skatelescope.org/australia/

[59] Jongerius, Rik, Stefan Wijnholds, Ronald Nijboer, and Henk Corporaal. "An end-to-end computing model for the square kilometre array." *Computer* 47, no. 9 (2014): 48-54.

[60] de Vos, Marco, Andre W. Gunst, and Ronald Nijboer. "The LOFAR telescope: System architecture and signal processing." *Proceedings of the IEEE* 97, no. 8 (2009): 1431-1437.

[61] H. D. Falcke *et al.*, "A very brief description of LOFAR–the Low Frequency Array," vol. 2, no. 14, pp. 386-387, 2006.

[62] M. P. van Haarlem *et al.*, "LOFAR: The low-frequency array," vol. 556, p. A2, 2013.

[63] Sinclair, David, Fred Dulwich, Benjamin Mort, Michael E. Jones, Keith Grainge, and Eloy de Lera Acedo. "Effect of gain and phase errors on SKA1-low imaging quality from 50-600 MHz." *arXiv preprint arXiv:1408.3998* (2014).

[64] F.Dulwich. SKA memo #153 [Online]. Available: https://www.skatelescope.org/uploaded/23880_153_Memo_Sinclair.pdf

[65] E.Jones, "Increased SKA-Low Science Capability through Extended Frequency Coverage, SKA memo #149."

[66] Fiorin, Leandro, Erik Vermij, Jan van Lunteren, Rik Jongerius, and Christoph Hagleitner. "Exploring the design space of an energy-efficient accelerator for the SKA1-low central signal processor." *International Journal of Parallel Programming* 44, no. 5 (2016): 1003-1027..

[67] Vermij, Erik, Leandro Fiorin, Rik Jongerius, Christoph Hagleitner, and Koen Bertels. "Challenges in exascale radio astronomy: Can the SKA ride the technology wave?." *The International Journal of High Performance Computing Applications* 29, no. 1 (2015): 37-50.

[68] B. D. Jeffs. Beamforming presentation [Online]. Available: http://ens.ewi.tudelft.nl/Education/courses/et4235/Beamforming.pdf

[69] Auraß, Henry. "AR Thompson, JM Moran and GW Swenson, Jr.: Interferometry and Synthesis in Radio Astronomy. John Wiley and Sons, New York, 1986. XX+ 534 Seiten, Preis:£ 57.45." (1987): 124-124.

[70] A. Bridle and F. Schwab, "Bandwidth and time-average smearing," in *Synthesis Imaging in Radio Astronomy II*, 1999, vol. 180, p. 371.

[71] C. Tasse, S. van der Tol, J. van Zwieten, G. van Diepen, S. J. A. Bhatnagar, and Astrophysics, "Applying full polarization A-Projection to very wide field of view instruments: An imager for LOFAR," vol. 553, p. A105, 2013.

[72] Cornwell, Tim J., Kumar Golap, and Sanjay Bhatnagar. "The noncoplanar baselines effect in radio interferometry: The W-projection algorithm." *IEEE Journal of Selected Topics in Signal Processing* 2, no. 5 (2008): 647-657.

[73] T. Cornwell, M. Voronkov, and B. Humphreys, "Wide field imaging for the square kilometre array," in *Image Reconstruction from Incomplete Data VII*, 2012, vol. 8500, p. 85000L: International Society for Optics and Photonics.

[74] Högbom, J. A. "Aperture synthesis with a non-regular distribution of interferometer baselines." *Astronomy and Astrophysics Supplement Series* 15 (1974): 417.

[75] Fomalont, EDWARD B. "Earth-rotation aperture synthesis." *Proceedings of the IEEE* 61, no. 9 (1973): 1211-1218.

[76] Booth, R. S., and J. L. Jonas. "An overview of the MeerKAT project." *African Skies* 16 (2012): 101.

[77] L. Lentati *et al.*, "COLDz: Karl G. Jansky Very Large Array discovery of a gas-rich galaxy in COSMOS," vol. 800, no. 1, p. 67, 2015.

[78] Alexandru, A., C. A. Alexandru, D. Coardos, and E. Tudora. "Big data: concepts, technologies and applications in the public sector." *Int J Comput Electr Autom Control Inform Eng* 10 (2016): 1629-35.

[79] D. L. Jones *et al.*, "Big data challenges for large radio arrays," in *2012 IEEE Aerospace Conference*, 2012, pp. 1-6: IEEE.

[80] J. D. Bunton, "SKA correlators and beamformers," in *2015 IEEE International Conference on Acoustics, Speech and Signal Processing (ICASSP)*, 2015, pp. 5650-5653: IEEE.

[81] S. J. Tingay, "An overviewof the SKA project: Why take on this signal processing challenge?," in *2015 IEEE International Conference on Acoustics, Speech and Signal Processing (ICASSP)*, 2015, pp. 5640-5644: IEEE.

[82] G. Reber, "Radio astronomy: by John D. Kraus. 481 pages, diagrams, illustrations, 6× 9 in. New York, McGraw-Hill Book Co., 1966. ed: Pergamon, 1967.

[83] Edge, David O., and Michael J. Mulkay. "Astronomy transformed. The emergence of radio astronomy in Britain." *New York: Wiley* (1976).

[84] W. N. Christiansen and J. A. Högbom, *Radiotelescopes*. CUP Archive, 1987.

[85] G. Levy *et al.*, "Very long baseline interferometric observations made with an orbiting radio telescope," vol. 234, no. 4773, pp. 187-189, 1986.

[86] P. J. Hall, *The square kilometre array: An engineering perspective*. Springer, 2005.

[87] R. A. Perley, F. R. Schwab, and A. H. Bridle, "Synthesis imaging in radio astronomy," in *Synthesis Imaging in Radio Astronomy*, 1989, vol. 6.

[88] G. B. Taylor, C. L. Carilli, and R. A. Perley, "Synthesis imaging in radio astronomy II," in *Synthesis Imaging in Radio Astronomy II*, 1999, vol. 180.

[89] Taylor, Greg B., Chris Luke Carilli, and Richard A. Perley. "Synthesis imaging in radio astronomy II." *Synthesis Imaging in Radio Astronomy II* 180 (1999).

[90] Rabiner, Lawrence R., Bernard Gold, and C. K. Yuen. *Theory and application of digital signal processing*. Prentice-Hall, 2016.

[91] F. Lurz *et al.*, "Digital phase correction for multiplexed ADCs in low-cost Six-Port interferometers," in *2016 IEEE Topical Conference on Wireless Sensors and Sensor Networks (WiSNet)*, 2016, pp. 56-59: IEEE.

[92] Le, Bin, Thomas W. Rondeau, Jeffrey H. Reed, and Charles W. Bostian. "Analog-to-digital converters." *IEEE Signal Processing Magazine* 22, no. 6 (2005): 69-77.

[93] A. Bakshi, *Linear Integrated Circuits*. Technical Publications, 2008.

[94] C. E. Shannon, *The Mathematical Theory of Communication, by CE Shannon (and Recent Contributions to the Mathematical Theory of Communication), W. Weaver*. University of illinois Press, 1949.

[95] L. R. D'Addario, "Cross correlators," in *Synthesis Imaging in Radio Astronomy*, 1989, vol. 6, p. 59.

[96] Napier, Peter J., A. Richard Thompson, and Ronald D. Ekers. "The very large array: Design and performance of a modern synthesis radio telescope." *Proceedings of the IEEE* 71.11 (1983): 1295-1320.

[97] S. K. Okumura *et al.*, "1-GHz bandwidth digital spectro-correlator system for the Nobeyama millimeter array," vol. 52, no. 2, pp. 393-400, 2000.

[98] Hawkins, David W. "Digital lag (XF) correlator theory." *California Institute of Technology, Pasadena, CA* (2002).

[99] D.E.Gary. Radio astronomy lecture in Digital Cross-Correlators [Online]. Available: https://web.njit.edu/~gary/728/Lecture8.html

[100] D. Bock. Correlators and Back-ends [Online]. Available: http://www.atnf.csiro.au/research/radio-school/2011/talks/RAS-correlators.pdf

[101] Carlson, B. R., et al. "The S2 VLBI correlator: A correlator for space VLBI and geodetic signal processing." *Publications of the Astronomical Society of the Pacific* 111.762 (1999): 1025.

[102] A. Whitney *et al.*, "Mark 4 VLBI correlator: Architecture and algorithms," vol. 39, no. 1, pp. 1-24, 2004.

[103] A. R. Whitney, "How Do VLBI Correlators Work?," in *International VLBI Service for Geodesy and Astrometry 2000 General Meeting Proceedings*, 2000, pp. 187-205.

[104] B. Carlson and X. Correlator, "An Analysis of the Effects of Phase Dithering in a Lag-based Fringe-Stopping XF Correlator," 2000.

[105] Carlson, B. R. "Refined EVLA WIDAR Correlator Architecture." *NRC-EVLA Memo* 14 (2001).

[106] Chikada, Y., et al. "A digital FFT spectro-correlator for radio astronomy." *Indirect Imaging. Measurement and Processing for Indirect Imaging* (1984): 387.

[107] J. D. Bunton, "SKA correlator advances," in *The Square Kilometre Array: An Engineering Perspective*: Springer, 2005, pp. 251-259.

[108] J. D. Bunton, Telecommunications and A. Industrial Physics, "ALMA Memo 342-An Improved FX Correlator," 2000.

[109] Romney, J. D. "Introduction to the special-domain (FX) correlator." *VLBA Correlator Memorandum* 60 (1986).

[110] Harris, Chris, Karen Haines, and Lister Staveley-Smith. "GPU accelerated radio astronomy signal convolution." *Experimental Astronomy* 22.1-2 (2008): 129-141.

[111] L. Milic, T. Saramaki, and R. Bregovic, "Multirate filters: an overview," in *APCCAS 2006-2006 IEEE Asia Pacific Conference on Circuits and Systems*, 2006, pp. 912-915: IEEE.

[112] J. Wild, "Measurement and Processing for Indirect Imaging," in *Indirect Imaging. Measurement and Processing for Indirect Imaging*, 1984, p. 3.

[113] J. A. Zensus, P. Diamond, and P. Napier, *Very long baseline interferometry and the VLBA*. Astronomical Society of the Pacific, 1995.

[114] V. Tatke, "A Digital Spectral Correlator for GMRT," 2013.

[115] S. M. Spangenberg and G. J. Povey, "Code acquisition for LEO satellite mobile communication using a serial-parallel correlator with FFT for Doppler estimation," in *Proceedings of the International Symposium on Communication Systems and Digital Signal Processing (CSDSP)*, 1998: Citeseer.

[116] W. H. Press, S. A. Teukolsky, B. P. Flannery, and W. T. Vetterling, *Numerical recipes in Fortran 77: volume 1, volume 1 of Fortran numerical recipes: the art of scientific computing*. Cambridge university press, 1992.

[117] Okamura, S. K., et al. "Feasibility Study of the Enhanced Correlator for 3-way ALMA I." *ALMA Memo No. 350* (2001)..

[118] Welch, Peter. "The use of fast Fourier transform for the estimation of power spectra: a method based on time averaging over short, modified periodograms." *IEEE Transactions on audio and electroacoustics* 15.2 (1967): 70-73.

[119] D. B. Percival and A. T. Walden, *Spectral analysis for physical applications*. cambridge university press, 1993.

[120] J. D. Bunton, "Implementing Correlators for the SKA," in *Workshop on application of radio Science, Leura, Australia*, 2002, pp. 20-22.

[121] R. T. Rajan, M. Bentum, A. Gunst, and A.-J. Boonstra, "Distributed correlators for interferometry in space," in *2013 IEEE Aerospace Conference*, 2013, pp. 1-9: IEEE.

[122] L. R. D'Addario and D. Wang, "A low-power correlator ASIC for arrays with many antennas," in *2016 United States National Committee of URSI National Radio Science Meeting (USNC-URSI NRSM)*, 2016, pp. 1-2: IEEE.

[123] Lapshev, Stepan, and S.M. Rezaul Hasan. "On the architecture for the X part of a very large FX correlator using two-accumulator CMACs." *Experimental Astronomy* 41.1-2 (2016): 259-270.

[124] L. R. D'Addario, "Low-power correlator architecture for the mid-frequency SKA," 2011.

[125] Đ. Kurepa, *The Cartesian multiplication and the cellularity number*. Matematički institut, 1963.

[126] A. A. Karatsuba and Y. P. Ofman, "Multiplication of many-digital numbers by automatic computers," in *Doklady Akademii Nauk*, 1962, vol. 145, no. 2, pp. 293-294: Russian Academy of Sciences.

[127] Candau, Yves, Tarek Raissi, Nacim Ramdani, and Laurent Ibos. "Complex interval arithmetic using polar form." *Reliable Computing* 12, no. 1 (2006): 1-20.

[128] Weste, Neil HE, and Kamran Eshraghian. *Principles of VLSI CMOS Design: A Systems Perspective*. Addison-Wesley, 1993.

[129] Y. Wang, Y. Jiang, and E. Sha, "On area-efficient low power array multipliers," in *ICECS 2001. 8th IEEE International Conference on Electronics, Circuits and Systems (Cat. No. 01EX483)*, 2001, vol. 3, pp. 1429-1432: IEEE.

[130] S. Shah, A. Al-Khalili, and D. Al-Khalili, "Comparison of 32-bit multipliers for various performance measures," in *ICM 2000. Proceedings of the 12th International Conference on Microelectronics.(IEEE Cat. No. 00EX453)*, 2000, pp. 75-80: IEEE.

[131] Swee, Kelly Liew Suet, and Lo Hai Hiung. "Performance comparison review of 32-bit multiplier designs." *2012 4th International Conference on Intelligent and Advanced Systems (ICIAS2012)*. Vol. 2. IEEE, 2012.

[132] W. J. Townsend, E. E. Swartzlander Jr, and J. A. Abraham, "A comparison of Dadda and Wallace multiplier delays," in *Advanced signal processing algorithms, architectures, and implementations XIII*, 2003, vol. 5205, pp. 552-560: International Society for Optics and Photonics.

[133] Vaidya, Sumit, and Deepak Dandekar. "Delay-power performance comparison of multipliers in vlsi circuit design." *International Journal of Computer Networks & Communications (IJCNC)* 2.4 (2010): 47-56.

[134] Vaidya, Sumit R., and D. R. Dandekar. "Performance comparison of multipliers for power-speed trade-off in VLSI design." *RECENT ADVANCES in NETWORKING, VLSI and SIGNAL PROCESSING, ISSN* 5117 (1790).

[135] S. Kerur, J. C. Prakash Narchi, H. M. Kittur, and V. Girish, "Implementation of Vedic multiplier for digital signal processing," in *International Conference on VLSI, Communication & Instrumentation (ICVCI)*, 2011, pp. 1-6.

[136] Kumar, G. Ganesh, and V. Charishma. "Design of high speed vedic multiplier using vedic mathematics techniques." *International Journal of Scientific and Research Publications* 2.3 (2012): 1.

[137] Pradhan, Manoranjan, Rutuparna Panda, and Sushanta Kumar Sahu. "Speed comparison of 16x16 vedic multipliers." *International journal of computer applications* 21.6 (2011): 0975-8887.

[138] H. D. Tiwari, G. Gankhuyag, C. M. Kim, and Y. B. Cho, "Multiplier design based on ancient Indian Vedic Mathematics," in *2008 International SoC Design Conference*, 2008, vol. 2, pp. II-65-II-68: IEEE.

[139] Wallace, Christopher S. "A suggestion for a fast multiplier." *IEEE Transactions on electronic Computers* 1 (1964): 14-17.

[140] Cappello, Peter R., and Kenneth Steiglitz. "A VLSI layout for a pipelined Dadda multiplier." *ACM Transactions on Computer Systems (TOCS)* 1.2 (1983): 157-174.

[141] Booth, Andrew D. "A signed binary multiplication technique." *The Quarterly Journal of Mechanics and Applied Mathematics* 4.2 (1951): 236-240.

[142] Madrid, Philip E., Brian Millar, and Earl E. Swartzlander. "Modified Booth algorithm for high radix fixed-point multiplication." *IEEE transactions on very large scale integration (VLSI) systems* 1.2 (1993): 164-167.

[143] Gharabaghlo, Nader Sharifi, and Tohid Moradi Khaneshan. "Performance Analysis of High Speed Radix-4 Booth Encoders in CMOS Technology." *Majlesi Journal of Electrical Engineering* 13.3 (2019): 49-57.

[144] Kaur, Sukhmeet. "Suman and Manpreet Signh Manna,“Implementation of Modified Booth Algorithm (Radix 4) and its Comparison with Booth Algorithm (Radix-2)”." *Advance in Electronic and Electric Engineering* 3.6 (2013): 683-690.

[145] M. D. Ercegovac and T. Lang, *Digital arithmetic*. Elsevier, 2004.

[146] M. W. Czekalski, "Corner turn memory address generator," ed: Google Patents, 1984.

[147] H. Izumi, K. Sasaki, K. Nakajima, and H. Sato, "An efficient technique for corner-turn in SAR image reconstruction by improving cache access," in

Proceedings 16th International Parallel and Distributed Processing Symposium, 2001, p. 6 pp: IEEE.

[148] D. Ford, A. Faulkner, and P. Alexander, "A Software Correlator for SKA," ed: The SKA Publications. Memo, 2012.

[149] J. Bunton, G. Hampson, E. Kooistra, and Mika, "SKA CSP Low CBF-Detailed Design Document," 2016.

[150] Granholm, Johan, and Kim Woelders. "Dual polarization stacked microstrip patch antenna array with very low cross-polarization." *IEEE Transactions on Antennas and Propagation* 49.10 (2001): 1393-1402.

[151] R. John, "Dual-polarization antenna," ed: Google Patents, 1958.

[152] S.M.R. Hasan, and C.M. Hadzer, "A new distributed arithmetic VLSI architecture for discrete fourier transform processor," vol. 10, no. 2, pp. 105-114, 1993.

[153] Dubois ER, Venetsanopoulos A. Convolution using a conjugate symmetry property for the generalized discrete Fourier transform. IEEE Transactions on Acoustics, Speech, and Signal Processing. 1978 Apr;26(2):165-70.

[154] Ercegovac, Milos D., and Tomas Lang. "Fast multiplication without carry-propagate addition." *IEEE Transactions on Computers* 39.11 (1990): 1385-1390.

[155] R. K. Kolagotla, H. R. Srinivas, and G. F. Burns, "VLSI implementation of a 200-MHz 16/spl times/16 left-to-right carry-free multiplier in 0.35/spl mu/m CMOS technology for next-generation DSPs," in *Proceedings of CICC 97-Custom Integrated Circuits Conference*, 1997, pp. 469-472: IEEE.

[156] Behrooz, Parhami. "Computer arithmetic: Algorithms and hardware designs." *Oxford University Press* 19 (2000): 512583-512585.

[157] A. Artisan. 28 nm SC9MC Standard Cell Libraries [Online]. Available: https://www.arm.com/products/physical-ip/logic-ip/standardcell-libraries.php

[158] V. R. Balu and S. M. R. Hasan, "Computationally minimized X-part for FX correlator in big-data interferometers," *IEEE Access*, vol. 5, pp. 25353-25364, 2017.

[159] V. R. Balu and S. M. R. Hasan, "New optimized ASIC multiplier in 28 nm CMOS for processing the X-part of FX correlator in radio interferometry," *Experimental Astronomy*, vol. 47, no. 3, pp. 325-343, 2019.

[160] Y. Chikada, et al., “A 6 × 320-MHz 1024-channel FFT cross-spectrum analyzer for radio astronomy”, Proceedings of the IEEE (Volume: 75 , Issue: 9 , Sept. 1987), Page(s): 1203 – 1210, DOI: 10.1109/PROC.1987.13873

APPENDICES

8.1 Example calculations

8.1.1 Example 1: Modified Booth Algorithm

A		0 0 0 1 1 1 0 0	28
X	x	0 0 1 0 1 1 0 1	45
Y		0 1 0 -1 0 -1 0 1	recoded multiplier

Add A	+	0 0 0 0 1 1 1 0 0
2-Bit Shift		0 0 0 0 0 0 1 1 1 0 0
Add -A	+	1 1 1 1 0 0 1 0 0

---

		1 1 1 1 0 1 0 1 1 0 0
2-Bit Shift		1 1 1 1 1 1 0 1 0 1 1 0 0
Add -A	+	1 1 1 1 0 0 1 0 0

---

		1 1 1 0 1 1 1 0 1 1 0 0
2-Bit Shift		1 1 1 1 1 0 1 1 1 1 0 1 1 0 0
Add A	+	0 0 0 0 1 1 1 0 0

---

		0 0 0 0 1 0 0 1 1 1 0 1 1 0 0
2-Bit Shift		0 0 0 0 0 0 1 0 0 1 1 1 0 1 1 0 0 1260

8.1.2 Example 2: Booth Algorithm

A		0 0 0 1 1 1 0 0	28
X	x	0 0 1 0 1 1 0 1	45
Y		0 1 -1 1 0 -1 1 -1	recoded multiplier

Add -A	+	1 1 1 0 0 1 0 0
Shift		1 1 1 1 0 0 1 0 0
Add A	+	0 0 0 1 1 1 0 0

---

		0 0 0 0 1 1 1 0 0
Shift		0 0 0 0 0 1 1 1 0 0
Add -A	+	1 1 1 0 0 1 0 0

---

	1 1 1 0 1 0 1 1 0 0
Shift	1 1 1 1 0 1 0 1 1 0 0

Shift Only	1 1 1 1 1 0 1 0 1 1 0 0	
Add A	+ 0 0 0 1 1 1 0 0	
	0 0 0 1 0 1 1 0 1 1 0 0	
Shift	0 0 0 0 1 0 1 1 0 1 1 0 0	
Add -A	+ 1 1 1 0 0 1 0 0	
	1 1 1 0 1 1 1 1 0 1 1 0 0	
Shift	1 1 1 1 0 1 1 1 1 0 1 1 0 0	
Add A	+ 0 0 0 1 1 1 0 0	
	0 0 0 1 0 0 1 1 1 0 1 1 0 0	
Shift	0 0 0 0 1 0 0 1 1 1 0 1 1 0 0	
Shift Only	0 0 0 0 0 1 0 0 1 1 1 0 1 1 0 0	1260

8.2 FPGA Implementation Results of Correlator Cells.

The same architecture of CMAC, CoMAC and PE are synthesized in Xilinx tool to check their utilization of power, area and performance in FPGA. It is summarised from the Table 8-1 that the power and area utilisation of the proposed CoMAC and PE cells using FPGA are also less when compared with CMAC as that of the ASIC design.

Logic Utilization	**CMAC[1]**	**CoMAC[2]**	**PE[3]**
Number of Slice Registers	96	96	160
Number of Slice LUTs	104	128	291
Number of fully used LUT-FF pairs	48	64	128
Number of bonded IOBs	98	130	195
Number of BUFG/BUFGCTRLs	1	1	1
Number of DSP48E1s	4	4	4
Power Utilization(mW)			
I/O	236	312	468
Block Arithmetic	13	15.3	30.01
Total	249	327.3	498.01

(All values based on the synthesis tool ISE Design Suite 14.7 for Virtex-6 FPGA ML605 Evaluation Kit with 200MHz on board CLK.)
1 - Values for calculating single Cross correlation visibility.
2 - Values for calculating two Cross correlation visibilities.
3 – Values for calculating four Auto and two Cross correlation visibilities.

Table 8- 1 Logic and power requirement summary for single cell on FPGA platform.

8.3 Published Journal Paper I: Computationally Minimized X-Part for FX Correlator in Big-Data Interferometers [158]

Received October 10, 2017, accepted November 7, 2017, date of publication November 13, 2017,
date of current version December 5, 2017.

Digital Object Identifier 10.1109/ACCESS.2017.2772841

Computationally Minimized X-Part for FX Correlator in Big-Data Interferometers

VIGNESH RAJA BALU AND S. M. REZAUL HASAN, (Senior Member, IEEE)
Center for Research in Analog and VLSI Microsystem Design, School of Engineering and Advanced Technology, Massey University, Albany, Auckland 0632, New Zealand

Corresponding author: S. M. Rezaul Hasan (hasanmic@massey.ac.nz)

ABSTRACT Big-data is a challenging domain for high-throughput digital signal processing (DSP), especially in global-projects like the square kilometer array. The composite input data rate for correlator in this system is more than 11 Tb/s, which immensely increases the memory requirement, complexity of correlation implementation and the overall power dissipation. This paper is focused on computational minimization as well as the improvement of energy efficiency in the complex architectural X-part of an FX correlator employed in large array radio telescopes. A dedicated correlator-multiplier block termed, correlator-system-multiplier-and-accumulator (CoSMAC) cell architecture is proposed, which produces two 16-b integer complex multiplications within the same clock period. The novel hardware optimization is achieved by utilizing the flipped mirror relationship (conjugate complex symmetry) between discrete Fourier transform (DFT) samples owing to the symmetry and periodicity of the DFT coefficient vectors (twiddle factors). In addition, using the proposed CoSMAC architecture a new processing element (PE) is designed to calculate both the cross- and auto-correlation functions within the same clock period. This paper describes how the arithmetic processing of three baseline calculations will be minimized in the X-part using the proposed novel algorithm and hardware design (CoSMAC and PE). In addition to optimizing the core processing elements, it is possible to eliminate nearly 50% of the usual memory requirement. The design has been synthesized using global foundries 28-nm HPP CMOS standard cells.

INDEX TERMS SKA, VLBI, VLSI, FX correlator, complex multiplier, astronomical digital signal processing, deep nano-metric CMOS.

I. INTRODUCTION

Radio interferometers are array of telescopes which monitor the cosmic and astrophysical occurrences in space such as the very-long-baseline interferometer (VLBI) [1]. Many ongoing and future interferometers like Square Kilometer Array (SKA) [1] have very high input data rate [2] of at least 11 Tbps which creates a "BIG DATA" [3] computational problem for astronomers and design engineers. It significantly raises the order of complexity in signal processing electronics for storage, processing and transmitting the Tera-data in an efficient manner. There is thus an enormous necessity for providing faster and cheaper miniaturized low power electronics to overcome this *Big-data* challenge in astronomical digital signal processing (ADSP). The correlator plays a major role in the image formation in ADSP architectures of all interferometer types, and the FX correlator has been widely used [4]–[8] in this regard. Unlike the lag correlator [9], [10] (XF type), the FX correlator [7], [11] converts each time domain signal to frequency domain in the F-section followed by the X-section which performs the multiplication and accumulation over each frequency sample for all the signals and thus directly measures the cross-power spectrum. The correlator-size increases at the rate of square of the number of antennas (*Na*) in the interferometer, multiplied with the total bandwidth (*Tb*), and hence, justifies the fact that the correlator is the most power consuming unit for very large array telescope structures.

A correlator performs cross-correlation among signal pairs and auto-correlation of each signal with itself to form baselines using complex multiplication and accumulation (CMAC) units [4]–[8], [12]. The correlation product elements of baselines are called "*visibilities*" [13]. A comparison of the matrix correlator architecture [14] used in Atacama Large Millimeter/submillimeter Array (ALMA) [15], Expanded Very Large Array (EVLA) [16] and SKA [6], with the pipeline correlator architecture [17] used in Allan Telescope

8.4 Published Journal Paper II: New optimized ASIC multiplier in 28 nm CMOS for processing the X-part of FX correlator in radio interferometry [159].

ORIGINAL ARTICLE

New optimized ASIC multiplier in 28 nm CMOS for processing the X-part of FX correlator in radio interferometry

Vignesh Raja Balu[1] · S. M. Rezaul Hasan[1]

Received: 14 January 2019 / Accepted: 22 May 2019/Published online: 29 May 2019

Abstract
The choice of multiplier and accumulation unit determines the performance of digital signal processors, particularly in Big-Data correlators employed in radio interferometers. This work is targeted towards reducing the multiplier-size and delay in order to achieve low-power and compact-area for interferometer correlators such as in SKA and VLBI. For this purpose different fast and hardware efficient algorithms are compared and combined to achieve a new optimized ASIC multiplier design for performing correlation in radio interferometry. Further, the optimized new multiplier design is incorporated into our previous correlation processing cell designs of CMAC, CoSMAC and PE in Balu and Hasan: IEEE. Access. **5** 25353–25364, 2017. The improvement in performance is verified using the GlobalFoundries 28 nm HPP standard cell library.

Keywords Square kilometer Array · FX correlator · Complex multiplier · 28 nm CMOS · ASIC

1 Introduction

Big-Data [1] processing is the most challenging task in the present and future radio-telescopes (radio interferometers) such as the Very Long Baseline Interferometer (VLBI) [2] and Square Kilometer Array (SKA) [2] which have very high input data rate of a minimum of 11 Tbps [3]. These enormous data are processed

✉ S. M. Rezaul Hasan
hasanmic@massey.ac.nz

Vignesh Raja Balu
v.balu@massey.ac.nz

[1] Center for Research in Analog and VLSI microsystem dEsign (CRAVE), School of Advanced Technology, Massey University, ROOM: AV 2.3, Albany Village Level-2, Albany, Auckland 0632, New Zealand

8.5 To be Published, Journal Paper III: Efficient and Non-redundant Matrix Architecture for the X-section of an FX correlator in Large High Data rate Radio-Interferometers [Under the Publication process]

Efficient and Non-redundant Matrix Architecture for the X-section of an FX correlator in Large High Data-rate Radio-Interferometers

Vignesh Raja Balu, and S. M. Rezaul Hasan, *Senior Member, IEEE*

***Abstract*— In large radio-interferometers it is considerably challenging to perform signal correlations at input data-rates of over 11 Tbps, which involves vast amount of storage, memory-bandwidth and computational hardware. This paper is focused on reducing the memory-access and design complexity in matrix architectural processing of the complex X-section of an FX correlator employed in large array radio-telescopes. The conventional complex-multiplier-and-accumulators (CMACs) employed to calculate the complex multiplications is replaced with dedicated ASIC correlator cells with optimized multipliers to reduce the overall power and area requirements in a matrix correlator architecture. The proposed architecture reduces by half the number of ASIC processor cells required to perform the complete correlation in large interferometers by eliminating redundant cells. This reduction in the number of ASIC processor cells reduces the memory requirement and the number of memory operations, which results in reduced power consumption. This new matrix architectural minimization is very effective in reducing the hardware complexity of large interferometers like the Square Kilometer Array (SKA).**

***Index Terms*— Square Kilometer Array, FX Correlator, Matrix architecture, Hardware minimization, CMAC, CoSMAC, PE, ASIC.**

I. Introduction

THE most challenging aspect in Radio-interferometers is the implementation of the digital signal processing for the enormous amount of processed data received from their antennas at the speed of tens of Tbps [1]. The efficient dispensation of these massive amount of data ("Big-data") significantly increases the hardware required to perform the processing and storage [2] in interferometers. This Big-data processing also surges the complexity of correlation computations since the size of the correlator depends on the number of antennas and the total signal bandwidth received from them. The signals received from these antennas undergo some adequate phase-amplitude calibration before it is correlated and beam-formed to constitute an image. The correlator is the main section in radio-interferometers which calculates the cross- and auto- correlation of antenna pairs that form the baselines [3] for imaging. The products generated in a cross-correlation baseline are called "visibilities" while the products in an auto-correlation baseline are considered as signal power for a source with "visibility" = 1 [4, 5]. Visibility calculations in baselines involves complex multiplication and accumulation over time between the antenna pairs by means of XF correlator (lag correlator) [6, 7] or FX correlator [8, 9]. In larger interferometers mostly FX type correlator is employed in order to directly measure the cross power spectrum with improved frequency-to-frequency isolation [10, 11]. Fig. 1 shows the general architecture of an FX correlator with Na number of dual polarized antennas which produces $2Na$ number of output signals. These signals are time sampled and fed into the F-section of the FX correlator where N-point FFT (Fast Fourier Transform) is performed and the F-section outputs the N discrete frequency channels to the X-section. The X-section calculates the "visibilities" by performing complex multiplications among two samples (of the same frequency channel for all the N channels) and accumulating for the same time-slice m (of overall dump period T) from each signal pair of $2Na^2$-Na cross-correlation baselines and $2Na$ auto-correlation baselines [3]. The resulting total number of visibility calculations $Tot_{visibilities}$ obtained from Na number of dual polarized antennas which are accumulated over the dump period T ($m=0,1,2, \ldots T-1$) is then given by (1) below.

$$Tot_{visibilities} = \sum_{m=0}^{T-1} \{(2Na^2 + Na)N\}_m \quad (1)$$

Compared to the existing large correlators such as Atacama Large Millimetre/Submillimetre Array (ALMA) [8] and Expanded Very Large Array (EVLA) [12], the Square Kilometre Array (SKA) [5, 10] is specified to provide ~10000 times higher performance, along-with much higher energy efficiency. Hence, a careful selection of hardware architecture for performing the vast correlation computations is extremely essential to optimize the cost of implementing and running large Big-data correlators like SKA. The expression in (2) below is used to estimate the size of a correlator Cs required to calculate the overall bandwidth (Tb) attained from (Na) number of antennas in an interferometer [3].

$$Cs = Na^2 \times Tb \quad (2)$$

The expressions in (1) and (2) indicates the enormity of power consumption and hardware-area utilization of the

Manuscript received May. 25, 2020.

The authors are with the Center for Research in Analog and VLSI Microsystem dEsign (CRAVE), School of Engineering and Advanced Technology (SEAT), Massey University, Albany, Auckland 0632, New Zealand (e-mail: v.balu@massey.ac.nz; hasanmic@massey.ac.nz).

8.6 Statement of Contribution

DRC 16

MASSEY UNIVERSITY
GRADUATE RESEARCH SCHOOL

STATEMENT OF CONTRIBUTION
DOCTORATE WITH PUBLICATIONS/MANUSCRIPTS

We, the candidate and the candidate's Primary Supervisor, certify that all co-authors have consented to their work being included in the thesis and they have accepted the candidate's contribution as indicated below in the *Statement of Originality*.

Name of candidate:	Vignesh Raja Balu
Name/title of Primary Supervisor:	Dr. S.M. Rezaul Hasan
Name of Research Output and full reference:	New optimized ASIC Multiplier in 28nm CMOS for Processing The x-Part of FX-correlator in radio Astronomy, experimental Astronomy, Vol. 47, No. 3, pp 325-343, 2019
In which Chapter is the Manuscript /Published work:	Chapter - 4
Please indicate:	
~~• The percentage of the manuscript/Published Work that was contributed by the candidate:~~	
~~and~~	
• Describe the contribution that the candidate has made to the Manuscript/Published Work:	
Vignesh carried out the entire research work under my supervision.	
For manuscripts intended for publication please indicate target journal:	
Candidate's Signature:	
Date:	29/05/2020
Primary Supervisor's Signature:	
Date:	29/05/2020

(This form should appear at the end of each thesis chapter/section/appendix submitted as a manuscript/ publication or collected as an appendix at the end of the thesis)

DRC 16

MASSEY UNIVERSITY
GRADUATE RESEARCH SCHOOL

STATEMENT OF CONTRIBUTION
DOCTORATE WITH PUBLICATIONS/MANUSCRIPTS

We, the candidate and the candidate's Primary Supervisor, certify that all co-authors have consented to their work being included in the thesis and they have accepted the candidate's contribution as indicated below in the *Statement of Originality*.

Name of candidate:	Vignesh Raja Balu
Name/title of Primary Supervisor:	Dr. S.M. Rezaul Hasan
Name of Research Output and full reference:	Computationally minimized x-part for fx correlator in big-data interferometers, – IEEE Access, Vol 5, pp 25353–25364, 2017
In which Chapter is the Manuscript /Published work:	Chapter – 4
Please indicate:	
• ~~The percentage of the manuscript/Published Work that was contributed by the candidate:~~	
~~and~~	
• Describe the contribution that the candidate has made to the Manuscript/Published Work:	
Vignesh carried out the entire research work under my supervision	
For manuscripts intended for publication please indicate target journal:	
Candidate's Signature:	
Date:	29/05/2020
Primary Supervisor's Signature:	
Date:	29/05/2020

(This form should appear at the end of each thesis chapter/section/appendix submitted as a manuscript/ publication or collected as an appendix at the end of the thesis)

DRC 16

MASSEY UNIVERSITY
GRADUATE RESEARCH SCHOOL

STATEMENT OF CONTRIBUTION
DOCTORATE WITH PUBLICATIONS/MANUSCRIPTS

We, the candidate and the candidate's Primary Supervisor, certify that all co-authors have consented to their work being included in the thesis and they have accepted the candidate's contribution as indicated below in the *Statement of Originality*.

Name of candidate:	Vignesh Raja Balu
Name/title of Primary Supervisor:	Dr. S.M. Rezaul Hasan
Name of Research Output and full reference:	Efficient and non-redundant mamx architecture for the x-section of an Fx correlator in Large High Data rate radio Interferometers.
In which Chapter is the Manuscript /Published work:	Chapter 5
Please indicate:	
• ~~The percentage of the manuscript/Published Work that was contributed by the candidate~~:	
~~and~~	
• Describe the contribution that the candidate has made to the Manuscript/Published Work:	
Vignesh carried out the entire research work under my supervision	
For manuscripts intended for publication please indicate target journal:	
Journal of Experimental Astronomy	
Candidate's Signature:	
Date:	29/05/2020
Primary Supervisor's Signature:	
Date:	29/05/2020

(This form should appear at the end of each thesis chapter/section/appendix submitted as a manuscript/ publication or collected as an appendix at the end of the thesis)